Search for neutral and charged Higgs bosons in e^+e^- collisions at $\sqrt{s}=$ 161 GeV and 172 GeV

P. Abreu, W. Adam, T. Adye, P. Adzic, I. Ajinenko, G D. Alekseev, R. Alemany, P P. Allport, S. Almehed, U. Amaldi, et al.

▶ **To cite this version:**

HAL Id: in2p3-00003399
http://hal.in2p3.fr/in2p3-00003399

Submitted on 3 Nov 1998

Search for neutral and charged Higgs bosons in e^+e^- collisions at $\sqrt{s} = 161$ GeV and 172 GeV

DELPHI Collaboration

Abstract

A search for neutral and charged Higgs bosons has been performed in the data collected by the DELPHI detector at centre-of-mass energies of 161 GeV and 172 GeV. The analysis assumes either the pair-production of charged Higgs bosons, $H^{\pm}$, or the production of the lightest neutral Higgs boson, h, with either a Z or a neutral pseudoscalar Higgs boson, A. All final state topologies expected from the decay of h and A into hadrons or a pair of τ leptons, and from the decay of $H^{\pm}$ into a pair of quarks or a $\tau\nu_{\tau}$ pair have been considered. Lower limits at the 95% confidence level have been obtained on the Higgs boson masses. The limits are 66.2 GeV/c^2 for h in the Standard Model, 59.5 GeV/c^2 for h and 51.0 GeV/c^2 for A in the minimal supersymmetric extension of the Standard Model and 51.5 GeV/c^2 for $H^{\pm}$ in the general two-doublet scheme for $H^{\pm}$ branching fractions into hadrons below 0.8.

11

P.Abreu[21], W.Adam[49], T.Adye[36], P.Adzic[11], I.Ajinenko[41], G.D.Alekseev[16], R.Alemany[48], P.P.Allport[22], S.Almehed[24], U.Amaldi[9], S.Amato[46], P.Andersson[43], A.Andreazza[9], P.Antilogus[9], W-D.Apel[17], Y.Arnoud[14], B.Åsman[43], J-E.Augustin[25], A.Augustinus[30], P.Baillon[9], P.Bambade[19], M.Barbi[46], D.Y.Bardin[16], G.Barker[9], A.Baroncelli[39], O.Barring[24], M.J.Bates[36], M.Battaglia[15], M.Baubillier[23], J.Baudot[38], K-H.Becks[51], M.Begalli[6], P.Beilliere[8], Yu.Belokopytov[9,52], A.C.Benvenuti[5], C.Berat[14], M.Berggren[46], D.Bertini[25], D.Bertrand[2], M.Besancon[38], F.Bianchi[44], M.Bigi[44], M.S.Bilenky[16], P.Billoir[23], M-A.Bizouard[19], D.Bloch[10], M.Blume[51], M.Bonesini[27], W.Bonivento[27], M.Boonekamp[38], P.S.L.Booth[22], A.W.Borgland[4], G.Borisov[38,41], C.Bosio[39], O.Botner[47], E.Boudinov[30], B.Bouquet[19], C.Bourdarios[19], T.J.V.Bowcock[22], M.Bozzo[13], P.Branchini[39], K.D.Brand[35], T.Brenke[51], R.A.Brenner[47], R.C.A.Brown[9], P.Bruckman[18], J-M.Brunet[8], L.Bugge[32], T.Buran[32], T.Burgsmueller[51], P.Buschmann[51], S.Cabrera[48], M.Caccia[27], M.Calvi[27], A.J.Camacho Rozas[40], T.Camporesi[9], V.Canale[37], M.Canepa[13], F.Carena[9], L.Carroll[22], C.Caso[13], M.V.Castillo Gimenez[48], A.Cattai[9], F.R.Cavallo[5], V.Chabaud[9], Ph.Charpentier[9], L.Chaussard[25], P.Checchia[35], G.A.Chelkov[16], M.Chen[2], R.Chierici[44], P.Chliapnikov[41], P.Chochula[7], V.Chorowicz[25], J.Chudoba[29], V.Cindro[42], P.Collins[9], M.Colomer[48], R.Contri[13], E.Cortina[48], G.Cosme[19], F.Cossutti[45], J-H.Cowell[22], H.B.Crawley[1], D.Crennell[36], G.Crosetti[13], J.Cuevas Maestro[33], S.Czellar[15], J.Dahm[51], B.Dalmagne[19], G.Damgaard[28], P.D.Dauncey[36], M.Davenport[9], W.Da Silva[23], A.Deghorain[2], G.Della Ricca[45], P.Delpierre[26], N.Demaria[34], A.De Angelis[9], W.De Boer[17], S.De Brabandere[2], C.De Clercq[2], C.De La Vaissiere[23], B.De Lotto[45], A.De Min[35], L.De Paula[46], H.Dijkstra[9], L.Di Ciaccio[37], A.Di Diodato[37], A.Djannati[8], J.Dolbeau[8], K.Doroba[50], M.Dracos[10], J.Drees[51], K.-A.Drees[51], M.Dris[31], J-D.Durand[25,9], D.Edsall[1], R.Ehret[17], G.Eigen[4], T.Ekelof[47], G.Ekspong[43], M.Elsing[9], J-P.Engel[10], B.Erzen[42], M.Espirito Santo[21], E.Falk[24], G.Fanourakis[11], D.Fassouliotis[45], M.Feindt[9], A.Fenyuk[41], P.Ferrari[27], A.Ferrer[48], S.Fichet[23], T.A.Filippas[31], A.Firestone[1], P.-A.Fischer[10], H.Foeth[9], E.Fokitis[31], F.Fontanelli[13], F.Formenti[9], B.Franek[36], A.G.Frodesen[4], R.Fruhwirth[49], F.Fulda-Quenzer[19], J.Fuster[48], A.Galloni[22], D.Gamba[44], M.Gandelman[46], C.Garcia[48], J.Garcia[40], C.Gaspar[9], U.Gasparini[35], Ph.Gavillet[9], E.N.Gazis[31], D.Gele[10], J-P.Gerber[10], L.Gerdyukov[41], R.Gokieli[50], B.Golob[42], P.Goncalves[21], G.Gopal[36], L.Gorn[1], M.Gorski[50], Yu.Gouz[44,52], V.Gracco[13], E.Graziani[39], C.Green[22], A.Grefrath[51], P.Gris[38], G.Grosdidier[19], K.Grzelak[50], M.Gunther[47], J.Guy[36], F.Hahn[9], S.Hahn[51], Z.Hajduk[18], A.Hallgren[47], K.Hamacher[51], F.J.Harris[34], V.Hedberg[24], R.Henriques[21], J.J.Hernandez[48], P.Herquet[2], H.Herr[9], T.L.Hessing[34], J.-M.Heuser[51], E.Higon[48], S-O.Holmgren[43], P.J.Holt[34], D.Holthuizen[30], S.Hoorelbeke[2], M.Houlden[22], J.Hrubec[49], K.Huet[2], K.Hultqvist[43], J.N.Jackson[22], R.Jacobsson[43], P.Jalocha[9], R.Janik[7], Ch.Jarlskog[24], G.Jarlskog[24], P.Jarry[38], B.Jean-Marie[19], E.K.Johansson[43], L.Jonsson[24], P.Jonsson[24], C.Joram[9], P.Juillot[10], M.Kaiser[17], F.Kapusta[23], K.Karafasoulis[11], E.Karvelas[11], S.Katsanevas[25], E.C.Katsoufis[31], R.Keranen[4], Yu.Khokhlov[41], B.A.Khomenko[16], N.N.Khovanski[16], B.King[22], N.J.Kjaer[30], O.Klapp[51], H.Klein[9], P.Kluit[30], D.Knoblauch[17], P.Kokkinias[11], M.Koratzinos[9], K.Korcyl[18], V.Kostioukhine[41], C.Kourkoumelis[3], O.Kouznetsov[16], M.Krammer[49], C.Kreuter[9], I.Kronkvist[24], Z.Krumstein[16], W.Krupinski[18], P.Kubinec[7], W.Kucewicz[18], K.Kurvinen[15], C.Lacasta[9], I.Laktineh[25], J.W.Lamsa[1], L.Lanceri[45], D.W.Lane[1], P.Langefeld[51], J-P.Laugier[38], R.Lauhakangas[15], G.Leder[49], F.Ledroit[14], V.Lefebure[2], C.K.Legan[1], A.Leisos[11], R.Leitner[29], J.Lemonne[2], G.Lenzen[51], V.Lepeltier[19], T.Lesiak[18], M.Lethuillier[38], J.Libby[34], D.Liko[9], A.Lipniacka[43], I.Lippi[35], B.Loerstad[24], J.G.Loken[34], J.M.Lopez[40], D.Loukas[11], P.Lutz[38], L.Lyons[34], J.MacNaughton[49], G.Maehlum[17], J.R.Mahon[6], A.Maio[21], T.G.M.Malmgren[43], V.Malychev[16], F.Mandl[49], J.Marco[40], R.Marco[40], B.Marechal[46], M.Margoni[35], J-C.Marin[9], C.Mariotti[9], A.Markou[11], C.Martinez-Rivero[33], F.Martinez-Vidal[48], S.Marti i Garcia[22], J.Masik[29], F.Matorras[40], C.Matteuzzi[27], G.Matthiae[37], M.Mazzucato[35], M.Mc Cubbin[22], R.Mc Kay[1], R.Mc Nulty[9], G.Mc Pherson[22], J.Medbo[47], C.Meroni[27], S.Meyer[17], W.T.Meyer[1], M.Michelotto[35], E.Migliore[44], L.Mirabito[25], W.A.Mitaroff[49], U.Mjoernmark[24], T.Moa[43], R.Moeller[28], K.Moenig[9], M.R.Monge[13], P.Morettini[13], H.Mueller[17], K.Muenich[51], M.Mulders[30], L.M.Mundim[6], W.J.Murray[36], B.Muryn[14,18], G.Myatt[34], T.Myklebust[32], F.Naraghi[14], F.L.Navarria[5], S.Navas[48], K.Nawrocki[50], P.Negri[27], S.Nemecek[12], W.Neumann[51], N.Neumeister[49], R.Nicolaidou[3], B.S.Nielsen[28], M.Nieuwenhuizen[30], V.Nikolaenko[10], M.Nikolenko[10,16], P.Niss[43], A.Nomerotski[35], A.Normand[22], A.Nygren[24], W.Oberschulte-Beckmann[17], V.Obraztsov[41], A.G.Olshevski[16], A.Onofre[21], R.Orava[15], G.Orazi[10], S.Ortuno[48], K.Osterberg[15], A.Ouraou[38], P.Paganini[19], M.Paganoni[9,27], S.Paiano[5], R.Pain[23], H.Palka[18], Th.D.Papadopoulou[31], K.Papageorgiou[11], L.Pape[9], C.Parkes[34], F.Parodi[13], U.Parzefall[22], A.Passeri[39], M.Pegoraro[35], L.Peralta[21], H.Pernegger[49], M.Pernicka[49], A.Perrotta[5], C.Petridou[45], A.Petrolini[13], H.T.Phillips[36], G.Piana[13], F.Pierre[38], M.Pimenta[21], E.Piotto[35], T.Podobnik[34], O.Podobrin[9], M.E.Pol[6], G.Polok[18], P.Poropat[45], V.Pozdniakov[16], P.Privitera[37], N.Pukhaeva[16], A.Pullia[27], D.Radojicic[34], S.Ragazzi[27], H.Rahmani[31], P.N.Ratoff[20], A.L.Read[32], M.Reale[51], P.Rebecchi[9], N.G.Redaelli[27], M.Regler[49], D.Reid[9], R.Reinhardt[51], P.B.Renton[34], L.K.Resvanis[3], F.Richard[19], J.Ridky[12], G.Rinaudo[44], O.Rohne[32], A.Romero[44], P.Ronchese[35], L.Roos[23], E.I.Rosenberg[1], P.Rosinsky[7], P.Roudeau[19], T.Rovelli[5], V.Ruhlmann-Kleider[38], A.Ruiz[40], K.Rybicki[18], H.Saarikko[15], Y.Sacquin[38], A.Sadovsky[16], G.Sajot[14], J.Salt[48], M.Sannino[13], H.Schneider[17], U.Schwickerath[17], M.A.E.Schyns[51], G.Sciolla[44], F.Scuri[45], P.Seager[20], Y.Sedykh[16], A.M.Segar[34], A.Seitz[17], R.Sekulin[36], L.Serbelloni[37], R.C.Shellard[6], A.Sheridan[22], P.Siegrist[9,38], R.Silvestre[38], F.Simonetto[35], A.N.Sisakian[16], T.B.Skaali[32], G.Smadja[25], O.Smirnova[24], G.R.Smith[36], A.Sokolov[41], O.Solovianov[41], R.Sosnowski[50], D.Souza-Santos[6], T.Spassov[21], E.Spiriti[39], P.Sponholz[51], S.Squarcia[13], D.Stampfer[9], C.Stanescu[39], S.Stanic[42], S.Stapnes[32], I.Stavitski[35], K.Stevenson[34], A.Stocchi[19], J.Strauss[49], R.Strub[10], B.Stugu[4], M.Szczekowski[50], M.Szeptycka[50], T.Tabarelli[27], J.P.Tavernet[23], E.Tcherniaev[41], O.Tchikilev[41], F.Tegenfeldt[47], F.Terranova[27], J.Thomas[34], A.Tilquin[26],

J.Timmermans[30], L.G.Tkatchev[16], T.Todorov[10], S.Todorova[10], D.Z.Toet[30], A.Tomaradze[2], B.Tome[21], A.Tonazzo[27], L.Tortora[39], G.Transtromer[24], D.Treille[9], G.Tristram[8], A.Trombini[19], C.Troncon[27], A.Tsirou[9], M-L.Turluer[38], I.A.Tyapkin[16], M.Tyndel[36], S.Tzamarias[11], B.Ueberschaer[51], O.Ullaland[9], V.Uvarov[41], G.Valenti[5], E.Vallazza[45], C.Vander Velde[2], G.W.Van Apeldoorn[30], P.Van Dam[30], W.K.Van Doninck[2], J.Van Eldik[30], A.Van Lysebetten[2], N.Vassilopoulos[34], G.Vegni[27], L.Ventura[35], W.Venus[36], F.Verbeure[2], M.Verlato[35], L.S.Vertogradov[16], D.Vilanova[38], P.Vincent[25], L.Vitale[45], E.Vlasov[41], A.S.Vodopyanov[16], V.Vrba[12], H.Wahlen[51], C.Walck[43], F.Waldner[45], C.Weiser[17], A.M.Wetherell[9], D.Wicke[51], J.H.Wickens[2], M.Wielers[17], G.R.Wilkinson[9], W.S.C.Williams[34], M.Winter[10], M.Witek[18], T.Wlodek[19], J.Yi[1], K.Yip[34], O.Yushchenko[41], F.Zach[25], A.Zaitsev[41], A.Zalewska[9], P.Zalewski[50], D.Zavrtanik[42], E.Zevgolatakos[11], N.I.Zimin[16], G.C.Zucchelli[43], G.Zumerle[35]

[1] Department of Physics and Astronomy, Iowa State University, Ames IA 50011-3160, USA
[2] Physics Department, Univ. Instelling Antwerpen, Universiteitsplein 1, B-2610 Wilrijk, Belgium
  and IIHE, ULB-VUB, Pleinlaan 2, B-1050 Brussels, Belgium
  and Faculté des Sciences, Univ. de l'Etat Mons, Av. Maistriau 19, B-7000 Mons, Belgium
[3] Physics Laboratory, University of Athens, Solonos Str. 104, GR-10680 Athens, Greece
[4] Department of Physics, University of Bergen, Allégaten 55, N-5007 Bergen, Norway
[5] Dipartimento di Fisica, Università di Bologna and INFN, Via Irnerio 46, I-40126 Bologna, Italy
[6] Centro Brasileiro de Pesquisas Físicas, rua Xavier Sigaud 150, RJ-22290 Rio de Janeiro, Brazil
  and Depto. de Física, Pont. Univ. Católica, C.P. 38071 RJ-22453 Rio de Janeiro, Brazil
  and Inst. de Física, Univ. Estadual do Rio de Janeiro, rua São Francisco Xavier 524, Rio de Janeiro, Brazil
[7] Comenius University, Faculty of Mathematics and Physics, Mlynska Dolina, SK-84215 Bratislava, Slovakia
[8] Collège de France, Lab. de Physique Corpusculaire, IN2P3-CNRS, F-75231 Paris Cedex 05, France
[9] CERN, CH-1211 Geneva 23, Switzerland
[10] Institut de Recherches Subatomiques, IN2P3 - CNRS/ULP - BP20, F-67037 Strasbourg Cedex, France
[11] Institute of Nuclear Physics, N.C.S.R. Demokritos, P.O. Box 60228, GR-15310 Athens, Greece
[12] FZU, Inst. of Physics of the C.A.S. High Energy Physics Division, Na Slovance 2, 180 40, Praha 8, Czech Republic
[13] Dipartimento di Fisica, Università di Genova and INFN, Via Dodecaneso 33, I-16146 Genova, Italy
[14] Institut des Sciences Nucléaires, IN2P3-CNRS, Université de Grenoble 1, F-38026 Grenoble Cedex, France
[15] Helsinki Institute of Physics, HIP, P.O. Box 9, FIN-00014 Helsinki, Finland
[16] Joint Institute for Nuclear Research, Dubna, Head Post Office, P.O. Box 79, 101 000 Moscow, Russian Federation
[17] Institut für Experimentelle Kernphysik, Universität Karlsruhe, Postfach 6980, D-76128 Karlsruhe, Germany
[18] Institute of Nuclear Physics and University of Mining and Metalurgy, Ul. Kawiory 26a, PL-30055 Krakow, Poland
[19] Université de Paris-Sud, Lab. de l'Accélérateur Linéaire, IN2P3-CNRS, Bât. 200, F-91405 Orsay Cedex, France
[20] School of Physics and Chemistry, University of Lancaster, Lancaster LA1 4YB, UK
[21] LIP, IST, FCUL - Av. Elias Garcia, 14-1°, P-1000 Lisboa Codex, Portugal
[22] Department of Physics, University of Liverpool, P.O. Box 147, Liverpool L69 3BX, UK
[23] LPNHE, IN2P3-CNRS, Universités Paris VI et VII, Tour 33 (RdC), 4 place Jussieu, F-75252 Paris Cedex 05, France
[24] Department of Physics, University of Lund, Sölvegatan 14, S-22363 Lund, Sweden
[25] Université Claude Bernard de Lyon, IPNL, IN2P3-CNRS, F-69622 Villeurbanne Cedex, France
[26] Univ. d'Aix - Marseille II - CPP, IN2P3-CNRS, F-13288 Marseille Cedex 09, France
[27] Dipartimento di Fisica, Università di Milano and INFN, Via Celoria 16, I-20133 Milan, Italy
[28] Niels Bohr Institute, Blegdamsvej 17, DK-2100 Copenhagen 0, Denmark
[29] NC, Nuclear Centre of MFF, Charles University, Areal MFF, V Holesovickach 2, 180 00, Praha 8, Czech Republic
[30] NIKHEF, Postbus 41882, NL-1009 DB Amsterdam, The Netherlands
[31] National Technical University, Physics Department, Zografou Campus, GR-15773 Athens, Greece
[32] Physics Department, University of Oslo, Blindern, N-1000 Oslo 3, Norway
[33] Dpto. Fisica, Univ. Oviedo, Avda. Calvo Sotelo, S/N-33007 Oviedo, Spain, (CICYT-AEN96-1681)
[34] Department of Physics, University of Oxford, Keble Road, Oxford OX1 3RH, UK
[35] Dipartimento di Fisica, Università di Padova and INFN, Via Marzolo 8, I-35131 Padua, Italy
[36] Rutherford Appleton Laboratory, Chilton, Didcot OX11 OQX, UK
[37] Dipartimento di Fisica, Università di Roma II and INFN, Tor Vergata, I-00173 Rome, Italy
[38] CEA, DAPNIA/Service de Physique des Particules, CE-Saclay, F-91191 Gif-sur-Yvette Cedex, France
[39] Istituto Superiore di Sanità, Ist. Naz. di Fisica Nucl. (INFN), Viale Regina Elena 299, I-00161 Rome, Italy
[40] Instituto de Fisica de Cantabria (CSIC-UC), Avda. los Castros, S/N-39006 Santander, Spain, (CICYT-AEN96-1681)
[41] Inst. for High Energy Physics, Serpukov P.O. Box 35, Protvino, (Moscow Region), Russian Federation
[42] J. Stefan Institute, Jamova 39, SI-1000 Ljubljana, Slovenia and Department of Astroparticle Physics, School of Environmental Sciences, Kostanjeviska 16a, Nova Gorica, SI-5000 Slovenia,
  and Department of Physics, University of Ljubljana, SI-1000 Ljubljana, Slovenia
[43] Fysikum, Stockholm University, Box 6730, S-113 85 Stockholm, Sweden
[44] Dipartimento di Fisica Sperimentale, Università di Torino and INFN, Via P. Giuria 1, I-10125 Turin, Italy
[45] Dipartimento di Fisica, Università di Trieste and INFN, Via A. Valerio 2, I-34127 Trieste, Italy
  and Istituto di Fisica, Università di Udine, I-33100 Udine, Italy
[46] Univ. Federal do Rio de Janeiro, C.P. 68528 Cidade Univ., Ilha do Fundão BR-21945-970 Rio de Janeiro, Brazil
[47] Department of Radiation Sciences, University of Uppsala, P.O. Box 535, S-751 21 Uppsala, Sweden
[48] IFIC, Valencia-CSIC, and D.F.A.M.N., U. de Valencia, Avda. Dr. Moliner 50, E-46100 Burjassot (Valencia), Spain
[49] Institut für Hochenergiephysik, Österr. Akad. d. Wissensch., Nikolsdorfergasse 18, A-1050 Vienna, Austria
[50] Inst. Nuclear Studies and University of Warsaw, Ul. Hoza 69, PL-00681 Warsaw, Poland
[51] Fachbereich Physik, University of Wuppertal, Postfach 100 127, D-42097 Wuppertal, Germany
[52] On leave of absence from IHEP Serpukhov

1 Introduction

This paper summarizes the searches for neutral and charged Higgs bosons performed in the data sample collected in 1996 by the DELPHI detector at centre-of-mass energies of 161 GeV and 172 GeV. After an introduction concerning the signal properties, the data samples and the experimental setup, the analyses for each final state are described in Sections 2 to 5 for the neutral Higgs bosons and in Section 6 for the charged Higgs particles. The results are presented in Section 7.

1.1 Signal production and decay

Despite the great success of the electroweak predictions of the Standard Model (SM), its crucial scalar sector remains unprobed. It may be only an effective theory valid at the low energies probed so far, but not valid at higher energies. It is therefore sensible to base the Higgs boson searches on more general theories. In the framework of a model with two Higgs field doublets, which is the easiest extension of the scalar sector of the SM, there are five physical Higgs scalars from the Higgs mechanism. Besides two charged Higgs particles, H^+ and H^-, there are two CP-even scalars h and H, with a mixing angle α, and one CP-odd pseudoscalar A. In e^+e^- collisions, these particles are produced mainly via Z exchange in the s-channel. Charged Higgs bosons are pair produced, while there are two complementary production modes for the neutral Higgs particles, $e^+e^- \to hZ$ and $e^+e^- \to hA$. If one production is suppressed by mixing, the other is enhanced. The SM picture with only one neutral Higgs scalar, h, produced in the process $e^+e^- \to hZ$, is included in this description.

Supersymmetry [1] can solve severe problems of the SM such as the naturalness or the hierarchy problems. Its simplest implementation, the minimal supersymmetric extension of the Standard Model (MSSM), is a particular case of a two Higgs field doublet model. The number of free parameters in the scalar sector is only two at tree level, usually chosen to be $\tan\beta$, the ratio of the vacuum expectation values of the two doublets, and m_A. Higher order corrections introduce dependences on other parameters, such as the top quark and the top squark masses. These parameters have an influence on the hZ and hA production cross-sections. As an example, for low $\tan\beta$ values, the hZ mode dominates and the Higgs boson sector is close to that of the SM, while the associated production of hA increases with $\tan\beta$.

In contrast to the SM Higgs boson, the possible mass range for the lightest MSSM neutral Higgs particle is tightly constrained: $m_h \leq 130$ GeV/c^2 [2]. This result includes radiative corrections computed at the two-loop order and uses the experimental value of the top quark mass. For low $\tan\beta$ values the constraint is tighter, $m_h \leq 105$ GeV/c^2 [2], and within the reach of the LEP2 program at its maximum energy. Searches at LEP1 with the DELPHI detector [3] have been turned into lower limits[†] at the 95% confidence level of 39 GeV/c^2 on m_A and 44 GeV/c^2 on m_h in the MSSM. At large $\tan\beta$, the exclusion limit on m_A reaches the kinematic limit of 45 GeV/c^2. In the SM, the 95% confidence level lower limit on m_h based on LEP1 data from the DELPHI detector [4] is 55.7 GeV/c^2.

In both the SM and the MSSM, the dominant decays of such heavy neutral Higgs bosons into standard particles are those into $b\bar{b}$ and $\tau^+\tau^-$ pairs. As an example, in the SM, a 60 GeV/c^2 Higgs scalar has a branching fraction of 85.6% into $b\bar{b}$ and 8.8% into $\tau^+\tau^-$. The search for neutral Higgs bosons described below is thus restricted to the

[†]for $\tan\beta$ above unity, assuming $m_t = 170$ GeV/c^2, $m_{squark} = 1$ TeV/c^2, and two-loop radiative corrections.

dominant final state topologies, four jets or two acollinear jets with either missing energy or a pair of charged leptons. The four-jet signature and the τ channels are expected from both hZ and hA, while the other signatures come from hZ only. Beyond the SM, Higgs bosons can decay into a pair of invisible products (e.g. a pair of lightest supersymmetric particles), and can be detected only through the hZ mode.

In contrast to the hZ and hA cross-sections, the production cross-section of the charged Higgs boson depends only on its mass in any model with two Higgs field doublets, while its decay branching ratios are model dependent. An analysis in the general two-doublet scheme is thus possible. Previous results from DELPHI [5], based on LEP1 data, excluded charged Higgs bosons of mass up to 43.5 GeV/c^2 at the 95% confidence level. At such masses, there are only two decay channels, into either a cs or a $\tau\nu_\tau$ pair. This leads to three possible final states: four jets, two jets and one tau lepton, or a pair of tau leptons. All three final states have been investigated.

1.2   Experimental setup

The detector consists of a cylindrical part covering the barrel region (with polar angle, θ, typically from 40° to 140°) and two end caps covering the forward regions. A large superconducting solenoid provides a magnetic field of 1.2 T inside the central tracking volume. In the barrel region, tracks of charged particles are reconstructed in the microvertex detector, the inner detector, the time projection chamber and the outer detector, reaching an average momentum resolution $\sigma(1/p)$ of 0.57×10^{-3} (GeV/c)$^{-1}$ for 45 GeV/c muons. In the forward region, the reconstruction is achieved by the time projection chamber, the inner detector and the forward drift chambers, with a momentum resolution of 1.31×10^{-3} (GeV/c)$^{-1}$. The polar angle acceptance of the whole tracking system is $20° < \theta < 160°$.

The microvertex detector, as well as improving the momentum resolution by a factor of two, also provides precise measurements of impact parameters and secondary vertices. As compared to the setup described in [6], the three layers of the microvertex detector have been extended down to 25° in θ. Typical precisions of the impact parameter measurements are $26\mu m$ in the transverse plane, and $47\mu m$ along the beam direction for tracks emitted at 90° in θ. The time projection chamber can also provide charged particle identification by measurement of the energy loss, which is most useful in the low momentum range, below the domain covered by the ring imaging Cherenkov detectors.

Neutral and charged particle energies are measured in the electromagnetic and hadronic calorimeters, whose coverage in θ starts at 8° and 11° respectively. The energy resolutions are $0.32/\sqrt{E}$ and $0.12/\sqrt{E}$ in the barrel and forward electromagnetic calorimeters respectively, where E is expressed in GeV, and $1.3/\sqrt{E}$ in the hadron calorimeter. Particles emitted at angles below 10° are detected in the small angle calorimeter devoted to luminosity measurement, whose acceptance lies between 1.69° and 10.8°. The hermeticity of the electromagnetic calorimetry is improved by photon taggers which cover the gap between the barrel and forward regions at $\theta \simeq 40°$, the weak region at $\theta \simeq 90°$ and some azimuthal gaps in the barrel calorimeter acceptance.

Finally, muons are identified by their penetration through the iron yoke of the hadron calorimeter to planes of drift chambers located partly inside and partly outside the yoke. The barrel region is equipped with three planes of drift chambers while the end caps contain two planes. One surrounding layer of limited streamer tubes completes the coverage between the barrel and forward regions at $\theta \simeq 50°$.

More details about the apparatus and its performance can be found in references [6,7].

1.3   Data samples

The integrated luminosities collected in 1996 are 10.0 pb^{-1} at 161.3 GeV, 1.1 pb^{-1} at 170.3 GeV and 8.9 pb^{-1} at 172.3 GeV. No distinction is made in the analysis between the last two energies. Background simulations are normalised to the luminosities corresponding to good running of the time projection chamber, that is 9.9 pb^{-1} at 161 GeV and 10.0 pb^{-1} at 172 GeV. In the missing energy channels (sections 3, 6.1 and 6.2), good running of the calorimeters is also required and the useful luminosities are 9.7 pb^{-1} at 161 GeV and 10.0 pb^{-1} at 172 GeV.

The selection criteria were defined using simulated data samples of the signal and background processes. Initial state radiation, which produces energetic photons at centre-of-mass energies above the Z peak, is included in all generators. Signal events from neutral Higgs boson production were generated using the HZHA program [8]. The t-channel production of the CP-even scalar h in the neutrino and electron channels ('fusion diagrams'), which has an important effect only close to the kinematic limit, is not included in the simulation.

Samples were generated for the hZ channels h$\mu^+\mu^-$, he^+e^-, h$\nu\bar{\nu}$ and h$q\bar{q}$ with a Higgs boson h decaying into known particles according to SM branching fractions. Samples for the hZ channels with τ leptons were generated in the $(h \to \tau^+\tau^-)(Z \to q\bar{q})$ and $(h \to b\bar{b}, c\bar{c})(Z \to \tau^+\tau^-)$ channels. Table 1 summarizes the cross-sections [9] and Higgs boson branching fractions [10] for the masses used in the generation. Additional samples were generated at the same masses for Z decaying into hadrons and h giving invisible products. For the hA production, samples were generated either with no restriction on the Higgs boson decay modes or assuming one of them to decay into $\tau^+\tau^-$ and the other into b$\bar{b}$. Most samples assume a large $\tan\beta$, i.e. 20, for which h and A have almost equal masses. Table 2 presents the different cross-sections [8] at $\tan\beta = 20$ for the masses used in the generation.

Signal events from charged Higgs bosons were generated with PYTHIA [11] for $m_{H^\pm}$ ranging from 41 to 60 GeV/c^2 in steps of 1 GeV/c^2. Zero width is assumed for the Higgs boson. The three expected topologies, $c\bar{s}c\bar{s}$, $cs\tau\nu_\tau$, and $\tau^+\nu_\tau\tau^-\bar{\nu}_\tau$, were generated separately. The generation of the purely leptonic topology includes the τ polarisation [12]. The different masses considered in the generation and the corresponding cross-sections [13] are presented in Table 3.

The different backgrounds are summarized in Table 4. Final states with two fermions were generated with PYTHIA [11], except $e^+e^-(\gamma)$ events for which the generator of Ref. [14] was used. Four-fermion final states from the ZZ (that is $(Z/\gamma)^*(Z/\gamma)^*$), WW, Weν and Zee processes were also generated with PYTHIA [11]. Two-photon interactions were generated with TWOGAM [15] for hadronic final states, BDK [16] for electron final states and BDKRC [16] for other leptonic final states.

The generated events were passed through JETSET 7.4 [11], tuned to LEP1 data, for quark fragmentation and then through the full simulation and reconstruction programs [6] of the experiment.

1.4   Particle selection

In all analyses, charged particles are selected if their momentum is greater than 100 MeV/c and if they come from the interaction region within 10 cm along the beam direction and within 4 cm in the transverse plane. The $\pi^\pm$ mass is assumed for all charged particles except identified leptons. Unless explicitly stated otherwise, the charged particle momentum is always estimated from the response of the tracking devices. Neutrals are

$m_{\rm h}$ (GeV/c^2)	45	50	55	60	65	70	75	80
σ (pb) at $\sqrt{s}$ =161 GeV	1.91	1.64	1.36	1.04	0.66	0.16	-	-
σ (pb) at $\sqrt{s}$ = 172 GeV	1.64	1.48	1.31	1.13	0.94	0.73	0.49	0.17
Br(h $\to$ b$\bar{\rm b}$) (%)	87.0	86.7	86.4	86.1	85.7	85.3	84.9	84.4
Br(h $\to \tau^+\tau^-$) (%)	7.34	7.46	7.57	7.67	7.76	7.84	7.90	7.96

Table 1: Total SM hZ cross-sections at $\sqrt{s}$ = 161 GeV and $\sqrt{s}$ = 172 GeV for the Higgs boson masses used in the generation. Also quoted are the Higgs boson branching fractions into b$\bar{\rm b}$ and $\tau^+\tau^-$.

$m_{\rm A}$ (GeV/c^2)	45	50	55	60	65	70
σ (pb) at $\sqrt{s}$ = 161 GeV	0.687	0.502	0.382	0.278	0.184	-
σ (pb) at $\sqrt{s}$ = 172 GeV	0.59	0.446	0.356	0.276	0.202	0.136
Br(hA $\to$ b$\bar{\rm b}$b$\bar{\rm b}$) (%)	84.9	84.7	84.5	84.4	84.2	84.0
Br(hA $\to \tau^+\tau^-$b$\bar{\rm b}$) (%)	13.7	13.9	14.1	14.3	14.5	14.7

Table 2: Total hA cross-sections at $\sqrt{s}$ = 161 GeV and $\sqrt{s}$ = 172 GeV in the MSSM at $\tan\beta = 20$, for the Higgs boson masses used in the generation. Also quoted are the fractions of b$\bar{\rm b}$ b$\bar{\rm b}$ and $\tau^+\tau^-$ b$\bar{\rm b}$ final states.

$m_{\rm H\pm}$ (GeV/c^2)	42	44	46	48	50	52	54	56	58	60
σ (pb)	0.94	0.84	0.75	0.69	0.63	0.57	0.52	0.46	0.41	0.35

Table 3: Total H$^+$H$^-$ cross-sections at $\sqrt{s}$ = 161 GeV in the two-doublet scheme, for some of the Higgs boson masses used in the generation. Initial state radiation and vertex corrections are included in the cross-section.

$\sqrt{s}$ = 161 GeV								
process	q$\bar{\rm q}(\gamma)$	$\gamma\gamma \to$ had.	WW	Weν	ZZ	Zee	$\gamma\gamma \to$ lep.	e$^+$e$^-(\gamma)$	ll(γ) l$\neq$e
σ (pb)	147.2	10042	3.4	0.4	0.41	6.3	4490	1644	23
L (pb^{-1})	435	29	3244	1392	3275	530	38	45	203
$\sqrt{s}$ = 172 GeV								
process	q$\bar{\rm q}(\gamma)$	$\gamma\gamma \to$ had.	WW	Weν	ZZ	Zee	$\gamma\gamma \to$ lep.	e$^+$e$^-(\gamma)$	ll(γ) l$\neq$e
σ (pb)	121	10761	12.28	0.48	1.15	6.8	4453	1442	9.7
L (pb^{-1})	519	29	982	860	1677	535	33	161	287

Table 4: Cross-sections and equivalent integrated luminosities of the simulated background samples used in the Higgs boson searches.

defined as energy clusters in the calorimeters unassociated with charged particle tracks. All neutrals of energy greater than 100 MeV are selected. Possible additional requirements in some analyses are described in the relevant sections. Jet reconstruction uses neutral and charged particles, whatever the jet algorithm.

1.5 b-tagging

Due to the high branching fraction of neutral Higgs bosons into b$\bar{\text{b}}$ pairs, b-tagging is a powerful tool to distinguish between signal and background. It is based on the precise reconstruction of the primary vertex position and of the impact parameters of charged particle tracks with respect to it.

The primary vertex is reconstructed for every event using the position of the interaction region as a constraint. The position of the interaction region is measured using high precision probes, and the alignment of these to the DELPHI frame is redone for each fill using reconstructed vertices. When information from the probes is unavailable the vertices alone are used. The position is averaged over a period of about 30 minutes and has a precision of around 25 μm along the axis pointing towards the centre of LEP and 8 μm in the vertical direction. The impact parameter is defined in the transverse plane to the beam axis, as the distance of closest approach of a charged particle track to the reconstructed primary vertex. The coordinate of the impact parameter along the beam direction z is then defined as the difference in the z coordinate of the point of closest approach in the transverse plane from that of the primary vertex. A sign is given to the impact parameters. It is positive if the vector joining the primary vertex to the point of closest approach is at less than 90° from the direction of the jet to which the track belongs.

Signed impact parameters are converted into b-tagging information through the probabilistic tagging technique described in [6] and [17]. The method is calibrated on hadronic decays of the Z boson collected at the Z resonance peak just before the 161 and 172 GeV runs. Only tracks with negative impact parameters are used for calibration to select impact parameters mainly due to detector effects. The tagging variables then measure the probability of a given set of tracks to be consistent with the primary vertex. Different tagging variables are defined, such as the event probability computed from tracks with positive impact parameters only, P_E^+. The event probability from impact parameters of any sign, P_E, is sometimes used to allow for redundancy. Jet probabilities (P_{jet}^+) are also defined and computed from the tracks in the jet with positive impact parameters. The selection is often applied to minus the logarithm of the tagging variables. As an example, Figure 1 shows the b-tagging efficiency as a function of the minimal value required for the event variable, $-\log_{10}(P_E^+)$, for simulated WW, q$\bar{\text{q}}(\gamma)$, hZ and hA events at high energy [17].

2 Neutral Higgs boson searches in events with jets and electrons or muons

The h$\mu^+\mu^-$ and he$^+$e$^-$ channels represent 6.7% of the hZ final states. The experimental signature is a pair of jets recoiling against a pair of high momentum and isolated leptons where the invariant mass of the lepton pair is close to the Z mass.
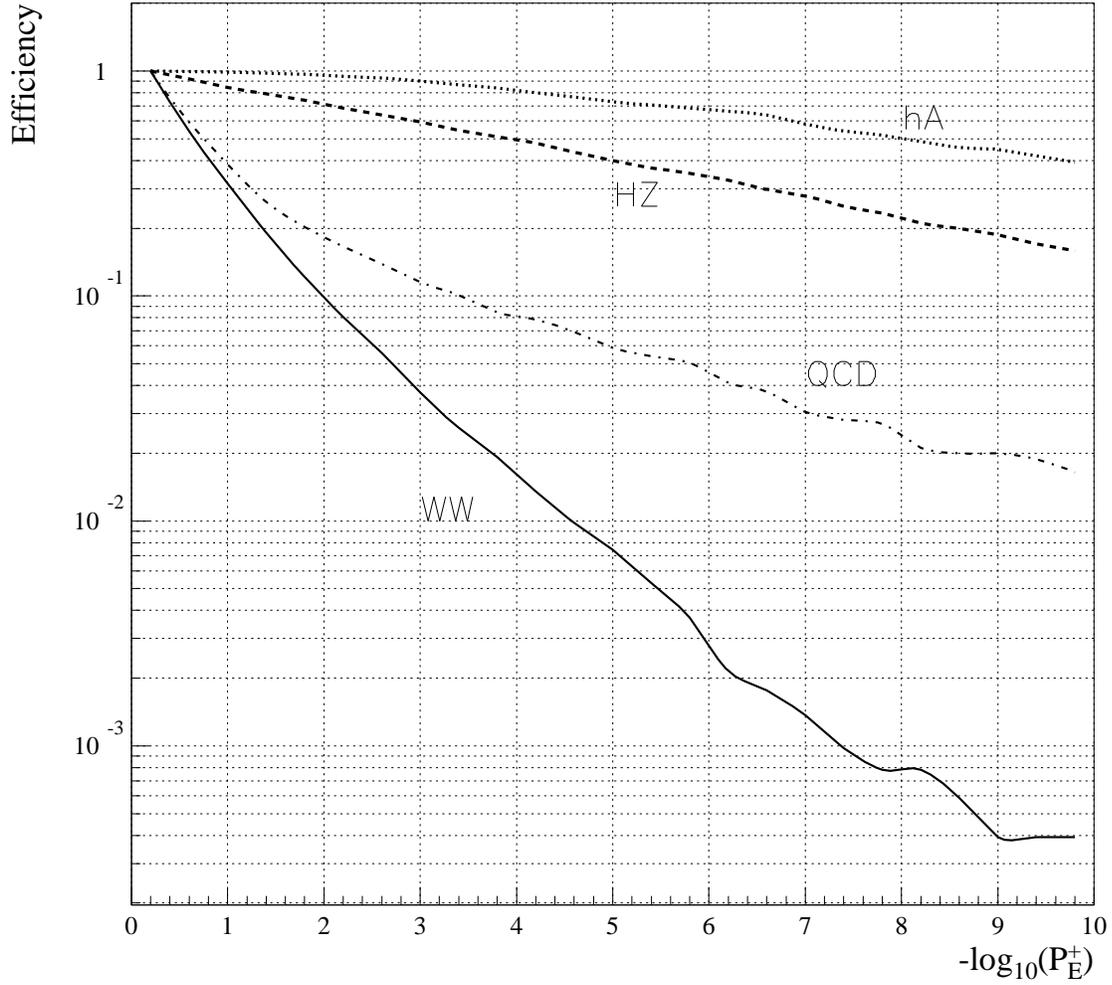
DELPHI

Figure 1: Performance of the probabilistic b-tagging: efficiency of the b-tagging requirement based on a minimal value of $-\log_{10}(P_E^+)$, as a function of this value. The efficiency is within the acceptance of the vertex detector. Curves are shown for simulated hadronic 4-jet events from WW pairs and $q\bar{q}(\gamma)$ background events (labelled 'QCD'), and from hZ and hA signal events. Centre-of-mass energies of 161 and 172 GeV give similar results and have been combined.

2.1 Lepton identification and jet reconstruction

Muon identification is provided primarily by the algorithm described in [6] which relies on the association of charged particle tracks to signals in the barrel and forward muon chambers. Depending on the severity required to validate the association, four tag levels are defined. The analysis uses only the two less severe levels, called very loose and loose, which provide an identification efficiency within the acceptance of the barrel and forward muon chambers of 96% and 95% respectively, with a probability of misidentifying a pion for a muon of 5.4% and 1.5% respectively. The same algorithm has been also extended to the surrounding muon chambers. If the identification in the muon chambers fails, charged particles are flagged as muons if the longitudinal profile of their energy deposit in the hadron calorimeter is compatible with that expected from a minimum ionizing particle. The inclusion of this additional information leads to an improvement of the overall muon detection efficiency from 90% to 98% within the acceptance of the tracking detectors, with a misidentification probability slightly increased from 5.4% to 6.5%.

A specific electron identification algorithm was developed for Higgs boson searches with emphasis on efficiency rather than purity, since electrons in the hZ channel are expected to be isolated. Electrons are identified as charged particle tracks with an energy deposit above 3 GeV in the electromagnetic calorimeter, below 5 GeV in the hadronic calorimeter and with a ratio of calorimeter energy to momentum from tracking above 0.3. A charged particle track pointing to an insensitive calorimeter region is also accepted provided it is not identified as a muon and either is associated to a hit in the hermeticity taggers or has an energy loss in the time projection chamber in agreement with that expected for an electron. In both cases, electrons from gamma conversion in the outer wall of the time projection chamber (TPC) or in the ring imaging Cherenkov detectors are rejected by requiring the track reconstruction to include points in the TPC or, if the particle passes between the modules of the TPC, points both in the microvertex and inner detectors. The energy of an electron candidate is defined by the calorimeter energy, except if the track points to an insensitive region of the calorimeters, in which case the momentum given by the tracking detectors is used. The electron identification efficiency is 94% within the acceptance of the tracking system and the probability of misidentifying a pion as an electron is 16%. When restricting to tracks linked to an electromagnetic shower, the efficiency is 83% and the misidentification probability is 13%.

2.2 Muon channel

Candidates for $e^+e^- \rightarrow h\mu^+\mu^-$ are selected by requiring at least five charged particles in the barrel acceptance and a total energy from charged particles above $0.12\sqrt{s}$. Among the charged particles, two must have opposite charges and momenta greater than 22 GeV/c. This defines the preselection. All pairs of particles satisfying these criteria are possible dilepton candidates. Each pair is considered in turn and muon identification is required either for both particles of the pair, in which case any identification level is accepted, or for only one particle, in which case the identified muon must be tagged as loose by the identification algorithm. A search for jets is then performed in the system recoiling from the muon pair, using the Durham algorithm [18] with a resolution parameter set to 0.12, which was shown to give the best efficiency and background reduction in this channel. Events are selected if at least two jets are reconstructed and the second most energetic jet consists of at least three charged particles. This last criterion is introduced to avoid fake jets due to noise or to photons showering in the detector. After this

step, the $\gamma\gamma$, Zee and Weν backgrounds are totally suppressed. Finally, the two muon candidates are required to be isolated at more than 9° with respect to the closest jet.

$\sqrt{s} = 161$ GeV								
selection	data	total background	$q\bar{q}(\gamma)$	ZZ	WW	Zee Weν	$l^+l^-(\gamma)$	$\gamma\gamma$	h$\mu^+\mu^-$ $\varepsilon(\%)$
hadronic	1910	1640 ± 11	1326	3.39	30.2	31.3	150	98.1	95.2
preselection	89	95.8 ± 5.2	40.2	0.410	1.02	1.53	51.8	0.89	81.0
$\mu^+\mu^-$ id.	6	2.51 ± 0.31	1.62	0.207	0.356	0	0.33	0	80.7
jets	4	1.86 ± 0.26	1.44	0.140	0.282	0	0	0	76.6
isolation	1	0.53 ± 0.12	0.32	0.118	0.098	0	0	0	74.8
5C Fit	0	0.039 ± 0.011	0	0.036	0.003	0	0	0	71.8
$\sqrt{s} = 172$ GeV								
selection	data	total background	$q\bar{q}(\gamma)$	ZZ	WW	Zee Weν	$l^+l^-(\gamma)$	$\gamma\gamma$	h$\mu^+\mu^-$ $\varepsilon(\%)$
hadronic	1655	1479 ± 9.7	1084	8.65	110	24.8	155	95.4	95.4
preselection	109	113 ± 4.2	44.3	0.935	4.74	0.72	60.6	1.74	79.2
$\mu^+\mu^-$ id.	9	5.26 ± 0.53	2.96	0.428	1.48	0.13	0.255	0	78.7
jets	8	4.42 ± 0.48	2.72	0.332	1.33	0	0.037	0	75.5
isolation	2	1.03 ± 0.19	0.40	0.265	0.360	0	0	0	73.5
5C Fit	0	0.126 ± 0.030	0	0.084	0.041	0	0	0	69.8

Table 5: Analysis of the h$\mu^+\mu^-$ channel: effect of the selections at $\sqrt{s} = 161$ GeV and $\sqrt{s} = 172$ GeV on data, simulated backgrounds and simulated signal events with m_{h} = 60 GeV/c^2 at 161 GeV and m_{h} = 70 GeV/c^2 at 172 GeV. Efficiencies are given for the signal.

To account for the specific kinematics of the signal, with the muon pair arising from an on-shell Z boson, a kinematic fit [19] is applied to the selected events. In addition to total energy and momentum conservation, the fit requires the mass of the muon pair to be consistent with m_{Z}, taking into account the Breit-Wigner shape of the Z resonance. Events are kept if the probability of the fit is higher than 10^{-10}. Table 5 details the effect of the selections on data and simulated samples of background and signal events. The agreement of simulation with data is good after the preselection. This can also be seen in Figure 2, which shows the distributions of the muon momenta and isolation angles at 161 GeV. The preselection has been applied with a looser requirement on the momenta at 15 GeV/c to select larger data samples. As the preselection does not include muon identification, other charged particles also contribute.

At the end of the analysis, the expected background comes mainly from ZZ and WW events, and amounts to $0.04 \pm 0.01(stat.) \pm 0.01$ ($syst.$) events at 161 GeV and to 0.13 ± 0.03 ($stat.$) ± 0.01 ($syst.$) events at 172 GeV. No event is selected in the data. The mass resolution is illustrated in Figure 3 which shows the distributions of the Z and Higgs boson masses in simulated signal events at 161 GeV. The Z mass is given by the mass of the muon pair and the Higgs boson mass by the recoiling mass to the muon pair, both masses taken after the kinematic fit. Table 6 gives the signal efficiencies. The decrease
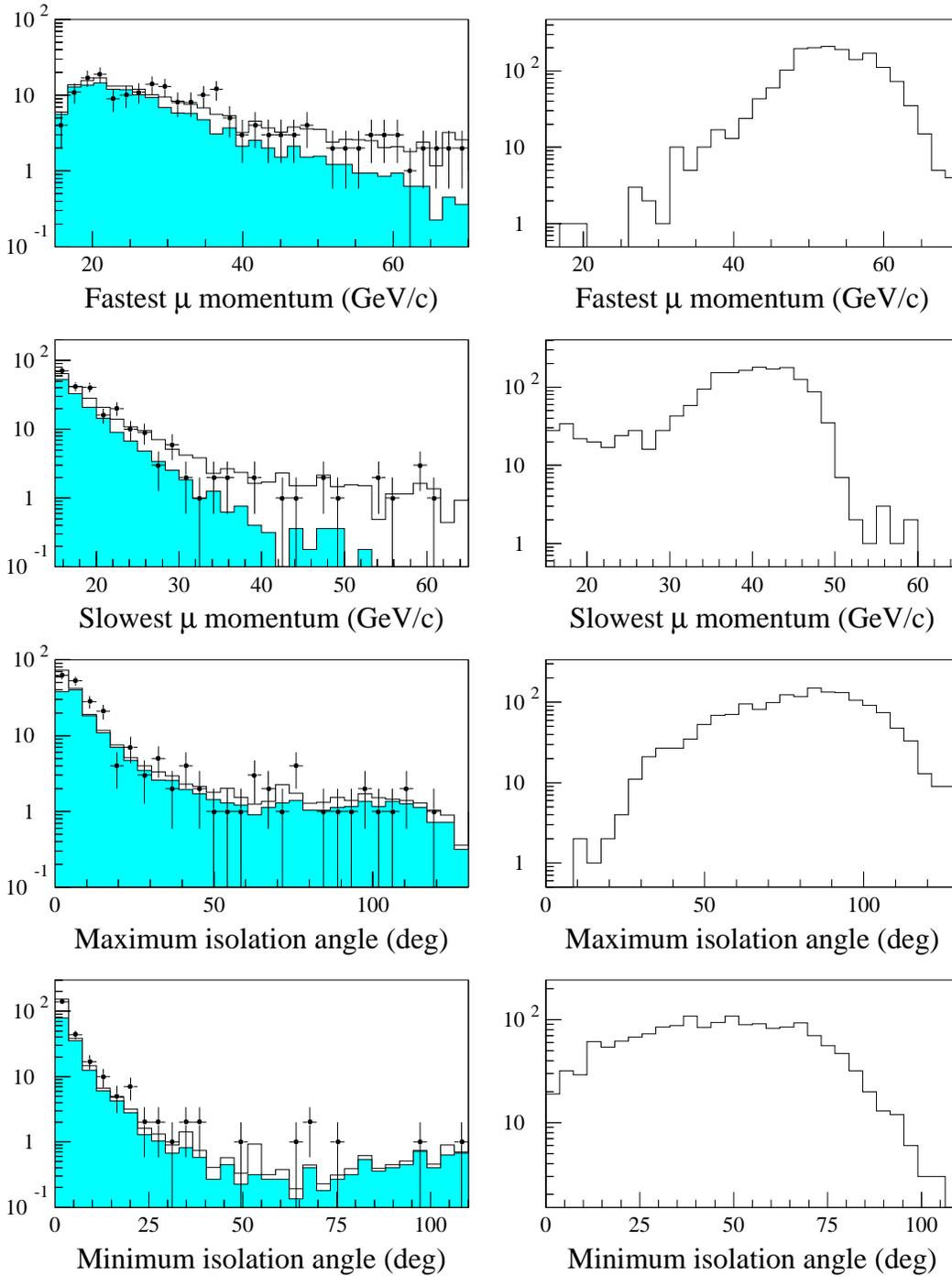
DELPHI - √s = 161 GeV

Figure 2: $h\mu^+\mu^-$ channel: distributions of some analysis variables as described in the text. Plots on the left show a comparison between 161 GeV data and simulated background events (solid line) normalised to the experimental luminosity. The shaded area represents the contribution of the dominant $q\bar{q}(\gamma)$ background. Plots on the right show the (unnormalised) expected distributions for a Higgs boson of 60 GeV/c^2.
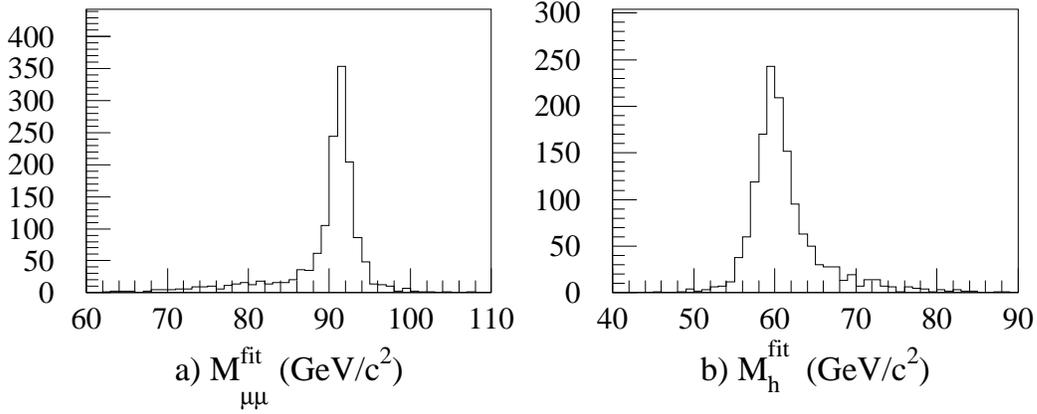
DELPHI - √s = 161 GeV

Figure 3: $h\mu^+\mu^-$ channel: distributions of (a) the Z mass and of (b) the Higgs boson mass at the end of the analysis for simulated $h\mu^+\mu^-$ events with $m_h = 60$ GeV/c^2 at 161 GeV.

m_h (GeV/c^2)	Efficiency at 161 GeV (%)	Efficiency at 172 GeV (%)
45	$56.9 \pm 1.1\ ^{+0.6}_{-0.7}$	$49.3 \pm 1.3\ ^{+0.6}_{-0.5}$
50	$64.7 \pm 1.1\ ^{+0.7}_{-0.7}$	$57.8 \pm 1.3\ ^{+0.7}_{-0.7}$
55	$67.8 \pm 1.0\ ^{+0.8}_{-0.7}$	$65.6 \pm 1.2\ ^{+0.7}_{-0.7}$
60	$71.8 \pm 1.0\ ^{+0.7}_{-0.8}$	$67.0 \pm 1.2\ ^{+0.7}_{-0.7}$
65	$73.0 \pm 1.0\ ^{+0.7}_{-0.8}$	$70.3 \pm 1.2\ ^{+0.8}_{-0.8}$
70	$69.0 \pm 1.0\ ^{+0.9}_{-0.9}$	$69.8 \pm 1.2\ ^{+0.8}_{-0.9}$
75	-	$72.4 \pm 1.2\ ^{+0.8}_{-0.8}$
80	-	$72.2 \pm 1.2\ ^{+0.8}_{-0.8}$

Table 6: Efficiency of the Higgs boson selection in the $h\mu^+\mu^-$ channel at $\sqrt{s} = 161$ GeV and $\sqrt{s} = 172$ GeV, as a function of the mass of the Higgs boson. The first uncertainty quoted is statistical, the second is systematic.

of the efficiency at low mass is due to the larger boost of the Higgs boson which makes the requirements on the number of jets and jet multiplicities less efficient.

The systematic uncertainties have been derived in the following way. The main source of systematic effects is expected to be the imperfect simulation of the detector response. The agreement of real and simulated distributions for the analysis variables was carefully checked at the hadronic preselection level, and no crucial discrepancy was found. The systematic uncertainties have been estimated by varying the selections on all continuous variables by the difference between the average values of the corresponding distributions in real and simulated samples and adding in quadrature the corresponding changes in the efficiencies. To account for possible differences between data and simulation in the muon identification, a relative 1% uncertainty [6] has been added in quadrature to get the final systematic uncertainties in the efficiencies. The changes in the selections have no effect on the expected background which might be due to the limited size of the simulated samples. Such a problem is expected to arise when dealing with so low a background. To check for a possible bias, a different estimator of the background was tried. Muon identification was removed from the selection and, for each background process, the background after the remaining selections was multiplied by the efficiency of the muon identification step, taken from table 5. This leads to $q\bar{q}(\gamma)$ backgrounds of 0.014 ± 0.005 (*stat.*) events at 161 GeV and 0.05 ± 0.02(*stat.*) events at 172 GeV, and to total backgrounds of 0.05 ± 0.01 (*stat.*) events at 161 GeV and 0.12 ± 0.02 (*stat.*) events at 172 GeV. Although the total backgrounds agree statistically with the estimates in Table 5, a systematic uncertainty of ± 0.01 events, coming from the difference between the two estimates at 161 GeV, has been attributed to the expected backgrounds.

2.3 Electron channel

Candidates for $e^+e^- \rightarrow he^+e^-$ are preselected as in the $h\mu^+\mu^-$ channel. Among the charged particles of the event, two are required to have a momentum above 4 GeV/c and must either be associated to a shower in the electromagnetic calorimeter or point to an insensitive calorimeter region. This defines the preselection. All pairs of particles satisfying the last criterion are then considered in turn. Electron identification is applied to both particles of the pair, with the restriction that the two particles are not allowed to point simultaneously to insensitive calorimeter regions. Events are kept if at least two electron candidates are found, with opposite charges, with an isolation angle greater than $5°$ from any other charged particle and with a total energy deposit in the electromagnetic calorimeters above 20 GeV.

A search for jets is performed in the system recoiling from the electron pair using the LUCLUS algorithm [20] with the resolution parameter kept to its default value of 2.5 GeV/c. Events are selected if at least two jets are reconstructed and the second most energetic jet contains at least two charged particles. Both electron energies are required to be above 15 GeV. The mass of the electron pair, obtained after a global kinematic fit [19] imposing total energy and momentum conservation, must be above 50 GeV/c^2, or above 30 GeV/c^2 if the kinematic fit gives a χ^2 probability below 10%. The system recoiling from the electron pair is forced to two jets in the fit. Electron isolation angles with respect to the closest jet are required to be more than $15°$ for the most isolated electron and more than $8°$ for the other. As the search is restricted to high mass Higgs bosons, the mass of the recoiling system as given by the kinematic fit is required to be above 40 GeV/c^2. Finally, to reject events with particles escaping detection in the forward region, the longitudinal component of the missing momentum must be below 30 GeV/c.

At 172 GeV, the analysis is completed by a loose event b-tagging in order to keep the background at an acceptable level, despite the increase of the WW and ZZ production cross-sections. The b-tagging selection requires the smaller of P_E^+ and P_E to be below 0.3.

Figure 4 shows the distributions of the main analysis variables after preselection, for 172 GeV data, simulated backgrounds and simulated signal events at 70 GeV/c^2. The agreement between data and background expectation is satisfactory.

$\sqrt{s} = 161$ GeV										
selection	data	total bg.	$q\bar{q}(\gamma)$	$ll(\gamma)$	WW	Zee	ZZ	Weν	$\gamma\gamma$ $\to$ had.	he$^+$e$^-$ $\varepsilon(\%)$
hadronic	1910	1613±21	1325.9	136.8	30.2	19.1	3.40	2.65	94.7	95.8
presel.	966	850±11	767.8	30.3	19.0	10.32	2.16	1.08	18.6	85.1
e$^+$e$^-$ id.	12	12.4±2.5	8.13	2.48	0.49	1.01	0.25	0.007	0	54.2
jets	9	9.13±0.71	7.50	0	0.49	0.91	0.23	0	0	52.5
e momenta	1	0.52±0.09	0.10	0	0.04	0.28	0.09	0	0	44.3
m_Z constraint	1	0.29±0.07	0.07	0	0.02	0.15	0.05	0	0	43.6
isol.,M_{rec}, P_z	0	0.13±0.04	0	0	0.02	0.08	0.04	0	0	41.7
$\sqrt{s} = 172$ GeV										
selection	data	total bg.	$q\bar{q}(\gamma)$	$ll(\gamma)$	WW	Zee	ZZ	Weν	$\gamma\gamma$ $\to$ had.	he$^+$e$^-$ $\varepsilon(\%)$
hadronic	1655	1437±13	1068.6	144.7	108.8	20.5	8.46	3.26	83.3	95.3
presel.	855	776.5±4.9	634.9	38.2	71.5	11.9	5.37	1.50	13.4	85.5
e$^+$e$^-$ id.	28	15.0±1.1	7.28	2.14	2.00	1.08	0.42	0.03	2.00	51.6
jets	22	12.34±0.87	6.91	0.72	1.96	0.95	0.39	0.03	1.37	49.9
e momenta	2	1.58±0.37	0.55	0	0.17	0.35	0.17	0	0.34	43.0
m_Z constraint	2	1.13±0.36	0.34	0	0.12	0.23	0.10	0	0.34	42.9
isol.,M_{rec}, P_z	0	0.31±0.06	0.07	0	0.05	0.15	0.05	0	0	40.7
b-tagging	0	0.20±0.05	0.05	0	0.01	0.12	0.02	0	0	37.2

Table 7: Analysis of the he$^+$e$^-$ channel: effect of the selections at $\sqrt{s} = 161$ GeV and $\sqrt{s} = 172$ GeV on data, simulated backgrounds and simulated signal events with $m_h = 60$ GeV/c^2 at 161 GeV and $m_h = 70$ GeV/c^2 at 172 GeV. Efficiencies are given for the signal.

Table 7 shows the effect of the selections on data, simulated background and signal events. Backgrounds not quoted in the table (two-photon processes leading to leptonic final states) are negligible. The final background amounts to 0.13±0.04 ($stat.$)±0.02 ($syst.$) events at 161 GeV and to 0.20 ± 0.05 ($stat.$) ± 0.03 ($syst.$) events at 172 GeV, and is mainly due to Zee events. No event is selected in the data. Figure 5 illustrates the resolution in the Z and Higgs boson masses in simulated signal events at 172 GeV. As in the previous channel, the Z mass is estimated as the mass of the electron pair and the Higgs boson mass is the recoiling mass from the electron pair, both masses given by the kinematic fit.
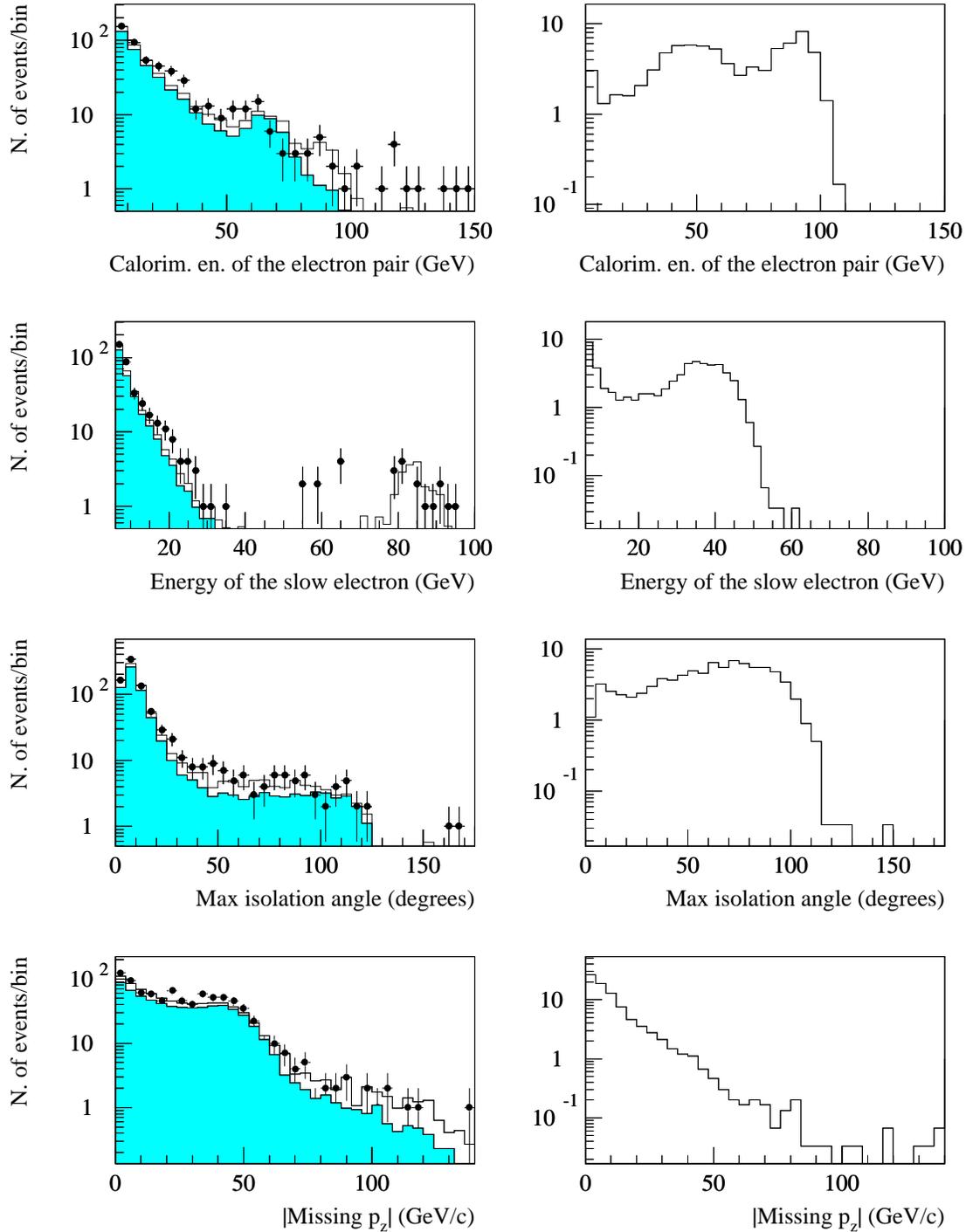
DELPHI - √s = 172 GeV

Figure 4: he$^+$e$^-$ channel: distributions of some analysis variables as described in the text. Plots on the left show a comparison between 172 GeV data (dots) and simulated events (solid line) normalised to the experimental luminosity. Plots on the right show the (unnormalised) expected distributions for a 70 GeV/c^2 Higgs boson.
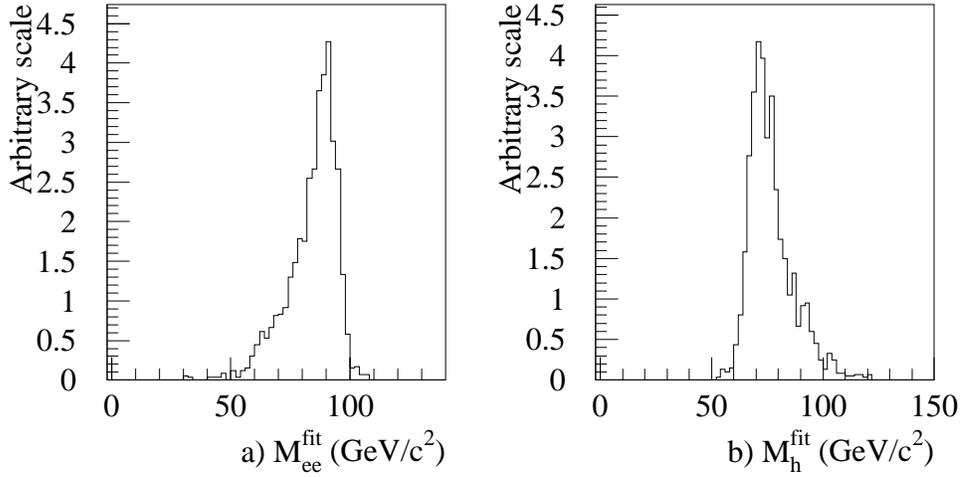
DELPHI - √s = 172 GeV

Figure 5: he$^+$e$^-$ channel: distributions of (a) the Z mass and of (b) the Higgs boson mass at the end of the analysis for simulated he$^+$e$^-$ events with $m_h = 70$ GeV/c^2 at 172 GeV.

m_h (GeV/c^2)	Efficiency at 161 GeV (%)	Efficiency at 172 GeV (%)
45	$38.0 \pm 0.9^{+1.2}_{-2.5}$	$36.1 \pm 0.9^{+0.6}_{-1.3}$
50	$39.0 \pm 0.9^{+0.8}_{-1.3}$	$36.3 \pm 0.9^{+0.6}_{-1.3}$
55	$42.9 \pm 0.9^{+0.6}_{-1.2}$	$37.1 \pm 0.9^{+0.6}_{-1.4}$
60	$41.5 \pm 0.9^{+0.6}_{-1.3}$	$36.2 \pm 0.9^{+0.5}_{-1.3}$
65	$42.0 \pm 0.9^{+0.5}_{-1.2}$	$36.7 \pm 0.9^{+0.6}_{-1.4}$
70	$41.7 \pm 0.9^{+0.8}_{-1.4}$	$37.2 \pm 0.9^{+0.7}_{-1.2}$
75	-	$38.4 \pm 0.9^{+0.6}_{-1.3}$
80	-	$36.6 \pm 0.9^{+0.7}_{-1.4}$

Table 8: Efficiency of the Higgs boson selection in the he$^+$e$^-$ channel at $\sqrt{s} = 161$ GeV and $\sqrt{s} = 172$ GeV as a function of the mass of the Higgs boson. The first uncertainty quoted is statistical, the second is systematic.

To derive the systematic error on the background, simulated samples of $e^+e^-q\bar{q}$ final states generated with the EXCALIBUR generator [21] have been used to evaluate the uncertainties due to approximations in the description of the background processes in PYTHIA [11] (e.g. absence of interference, kinematic cuts at generation level). The background was found to be lower than but consistent with the previous estimate. Table 8 shows the selection efficiency. The systematic uncertainties have been evaluated by considering both the difference between data and simulation in the distributions of each analysis variable and the sensitivity of the selection criteria on such variables. The variables included in this procedure are the continuous variables used in the electron identification and in the kinematic requirements. More precisely, after observing (at preselection level) how much the selection value had to be moved in simulation in order to get the same fraction of selected events as in real data, the variation of the efficiency after a positive or negative variation of the same amount was recorded. The sum in quadrature of these differences in efficiency has been taken as an estimate of the systematic error.

3 Neutral Higgs boson searches in events with jets and missing energy

The $h\nu\bar{\nu}$ channel corresponds to 20% of the hZ final states. The experimental signature is a pair of acoplanar and acollinear jets, coming mostly from b quarks, with a recoiling mass compatible with the Z mass. Beyond the SM, a similar topology arises in 69% of the hZ final states in which the Higgs boson decays into a pair of invisible products (the 69% in which the Z decays to $q\bar{q}$). The kinematic difference is that in this case the visible mass is compatible with the Z mass.

Three analyses have been performed in this channel. They gave compatible results. For brevity, only one of them, using a probabilistic approach, is described here. The other two, one using sequential selections with emphasis on a very low background level, and one based on an iterative non-linear discriminant analysis aiming at a high selection efficiency, are described in detail in references [22] and [23], respectively.

3.1 Preselection

Hadronic events are selected by requiring at least five charged particles and a total charged energy over $0.12\sqrt{s}$. Jets in selected events are reconstructed in two ways. Events are divided into two hemispheres with respect to the plane perpendicular to the thrust axis and the particles in each hemisphere are summed up to build what will be referred as 'hemispheric jets'. A jet search is also performed using LUCLUS [20] with the resolution parameter kept to its default value. These jets will be referred as 'jets' in the following.

Typical signal events are characterized by a large missing energy and a missing momentum not aligned with the beam direction, due to the production of the Higgs and Z bosons at large polar angles. In addition, the visible system is most often split into at least two jets. To select such topologies, the event visible mass is required to be below 120 GeV/c^2, each hemispheric jet must contain at least two charged particles and the acoplanarity between the two hemispheric jets must be greater than 2°, where the acoplanarity is defined as the supplement of the angle between the transverse momenta (with respect to the beam axis) of the two jets. At this stage of the analysis, the main backgrounds are $q\bar{q}(\gamma)$ events and two-photon processes leading to hadronic final states. As the latter are easily suppressed by the probabilistic step, due to strong topological

differences with the Higgs boson process, the remaining selections are intended to reduce the contamination from WW pairs and q$\bar{\text{q}}(\gamma)$ events.

Background from WW pairs comes mainly from mixed decays where one W decays hadronically while the other decays leptonically. The corresponding final states contain an energetic and isolated lepton, which is not the case for the signal. A search for isolated particles is performed by computing the total energy lying around the direction of each particle with momentum above 2 GeV/c, whatever its charge. In order to tag also isolated τ leptons or showering electrons, the energy is collected between two cones with half opening angles of 5° and 25°. For particles of momentum between 2 and 5 GeV/c, the opening of the wider cone is enlarged to 60° to prevent a low momentum particle from being tagged as isolated. Events with a particle whose cone energy is below 1 GeV are rejected. This selection halves the WW background and also rejects some q$\bar{\text{q}}(\gamma)$ events since the isolated photons, whether converted or not, can be tagged by this method.

The last two selections reinforce the rejection of events with a radiative photon emitted at large angle from the beam axis. Events with a shower in the electromagnetic calorimeter above 20 GeV are rejected; this is done whether the shower is associated to a charged particle track or not, in order to be sensitive to converted photons. Finally, signals from the hermeticity taggers at 40° and 90° are used to tag the loss of an energetic photon in the insensitive regions of the electromagnetic calorimetry. Signals are considered significant only when coming from well isolated counters, at more than 30° (20°) from the closest jet for the 40° (90°) taggers. Among these signals, the one from the counter closest to the missing momentum direction is considered as due to a particle provided the angular difference between the counter and the missing momentum directions is below 50° in θ and 30° in ϕ for the 40° taggers, or below 20° in ϕ for the 90° taggers. Events with such a signal are rejected.

3.2 Probabilistic step

At the end of the preselection, the remaining background from q$\bar{\text{q}}(\gamma)$, WW and Weν events is topologically close to the signal. This translates into large overlaps between the signal and background distributions of most of the discriminating variables. The probabilistic method is used to combine several of them into one single variable with a better discriminating power. The outline of the method, already used at LEP1 in the h$\nu\bar{\nu}$ channel [4], is only briefly recalled here.

A set of discriminating variables is chosen and each variable is transformed into a new one *uniformly* distributed between 0 and 1 for the background, while its distribution for the signal is asymmetric with an excess *below* 0.5. This is achieved by integrating the variable probability density function over the simulated background events in the appropriate direction and taking the cumulative probability as the new variable [4]. Thus, if X is an initial variable and x a value taken by X, the new variable, $P_X(x)$, measures the probability to observe a value of X greater (or lower, depending on the direction of integration) than x in the background. The variables, once transformed, are summed up to define the global event weight, $\mathcal{W}$, which measures the compatibility of the event with the background. If the number of variables, N, is not too small and the variables are uncorrelated, $\mathcal{W}$ has a Gaussian distribution with known mean ($\mu = N/2$) and known variance ($\sigma^2 = N/12$). In practice, the variables are correlated but the correlations are small so that the shape of the $\mathcal{W}$ distribution can still be approximated by a Gaussian [4].

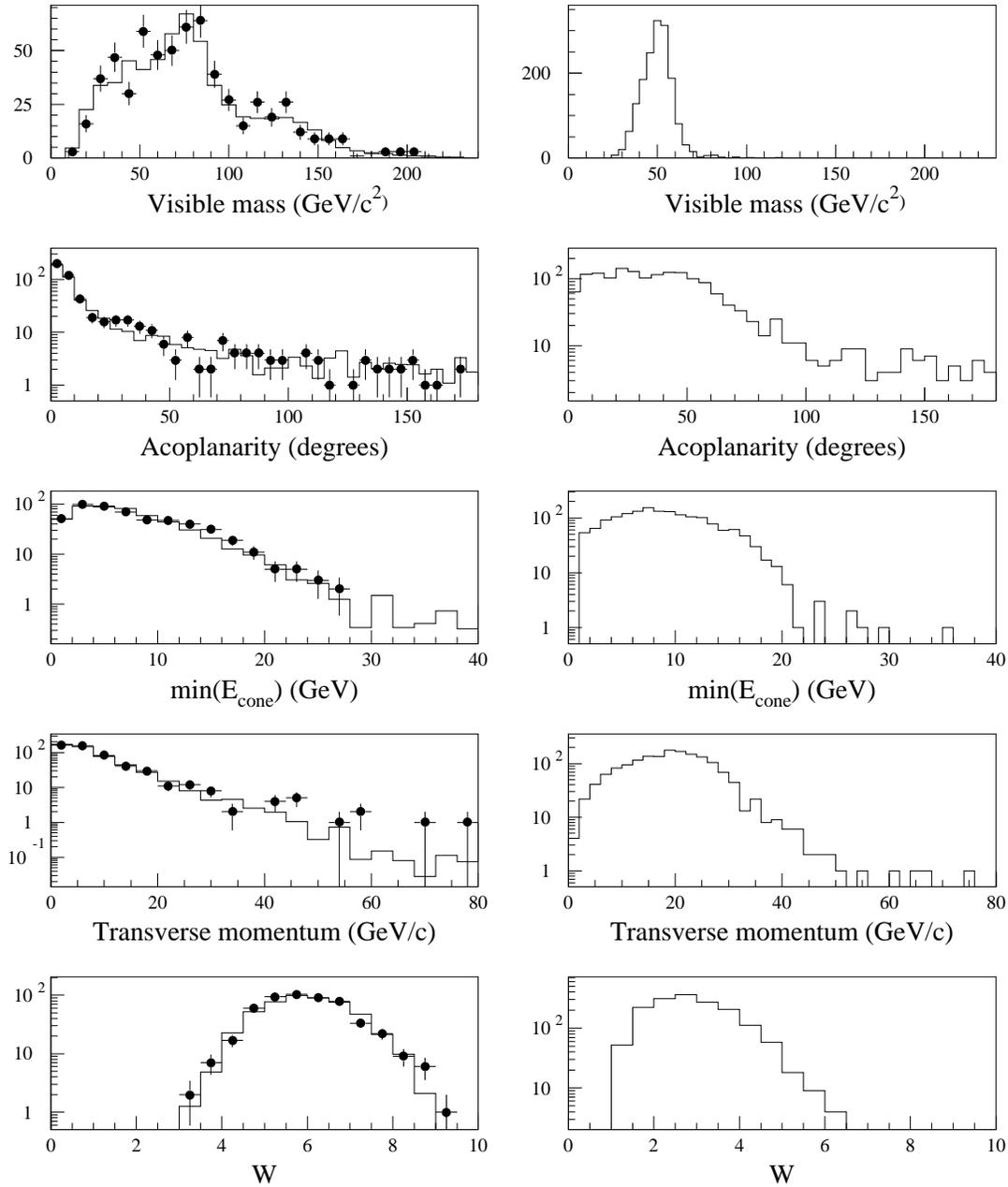**DELPHI - √s = 161 GeV**

Figure 6: h$\nu\bar{\nu}$ channel, probabilistic analysis: distributions of some analysis variables as described in the text. Plots on the left show a comparison between 161 GeV data and simulated background events (solid line) normalised to the experimental luminosity. Plots on the right show the (unnormalised) expected distributions for a Higgs boson of 60 GeV/c^2.

3.3 Content of the event global weight

Twelve discriminating variables are chosen for the analysis in the h$\nu\bar{\nu}$ channel. There are four angular variables: the acoplanarity between the hemispheric jets (α), the polar angle of the thrust axis (θ_{thr}), the angle between the missing momentum direction and the closest jet (λ_{xy}) and the maximum angle between any pair of jets (ρ_{xy}), the event being projected on the plane transverse to the beam axis before the last two variables are computed. There are five global variables: the event transverse momentum with respect to the beam direction (P_t), the event visible mass (M), the event missing mass recoiling against the visible system (M_{rec}), the reduced centre-of-mass energy when the visible system is forced into two jets and a kinematic fit is applied with energy and momentum conservation, assuming a photon to be lost along the beam direction ($\sqrt{s'}$) and the event transverse size in the rest frame of the visible system (σ_{P_t}). The last is defined by dividing the event into two hemispheres with respect to a plane perpendicular to the sphericity axis and computing σ_{P_t} in the hemisphere with the larger number of particles as the r.m.s of the distribution of the particle transverse momenta with respect to the sphericity axis. The last three variables, dedicated against WW and Weν events, are: the minimum cone energy in the event, as defined in the previous section (E_{cone}^{min}), the energy of the most energetic particle in the event or the total energy in the forward electromagnetic calorimeters if it is higher (E_{most}), the b-tagging event variable ($-\log_{10}(P_E^+)$).

The agreement between data and background simulation is illustrated in Figure 6, which shows the distributions of M, α, E_{cone}^{min}, P_t and $\mathcal{W}$ at preselection level, with no mass requirement for the first four distributions. Also shown are the corresponding distributions for signal events at 60 GeV/c^2. The selection on the global event weight is chosen as $\mathcal{W} < 3.3$ which gives efficiencies at the reference masses (60 GeV/c^2 at $\sqrt{s} = 161$ GeV and 70 GeV/c^2 at $\sqrt{s} = 172$ GeV) close to 50%, with reasonable backgrounds at both energies. Table 9 shows the effect of the selections on data, simulated backgrounds and simulated signal events. The last but one column in the table groups the contributions of ll(γ) events and two-photon processes leading to leptonic final states. The main contribution there is from e$^+$e$^-(\gamma)$ events up to the requirement on the visible photon and from processes giving τ leptons in the final state afterwards.

3.4 The h$\nu\bar{\nu}$ channel

When the Higgs boson is assumed to decay according to the SM or to the MSSM, b-tagging provides an additional rejection against background. The b-tagging requirement is $\max(-\log_{10}(P_E^+), -\log_{10}(P_E)) > 1.1$ so that the selection leaves more than 80 % of the signal. As seen in Table 9, after b-tagging, the remaining background is dominated by the q$\bar{\text{q}}(\gamma)$ process and then by Weν events. WW pairs make another source of background only in the 172 GeV data. Table 10 shows the signal efficiencies. The decrease of the efficiency at low mass is due to the requirement on both hemispheric jet multiplicities which is less efficient there due to the larger boost of the Higgs boson. This requirement is however powerful against ZZ events with only one hemispheric jet, which would make a small non-Gaussian tail in the $\mathcal{W}$ distribution in the signal region.

Systematic uncertainties are estimated by comparing the $\mathcal{W}$ distributions in data and simulation at preselection level. In both data and simulation, the distributions are Gaussian with parameters compatible within statistics, as can be seen in Table 11. The means agree quite well with the expected value of 6 while the variances are slightly lower than the expected value of 1. As the shape of the background is predictable, the expected background remaining after the selection on $\mathcal{W}$ can be computed using the Gaussian

$\sqrt{s} = 161$ GeV									
selection	data	total bg.	$q\bar{q}(\gamma)$	$\gamma\gamma$ $\to$ had.	WW	Weν	ZZ	Zee	other bg.	h$\nu\bar{\nu}$ $\varepsilon(\%)$
hadronic	2262	2391 $\pm$ 16	1354	353.0	29.6	2.6	3.4	23.2	625.2	90.0
Mass	1533	1609 $\pm$ 15	845.8	346.0	14.6	2.5	1.4	19.1	379.4	90.0
acoplanarity	873	870 $\pm$ 11	487.7	231.8	13.3	2.4	0.92	7.9	126.1	87.3
no isol. part.	626	580 $\pm$ 9	381.1	182.3	5.5	1.9	0.52	4.3	4.6	82.6
no vis. γ	546	517 $\pm$ 9	326.2	180.2	4.3	1.9	0.47	3.7	0.55	82.3
hermeticity	522	504 $\pm$ 9	318.7	175.0	4.2	1.8	0.45	3.6	0.55	81.2
$\mathcal{W} < 3.3$	2	0.78 $\pm$ 0.11	0.47	0	0.04	0.24	0.02	0	0	56.9
b-tagging	1	0.52 $\pm$ 0.10	0.38	0	0.02	0.10	0.01	0	0	50.3

$\sqrt{s} = 172$ GeV									
selection	data	total bg.	$q\bar{q}(\gamma)$	$\gamma\gamma$ $\to$ had.	WW	Weν	ZZ	Zee	other bg.	h$\nu\bar{\nu}$ $\varepsilon(\%)$
hadronic	2054	2257 $\pm$ 13	1128	394.8	109.7	3.3	8.8	25.9	587.2	90.5
Mass	1363	1470 $\pm$ 13	660.0	383.5	44.2	3.3	3.5	20.9	355.0	90.5
acoplanarity	805	821 $\pm$ 10	386.8	263.9	41.3	3.0	2.4	8.3	114.8	87.6
no isol. part.	583	546 $\pm$ 8	309.6	205.6	16.3	2.6	1.6	4.5	5.8	82.4
no vis. γ	506	477 $\pm$ 8	259.2	197.5	12.3	2.4	1.2	3.8	0.34	81.2
hermeticity	486	465 $\pm$ 8	251.7	193.7	12.0	2.3	1.1	3.7	0.34	79.5
$\mathcal{W} < 3.3$	0	1.19 $\pm$ 0.12	0.35	0	0.30	0.52	0.02	0	0	47.7
b-tagging	0	0.61 $\pm$ 0.09	0.27	0	0.16	0.16	0.01	0	0	42.8

Table 9: Analysis in the h$\nu\bar{\nu}$ channel: effect of the selections at $\sqrt{s} = 161$ GeV and $\sqrt{s} = 172$ GeV on data, simulated backgrounds and simulated signal events with m_{h} = 60 GeV/c^2 at 161 GeV and m_{h} = 70 GeV/c^2 at 172 GeV. Efficiencies are given for the signal.

m_{h} (GeV/c^2)	Efficiency at 161 GeV (%)	Efficiency at 172 GeV (%)
45	$45.2 \pm 1.1 \; ^{+1.5}_{-1.4}$	$26.9 \pm 1.1 \; ^{+0.8}_{-0.9}$
50	$51.0 \pm 1.1 \; ^{+1.7}_{-1.6}$	$43.4 \pm 1.3 \; ^{+1.4}_{-1.6}$
55	$49.7 \pm 1.1 \; ^{+1.7}_{-1.6}$	$50.6 \pm 1.3 \; ^{+1.7}_{-1.6}$
60	$50.3 \pm 1.1 \; ^{+1.6}_{-1.9}$	$50.5 \pm 1.3 \; ^{+1.6}_{-2.6}$
65	$44.5 \pm 1.1 \; ^{+1.7}_{-1.8}$	$47.4 \pm 1.3 \; ^{+1.9}_{-1.9}$
70	$36.3 \pm 1.1 \; ^{+1.7}_{-1.7}$	$42.8 \pm 1.3 \; ^{+1.8}_{-1.5}$
75	-	$37.5 \pm 1.2 \; ^{+1.5}_{-1.6}$
80	-	$26.4 \pm 1.1 \; ^{+1.5}_{-1.5}$

Table 10: Efficiency of the Higgs boson selection in the h$\nu\bar{\nu}$ channel at $\sqrt{s} = 161$ GeV and $\sqrt{s} = 172$ GeV as a function of the particle mass. The first uncertainty quoted is statistical, the second is systematic.

$\mathcal{W}$ distribution	161 GeV		172 GeV	
Gaussian fit	mean	σ	mean	σ
data	5.97 ± 0.04	0.99 ± 0.03	5.97 ± 0.04	0.93 ± 0.03
simulation	6.02 ± 0.02	0.96 ± 0.01	6.02 ± 0.02	0.95 ± 0.01
$\mathcal{W} < 3.3$	$1.16 \pm 0.14 \pm 0.18$		$0.97 \pm 0.12 \pm 0.13$	

Table 11: $h\nu\bar{\nu}$ channel: the first two lines give the mean and variance of a Gaussian fit to the $\mathcal{W}$ distributions in data and background simulation. The last line shows the expected background computed from the Gaussian parameters in simulation.

parameters from simulation and the number of simulated events after preselection. The result is given in Table 11. The first uncertainty is statistical and obtained by varying successively the mean and variance within the errors given by the Gaussian fit and adding the variations in quadrature. The second uncertainty is obtained by varying successively the mean and variance within half of the differences in the Gaussian parameters between data and simulation, and adding the variations in quadrature. This accounts for systematic uncertainties due to possible imperfections in the simulation.

The computed background in Table 11 is to be compared with the background estimate obtained in Table 9 by direct application of the selection on $\mathcal{W}$ in the simulation. At 172 GeV, the agreement is correct within statistics. At 161 GeV, the computed background is higher indicating a possible underestimate of the background in Table 9. At this energy, a more reliable estimate is obtained by averaging the direct and computed backgrounds, and taking the difference from the average as an additional statistical uncertainty. The final background after b-tagging is obtained by applying the b-tagging rejection factor deduced from Table 9. The final background is thus $0.65 \pm 0.16 \ (stat.) \pm 0.11 \ (syst.)$ events at 161 GeV and $0.61 \pm 0.09 \ (stat.) \pm 0.08 \ (syst.)$ events at 172 GeV. The systematic uncertainty is obtained by applying the relative systematic error on the computed background in Table 11 and adding in quadrature a relative error of $\pm 3\%$ to account for possible differences between data and simulation in b-tagging performance, as measured at the Z boson resonance [17]. Finally, to estimate the systematic uncertainty in the signal efficiencies, the variations in the Gaussian parameters used to derive the systematics on the computed background have been first translated into new selections on $\mathcal{W}$ and the new selections have been applied to the signal simulations. As for the background, a relative error of $\pm 3\%$ has been added in quadrature to account for systematics in b-tagging.

One event is selected in the 161 GeV data sample with $\mathcal{W}$ equal to 3.04. As a comparison, the average values of $\mathcal{W}$ in simulated background events are 6.1 for the $q\bar{q}(\gamma)$ process, 5.9 for WW pairs and 4.4 for Weν events, the r.m.s values being close to 1. Simulated signal events with $m_h = 65 \ \mathrm{GeV}/c^2$ give an average of 3.1 with a r.m.s of 0.9. The values of the individual variables used in $\mathcal{W}$ are summarized in Table 12, which also gives the corresponding probabilities. In most variables (except λ_{xy} and σ_{P_t}), the event is hardly compatible with the background.

The event has a visible mass of 56.2 GeV/c^2 and a missing mass of 100.6 GeV/c^2. As the resolution in the visible mass is rather poor, around 7.5 GeV/c^2, a rescaling is applied to the energy and momentum of the visible system assuming that the recoil system has a mass equal to m_Z [24]. After rescaling, the reconstructed h mass is 64.6 GeV/c^2. Figure 7 shows the distribution of the reconstructed mass in simulated background events at the

variable	P_t	λ_{xy}	α	E_{cone}^{min}	θ_{thr}	σ_{P_t}
	(GeV/c)	(o)	(o)	(GeV)	(o)	(GeV/c)
value	17.5	7.6	36.7	8.5	65.2	0.87
probability	0.11	0.80	0.19	0.35	0.14	0.71

variable	M_{rec}	E_{most}	ρ_{xy}	M	$-\log_{10}(P_E^+)$	$\sqrt{s'}$
	(GeV/c^2)	(GeV)	(o)	(GeV)		(GeV)
value	100.6	7.1	35.6	56.2	7.3	110.7
probability	0.01	0.04	0.08	0.36	0.03	0.21

Table 12: h$\nu\bar{\nu}$ channel: for each variable in the definition of $\mathcal{W}$, the table gives the value measured in the selected event and the corresponding probability to observe such a value in background.

end of the analysis. The mass of the selected event is indicated by the arrow. The resolution achieved in the reconstructed mass is illustrated in Figure 7 for simulated signal events of 60, 65 and 70 GeV/c^2 masses. Close to the kinematic limit, the Z is produced at lower masses than m_Z and the distribution of the reconstructed Higgs boson mass gets distorted, as can be seen for the 70 GeV/c^2 Higgs boson. A reconstructed mass of 64.6 GeV/c^2 can therefore arise from a 70 GeV/c^2 Higgs boson. More precisely, while 52% of 65 GeV/c^2 Higgs bosons give a reconstructed mass equal to the observed one within 2 GeV/c^2, this fraction is 15% and 32% for 60 and 70 GeV/c^2 Higgs bosons, respectively. The uncertainty on the observed reconstructed mass is then estimated as the interval of masses for which this fraction is above 32%, which goes from 62 to 70 GeV/c^2.

Finally, the b content of the event has been thoroughly checked. The b-tagging variable P_E^+ has a value of 4.6×10^{-8}, which corresponds to a purity in beauty quarks of 97% as measured in hadronic Z decays taken at the resonance peak. Four tracks are found to make a secondary vertex in space corresponding to a decay length of 3.28 ± 0.12 mm. The three projections of the vertex are shown in Figure 8. The χ^2 probability of the secondary vertex fit is 0.97. When all tracks in the secondary vertex are given the pion mass, the estimated mass of the system of the four particles is 3.7 GeV/c^2.

3.5   The h $\rightarrow$ invisible, Z $\rightarrow$ q$\bar{\text{q}}$ channel

Minor changes in the previous analysis allow a search for the h $\rightarrow$ invisible, Z $\rightarrow$ q$\bar{\text{q}}$ channel with an acceptable efficiency and background. Starting with the same preselection, the variables in the definition of the event global weight are the same except for the event transverse size, σ_{P_t}, which is replaced by the event thrust, which proves to discriminate signal events better from the background. The selection on the global event weight is chosen as $\mathcal{W}$ < 3.45 to have about 20% efficiency at the reference mass at both energies. The Higgs boson mass is estimated as the missing mass recoiling against the visible system, after a rescaling of the energy and momentum of the latter under the assumption that the visible mass is equal to m_Z. The remaining background is further suppressed by requiring the rescaling to lead to a positive missing mass squared.

Table 13 summarizes the effects of the selections on data and simulation. No event is left in the 161 GeV data sample. One event is selected at 172 GeV with a visible mass of
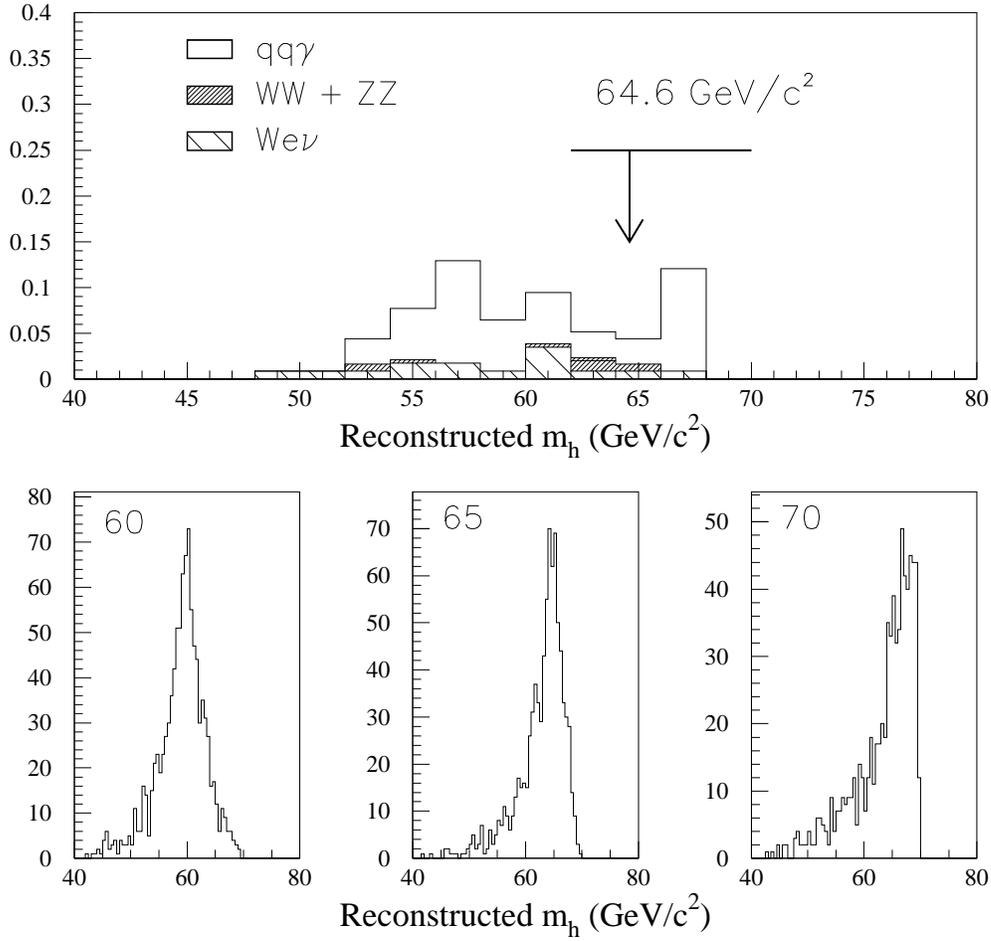
Figure 7: h$\nu\bar{\nu}$ channel: distribution of the reconstructed mass of the Higgs boson at the end of the analysis at $\sqrt{s} = 161$ GeV. The Higgs boson is assumed to recoil against an on-shell Z. The upper plot shows the distribution of the simulated background. The arrow indicates the mass of the selected event and the transverse error bar the uncertainty on the measurement. The bottom plots are the distributions of simulated signal events with masses of 60, 65 and 70 GeV/c^2.

X - Y projection

2.0 mm

Z - X projection
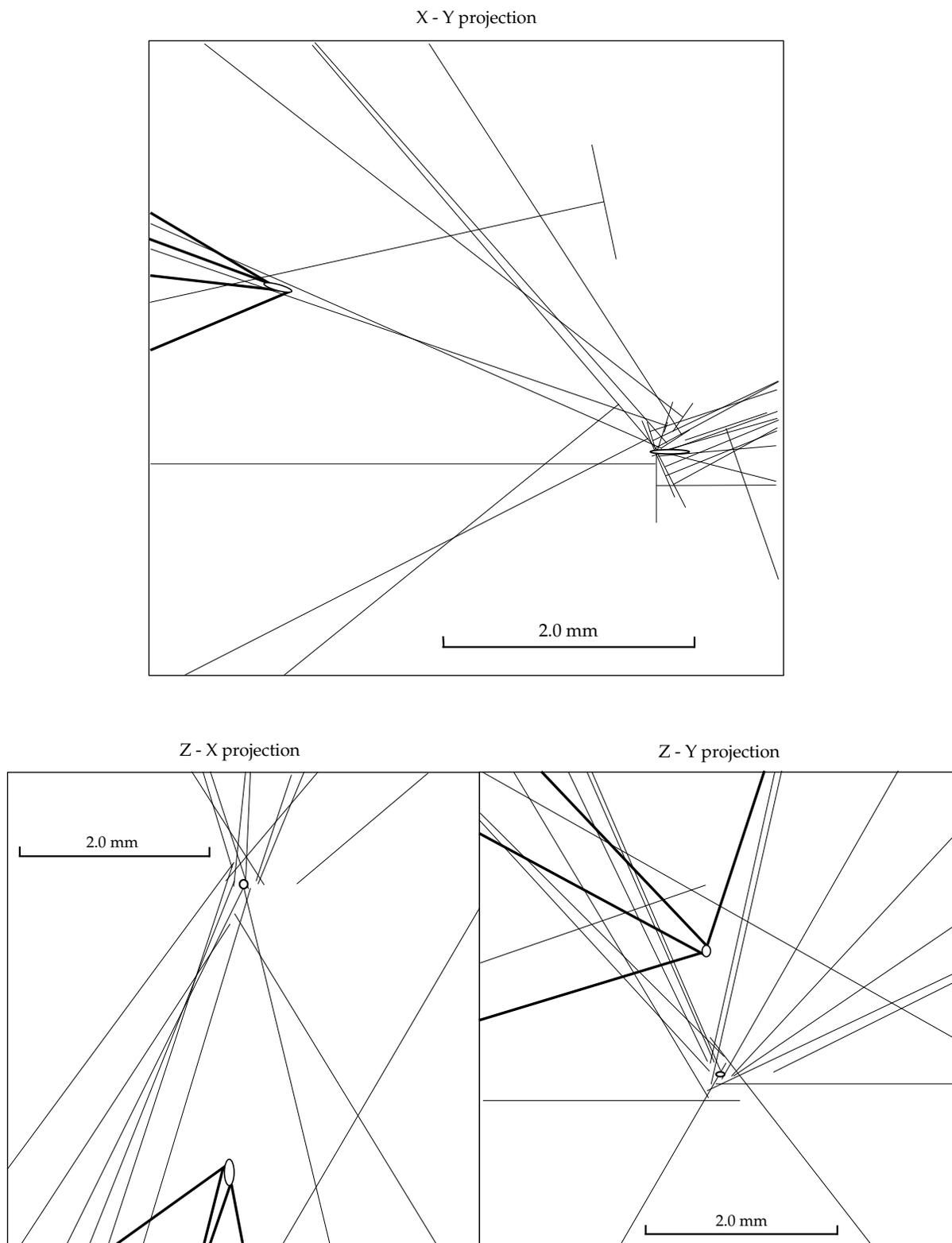
2.0 mm

Z - Y projection

2.0 mm

Figure 8: $h\nu\bar{\nu}$ channel, probabilistic analysis: graphic reconstruction of the secondary vertex found in the selected event. The errors on impact parameters are shown in the x-y projection as transverse bars. The four tracks which are consistent with a secondary vertex in the three projections are indicated by broader lines.

$\sqrt{s}$ = 161 GeV									
selection	data	total bg.	$q\bar{q}(\gamma)$	$\gamma\gamma$ → had.	WW	Weν	ZZ	Zee	other bg.	inv.q$\bar{q}$ ε(%)
presel.	522	504 ± 9	318.7	175.0	4.2	1.8	0.45	3.6	0.55	76.1
$\mathcal{W}$ < 3.45	0	0.83± 0.11	0.42	0	0.11	0.27	0.02	0	0	20.6
mis. mass	0	0.78 ± 0.11	0.42	0	0.11	0.24	0.006	0	0	20.2

$\sqrt{s}$ = 172 GeV									
selection	data	total bg.	$q\bar{q}(\gamma)$	$\gamma\gamma$ → had.	WW	Weν	ZZ	Zee	other bg.	inv.q$\bar{q}$ ε(%)
presel.	486	465 ± 8	251.7	193.7	12.0	2.3	1.1	3.7	0.34	77.1
$\mathcal{W}$ < 3.45	1	1.80 ± 0.16	0.69	0	0.62	0.46	0.02	0	0	24.3
mis. mass	1	1.68 ± 0.15	0.62	0	0.62	0.43	0.02	0	0	24.1

Table 13: h → invisible, Z → q$\bar{q}$ channel: effect of the selections at $\sqrt{s}$ = 161 GeV and $\sqrt{s}$ = 172 GeV on data, simulated backgrounds and simulated signal events with m_h = 60 GeV/c^2 at 161 GeV and m_h = 70 GeV/c^2 at 172 GeV. Efficiencies are given for the signal.

74.8 GeV/c^2, and missing masses of 79.4 GeV/c^2 before rescaling and 51.8 GeV/c^2 after rescaling. The signal efficiencies are given in Table 14.

m_h (GeV/c^2)	Efficiency at 161 GeV (%)	Efficiency at 172 GeV (%)
45	$14.3 \pm 0.8^{+1.3}_{-2.2}$	$14.2 \pm 0.8^{+1.5}_{-1.0}$
50	$14.1 \pm 0.8^{+2.2}_{-1.5}$	$17.2 \pm 0.8^{+1.3}_{-1.3}$
55	$18.4 \pm 0.9^{+1.6}_{-2.1}$	$18.6 \pm 0.9^{+1.4}_{-1.6}$
60	$20.2 \pm 0.9^{+1.6}_{-2.3}$	$21.5 \pm 0.9^{+2.2}_{-1.5}$
65	$18.1 \pm 0.9^{+2.2}_{-2.0}$	$22.9 \pm 0.9^{+1.7}_{-2.3}$
70	$14.2 \pm 0.8^{+1.6}_{-1.6}$	$24.1 \pm 0.9^{+1.3}_{-1.5}$
75	-	$22.2 \pm 0.9^{+1.9}_{-1.9}$
80	-	$16.9 \pm 0.8^{+1.9}_{-1.9}$

Table 14: Efficiency of the Higgs boson selection in the h → invisible, Z → q$\bar{q}$ channel at $\sqrt{s}$ = 161 GeV and $\sqrt{s}$ = 172 GeV as a function of the particle mass. The first uncertainty quoted is statistical, the second is systematic.

The systematic uncertainties have been estimated as previously, by comparing the $\mathcal{W}$ distributions in data and simulation at preselection level. Both are Gaussian and their parameters are compatible, as shown in Table 15. The means agree with the expected value of 6 but the variances are lower than in the h$\nu\bar{\nu}$ channel, indicating higher correlations between the variables used in $\mathcal{W}$. The computed background agrees within statistics with the direct estimate at 161 GeV, but at 172 GeV the computed background is lower. A better estimate at this energy is obtained by averaging the computed and direct estimates and the difference from the average is taken as an additional statistical

$\mathcal{W}$ distribution	161 GeV		172 GeV	
Gaussian fit	mean	σ	mean	σ
data	6.02 ± 0.04	0.90 ± 0.03	5.98 ± 0.04	0.88 ± 0.02
simulation	6.01 ± 0.01	0.85 ± 0.01	6.02 ± 0.02	0.92 ± 0.01
$\mathcal{W} < 3.45$	$0.65 \pm 0.09^{+0.21}_{-0.17}$		$1.21 \pm 0.14^{+0.25}_{-0.23}$	

Table 15: h $\rightarrow$ invisible, Z $\rightarrow$ q$\bar{\text{q}}$ channel: the first two lines give the mean and variance of a Gaussian fit to the $\mathcal{W}$ distributions in data and background simulation. The last line shows the expected background computed from the Gaussian parameters in simulation.

uncertainty. The final expected background is thus 0.78 ± 0.11 (*stat.*) ± 0.25 (*syst.*) events at 161 GeV and 1.40 ± 0.32 (*stat.*) ± 0.29 (*syst.*) events at 172 GeV. No contribution has been added to the systematics for the last selection on the reconstructed mass, since differences between data and simulation in this variable are such that moving the selection accordingly has no effect, either in the background expectation or in the signal efficiencies.

4 Neutral Higgs boson searches in events with jets and taus

This topology makes 8.5% of the hZ final states and 14.4% of the hA final states. The experimental signature is two jets and two isolated τ leptons, which are reconstructed inclusively as low multiplicity jets.

4.1 Preselection

Hadronic events are selected by requiring at least seven charged particles, a total energy greater than $0.30\sqrt{s}$ and a total energy carried by charged particles greater than $0.15\sqrt{s}$. As τ leptons are expected to give low multiplicity jets with one or three charged particles, a four-jet topology is forced using the Durham algorithm [18], and jets are classified by increasing multiplicity. The two jets with lowest charged multiplicities are identified as τ candidates, and the invariant mass of the $\tau^+\tau^-$ pair is required to be greater than 20 GeV/c^2 since the search is restricted to heavy Higgs bosons.

Events with a large missing energy (such as q$\bar{\text{q}}(\gamma)$ events with an energetic photon lost in the beam pipe) are rejected by requiring the effective centre-of-mass energy $\sqrt{s'}$ to be greater than 105 GeV. The dominant background then comes from q$\bar{\text{q}}(\gamma)$ events leading to two jets in a back-to-back topology or to three jets. To reduce this contamination, a linear discriminant analysis is performed using the Fisher method [25]. This method discriminates between two classes of events using the same set of variables which are linearly combined into a single discriminating variable. The linear combination of the selected variables is chosen such that the ratio of the between-class variance (i.e. the variance of the distribution of the final discriminating variable in the two samples taken together) to the within-class variance (i.e. the variance of the distribution in the signal sample) is maximized. The distributions used to define the discriminating variable are obtained with a sample of 1000 simulated signal events and a sample of 1000 q$\bar{\text{q}}(\gamma)$ simulated background events, both samples being taken after the preceding selections.

To check the stability of the result, the definition procedure is repeated six times at each centre-of-mass energy, with two different signal samples, and three different samples of $q\bar{q}(\gamma)$ background events. The definition of the discriminating function is found to be very stable and not to change with the energy. The variables are, in order of decreasing discriminating power:

- Y_{min}, the minimal distance [18] between two jets,
- C, a combination of the normalised sphericity tensor eigenvalues [26],

$$C = 3(\lambda_1\lambda_2 + \lambda_1\lambda_3 + \lambda_2\lambda_3)$$

- T, the event thrust,
- θ_{min}, the minimum opening angle between any pair of jets.

The T and C variables help to remove two-jet events, while Y_{min} and θ_{min} identify three-jet like events. The most discriminating combination of these variables as given by the Fisher method is:

$$Dvar = -6.951 - 0.979 \cdot Y_{min} + 4.562 \cdot C + 8.253 \cdot T + 0.015 \cdot \theta_{min}$$

This variable is required to be positive, which selects about 75% of the signal and reduces the expected background by a factor 4 when averaging both energies.

$\sqrt{s} = 161$ GeV									
selection	data	total	$q\bar{q}(\gamma)$	WW	ZZ	Zee	Weν	$\gamma\gamma$	hZ
		bg.						$\rightarrow$ had.	$\varepsilon(\%)$
hadronic	985	880.2 ± 7.7	746.3	22.4	2.4	6.7	1.4	91.2	89.7 (92.6)
$\sqrt{s'} > 105$	442	381.8 ± 5.2	318.5	19.7	2.1	2.4	0.51	29.2	81.6 (78.4)
$Dvar > 0$	91	83.6 ± 2.1	64.6	14.1	1.3	0.83	0.1	2.6	62.3 (60.1)
τ charges	39	32.0 ± 1.4	24.0	5.1	0.63	0.37	0.03	1.77	42.3 (41.4)
τ mult.	13	9.7 ± 1.1	6.2	1.1	0.40	0.23	0.01	1.77	30.9 (29.6)
isolation	3	3.23 ± 0.7	1.57	0.37	0.28	0.13	0	0.88	26.5 (26.2)
$\sqrt{s} = 172$ GeV									
selection	data	total	$q\bar{q}(\gamma)$	WW	ZZ	Zee	Weν	$\gamma\gamma$	hZ
		bg.						$\rightarrow$ had.	$\varepsilon(\%)$
hadronic	896	795 ± 5.6	609.3	82.2	6.2	12.5	1.7	72.3	88.2 (91.2)
$\sqrt{s'} > 105$	439	378 ± 3.8	267.4	73.1	5.0	3.7	0.87	27.6	80.3 (79.1)
$Dvar > 0$	130	103 ± 1.2	49.0	49.5	2.3	1.2	0.13	0.95	65.2 (58.1)
τ charges	40	37.2 ± 0.7	17.3	18.2	1.1	0.60	0.02	0	45.5 (42.7)
τ mult.	12	8.9 ± 0.4	4.1	3.8	0.62	0.37	0.01	0	38.3 (35.6)
isolation	6	3.6 ± 0.2	1.0	1.8	0.44	0.32	0	0	29.2 (28.8)

Table 16: Analysis in the $\tau^+\tau^-q\bar{q}$ channel: effect of the selections at $\sqrt{s} = 161$ GeV and $\sqrt{s} = 172$ GeV on data, simulated backgrounds and simulated signal events with m_h = 60 GeV/c^2 at 161 GeV and m_h = 70 GeV/c^2 at 172 GeV. Efficiencies are given for the signal (τ from h, and in parentheses τ from Z).

In order to increase the purity in true τ leptons, three additional selections are introduced, based on the charge, multiplicity and isolation of the jets tagged as τ candidates. The product of the jet charges [‡] is required to be lower than -0.2 and the sum of their charged multiplicities to be lower than 5. The isolation of the τ candidates is characterized by the global variable:

$$I = \frac{E_{cone}^{(1)} \cdot E_{cone}^{(2)}}{E_{\tau jet}^{(1)} \cdot E_{\tau jet}^{(2)}}$$

where E_{cone}^i is the energy in a cone of $30°$ around each τ candidate, and $E_{\tau jet}^i$ is the τ energy. This variable is required to be between 0.85 and 1.05, which is the preferred interval for signal events.

Table 16 presents the effect of the selections on data, simulated backgrounds and simulated hZ events. The total background in the table also includes the residual contamination from $e^+e^-(\gamma)$ events, which is not indicated separately since it amounts to only around ten events in the first two steps of the analysis and is then suppressed by the discriminant analysis. Data agree with simulation after the discriminant analysis at 161 GeV, and after the next selection on the charges of the τ candidates at 172 GeV. This is illustrated in Figure 9 which compares 172 GeV data with simulated backgrounds and simulated signal events at 70 GeV/c^2. The distributions refer to $\sqrt{s'}$, $Dvar$, the product of the τ jet charges, the sum of the τ charged multiplicities, and the τ isolation variable. The first distribution is shown after the hadronic selection, the others after the selection on $\sqrt{s'}$. The disagreement between data and simulation is partly in the signal region in the distribution of $Dvar$, and hence is not completely suppressed after the selection on $Dvar$, as was the case at 161 GeV. Agreement is however obtained after the next selection.

Before channel dependent selections, a kinematic fit [19] is applied to the preselected events. In addition to total momentum and energy conservation, a hypothetical neutrino is added to each τ jet and the neutrino momenta are adjusted so that the mass of each jet-neutrino system is consistent with the τ mass. The mass resolutions achieved after the kinematic fit are illustrated in Figure 10 which presents the distributions of the invariant masses of the $\tau^+\tau^-$ pair and of the recoiling hadronic system for simulated signal events in the three channels, at 172 GeV. The distribution of one mass as a function of the other is also shown for 161 and 172 GeV data. The fitted jet and τ energies and momenta are used in the final selections described in the three following subsections.

4.2 The hZ channel

4.2.1 h decaying into $\tau^+\tau^-$

In the hZ channel with h decaying into $\tau^+\tau^-$, the hadronic system is expected to come from a Z and the $\tau^+\tau^-$ pair from a high mass Higgs boson. Events are selected if the mass of the $\tau^+\tau^-$ pair is greater than 45 GeV/c^2 and the mass of the pair of hadronic jets is above 70 GeV/c^2.

The effect of the selections on data, simulated backgrounds and simulated signal events is shown in Table 17, while the signal efficiencies are given in Table 18. The final expected

---

[‡]the jet charge is defined as

$$Q_{jet} = \sum_{i \in jetj} q_i \omega^{0.2}, \quad \text{where} \quad \omega = \frac{\vec{P}_i . \vec{P}_{jetj}}{|\vec{P}_{jetj}|^2} \quad \text{always positive in the Durham clustering}$$
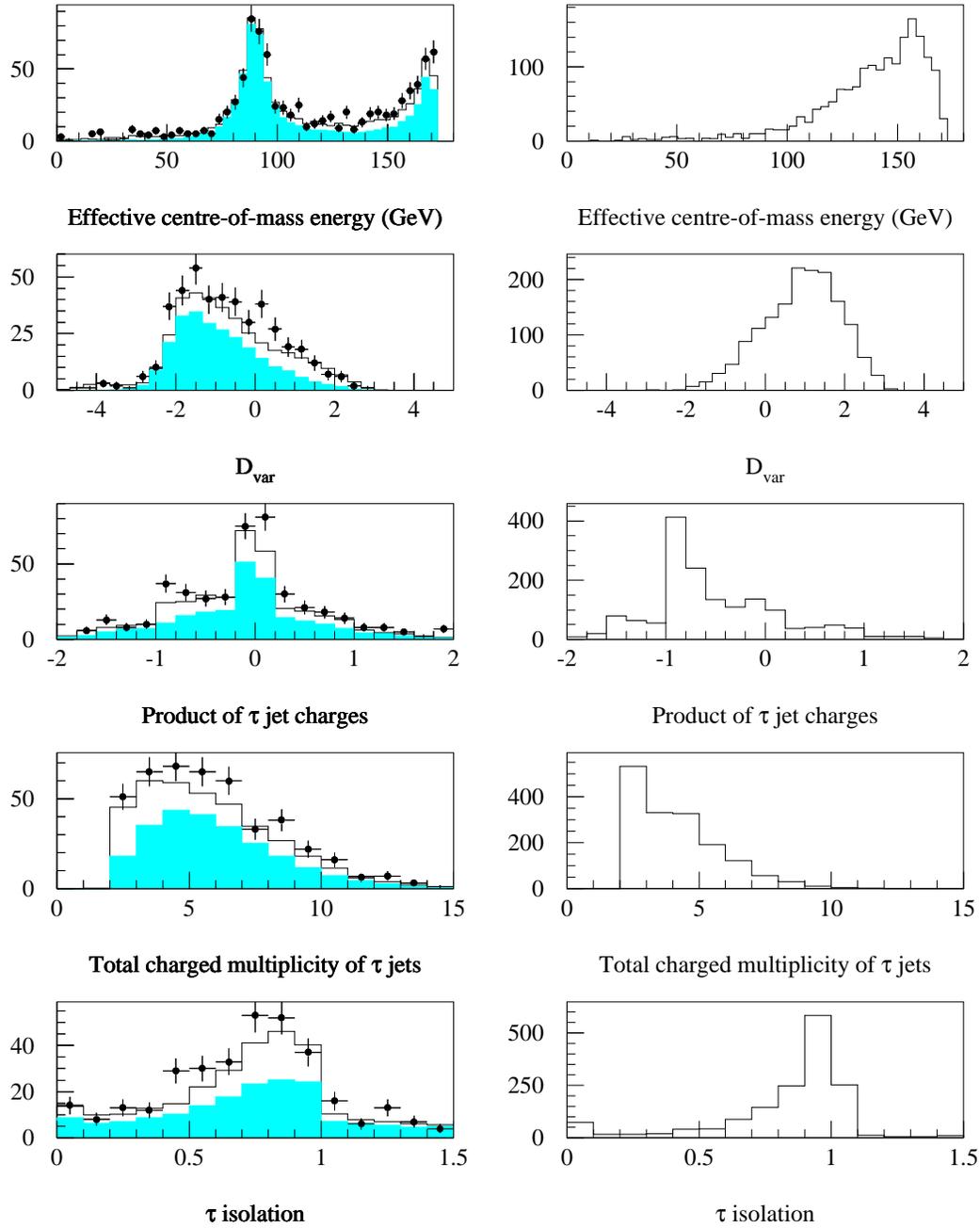
DELPHI - √s = 172 GeV

Figure 9: $\tau^+\tau^-$ $q\bar{q}$ channel: distributions of some analysis variables as described in the text. Plots on the left show a comparison between 172 GeV data and simulated background events (solid line) normalised to the experimental luminosity. The shaded area represents the contribution of the dominant $q\bar{q}(\gamma)$ background. Plots on the right show the (unnormalised) expected distributions for a 70 GeV/c^2 Higgs boson decaying into $\tau^+\tau^-$.

DELPHI - √s = 161+172 GeV
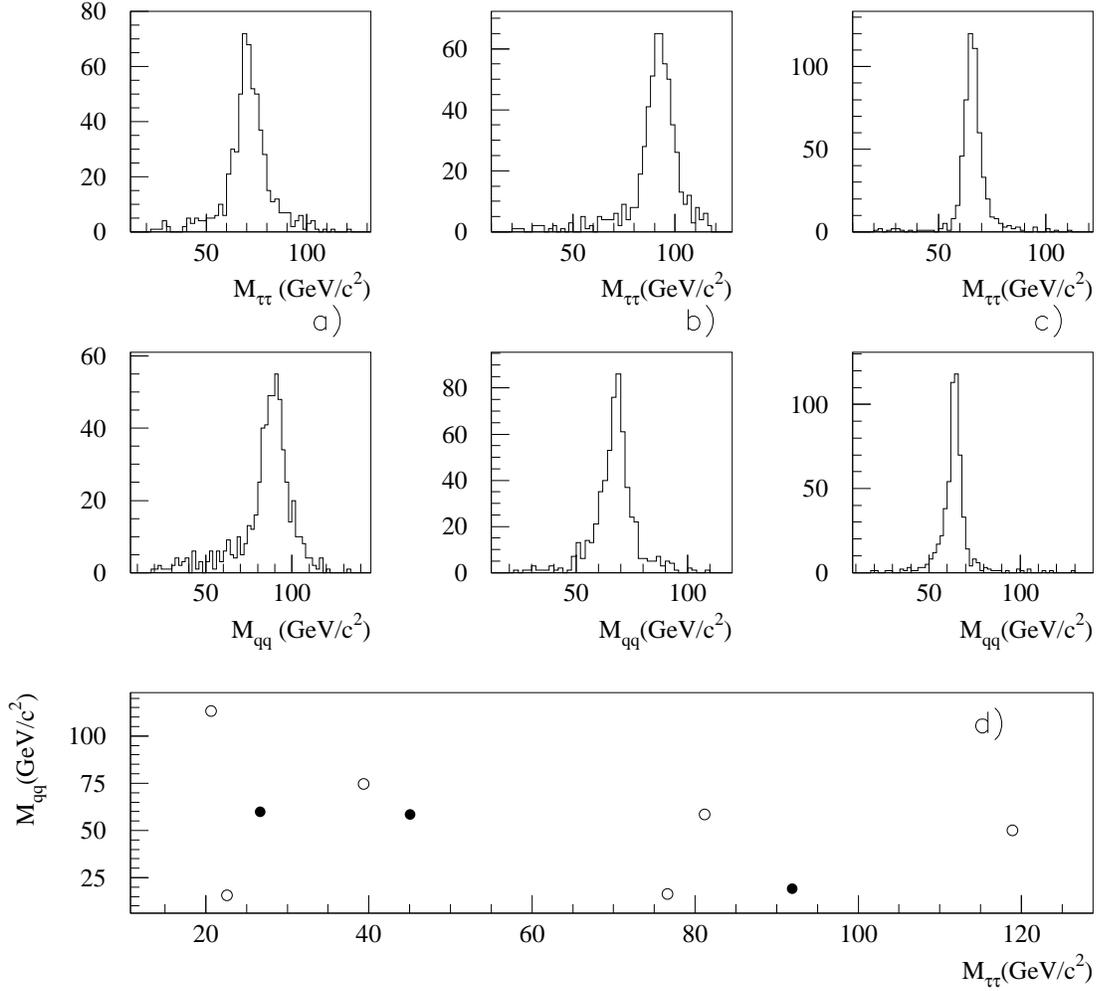
Figure 10: $\tau^+\tau^-$ $q\bar{q}$ channel: invariant mass distributions of the $\tau^+\tau^-$ pair and of the pair of hadronic jets after preselection. Plots a), b) and c) refer to simulated signal samples at $\sqrt{s} = 172$ GeV with a Higgs boson mass of 70 GeV/c^2 in the $(h \rightarrow \tau^+\tau^-)q\bar{q}$, $(h \rightarrow q\bar{q})\tau^+\tau^-$ and $hA \rightarrow \tau^+\tau^- q\bar{q}$ channels, respectively. Plot d) shows data at 161 GeV (black circles) and 172 GeV (open circles) in the plane 'invariant mass of the pair of hadronic jets' vs 'invariant mass of the $\tau^+\tau^-$ pair'.

$\sqrt{s} = 161$ GeV								
Selection	data	total bg.	$q\bar{q}(\gamma)$	WW	ZZ	Zee	$\gamma\gamma$	hZ (ε%)
$m_{\tau\tau} > 45 \text{GeV}/c^2$	2	2.1 ± 0.5	1.15	0.19	0.14	0.10	0.44	25.8
$m_{q\bar{q}} > 70 \text{GeV}/c^2$	0	0.32 ± 0.09	0.14	0.08	0.08	0.03	0	24.0
$\sqrt{s} = 172$ GeV								
Selection	data	total bg.	$q\bar{q}(\gamma)$	WW	ZZ	Zee	$\gamma\gamma$	hZ (ε%)
$m_{\tau\tau} > 45 \text{GeV}/c^2$	3	2.45 ± 0.17	0.74	1.24	0.25	0.20	0	28.1
$m_{q\bar{q}} > 70 \text{GeV}/c^2$	0	0.91 ± 0.11	0.18	0.41	0.15	0.17	0	24.4

Table 17: Analysis in the (h $\rightarrow$ $\tau^+\tau^-$)q$\bar{q}$ channel: effect of the final selections at $\sqrt{s} = 161$ GeV and $\sqrt{s} = 172$ GeV on data, simulated backgrounds and simulated (h $\rightarrow$ $\tau^+\tau^-$)q$\bar{q}$ events with $m_h = 60$ GeV/c^2 at 161 GeV and $m_h = 70$ GeV/c^2 at 172 GeV.

background is 0.32 ± 0.09 (*stat.*) ± 0.03 (*syst.*) events at 161 GeV, mostly due to the q$\bar{q}(\gamma)$ process, and 0.91 ± 0.11 (*stat.*) ± 0.09 (*syst.*) events at 172 GeV, mostly from WW pairs. No event is selected in the data. Systematic uncertainties have been derived in the following way. Track momenta were randomly varied according to the experimental resolutions while energies were randomly varied by $\pm 3\%$. The analysis variables were recalculated and the shifts in the signal efficiencies and background estimates taken as systematic uncertainties. The same method is used in the two other channels.

m_h (GeV/c^2)	Efficiency at 161 GeV (%)	Efficiency at 172 GeV (%)
45	$10.4 \pm 0.7 \pm 1.9$	$12.2 \pm 0.7 \pm 2.2$
50	$21.2 \pm 0.9 \pm 1.9$	$17.3 \pm 0.8 \pm 2.0$
55	$23.5 \pm 0.9 \pm 1.9$	$20.8 \pm 0.9 \pm 2.0$
60	$24.0 \pm 0.9 \pm 1.9$	$23.7 \pm 0.9 \pm 1.9$
65	$23.8 \pm 0.9 \pm 1.9$	$22.9 \pm 0.9 \pm 1.9$
70	$22.1 \pm 0.9 \pm 1.9$	$24.4 \pm 0.9 \pm 1.9$
75	-	$25.3 \pm 0.9 \pm 1.9$
80	-	$24.1 \pm 0.9 \pm 1.9$

Table 18: Efficiency of the Higgs boson selection in the (h $\rightarrow$ $\tau^+\tau^-$)q$\bar{q}$ channel at $\sqrt{s} = 161$ GeV and $\sqrt{s} = 172$ GeV, as a function of the Higgs boson mass. The first uncertainty quoted is statistical, the second is systematic.

4.2.2 Z decaying into $\tau^+\tau^-$

When the Z decays into $\tau^+\tau^-$, the hadronic system is expected to come from the Higgs boson and thus to contain beauty hadrons. Events are selected if the mass of the pair of hadronic jets is greater than 35 GeV/c^2 and the mass of the $\tau^+\tau^-$ pair is greater than 70 GeV/c^2. The b-tagging variable, P_E^+, is required to be below 0.1, which reduces the remaining background by a factor of 3 to 4 for a limited loss in efficiency.

$\sqrt{s} = 161$ GeV								
Selection	data	total bg.	$q\bar{q}(\gamma)$	WW	ZZ	Zee	$\gamma\gamma$	hZ ($\varepsilon\%$)
$m_{\tau\tau} > 70\text{GeV}/c^2$	1	1.4 ± 0.5	0.78	0.08	0.05	0.05	0.44	25.3
$m_{q\bar{q}} > 35\text{GeV}/c^2$	0	1.3 ± 0.5	0.74	0.06	0.02	0.04	0.44	24.5
$P_E^+ < 0.1$	0	0.31 ± 0.1	0.23	0.03	0.01	0.03	0	23.9
$\sqrt{s} = 172$ GeV								
Selection	data	total bg.	$q\bar{q}(\gamma)$	WW	ZZ	Zee	$\gamma\gamma$	hZ ($\varepsilon\%$)
$m_{\tau\tau} > 70\text{GeV}/c^2$	3	1.2 ± 0.12	0.44	0.59	0.12	0.04	0	26.7
$m_{q\bar{q}} > 35\text{GeV}/c^2$	2	0.90 ± 0.11	0.38	0.39	0.10	0.04	0	26.4
$P_E^+ < 0.1$	0	0.22 ± 0.06	0.10	0.09	0.01	0.02	0	24.4

Table 19: Analysis in the $(h \to q\bar{q})\tau^+\tau^-$ channel: effect of the final selections at $\sqrt{s} = 161$ GeV and $\sqrt{s} = 172$ GeV on data, simulated backgrounds and simulated $(h \to q\bar{q})\tau^+\tau^-$ events with $m_h = 60$ GeV/c^2 at 161 GeV and $m_h = 70$ GeV/c^2 at 172 GeV.

The result of these selections on data, simulated backgrounds, and simulated signal events is given in Table 19, while the efficiencies are given in Table 20. The final expected background amounts to 0.31 ± 0.10 (*stat.*) ± 0.03 (*syst.*) events at 161 GeV and to 0.22 ± 0.06 (*stat.*) ± 0.04 (*syst.*) events at 172 GeV. In both cases, $q\bar{q}(\gamma)$ events are the main source of background. No event is left in the data.

m_h (GeV/c^2)	Efficiency at 161 GeV (%)	Efficiency at 172 GeV (%)
45	$14.9 \pm 1.3 \pm 1.9$	$18.4 \pm 1.2 \pm 2.1$
50	$20.1 \pm 0.9 \pm 2.3$	$17.7 \pm 0.7 \pm 2.1$
55	$21.4 \pm 0.9 \pm 2.3$	$18.6 \pm 0.7 \pm 2.1$
60	$23.9 \pm 0.9 \pm 2.3$	$21.6 \pm 1.1 \pm 2.2$
65	$24.3 \pm 0.9 \pm 2.3$	$22.2 \pm 0.9 \pm 2.2$
70	$22.9 \pm 0.9 \pm 2.3$	$24.4 \pm 0.9 \pm 2.2$
75	-	$25.1 \pm 1.1 \pm 2.2$
80	-	$24.4 \pm 0.9 \pm 2.2$

Table 20: Efficiency of the Higgs boson selection in the $(h \to q\bar{q})\tau^+\tau^-$ channel at $\sqrt{s} = 161$ GeV and $\sqrt{s} = 172$ GeV, as a function of the Higgs boson mass. The first uncertainty quoted is statistical, the second is systematic.

4.3 The hA channel

In the hA channel, the cross-section is maximum at large $\tan\beta$, i.e. when the two Higgs bosons are almost degenerate in mass. In that case, the masses of the pair of hadronic jets and of the $\tau^+\tau^-$ pair are expected to be close. In addition, one Higgs boson is expected to decay into a b$\bar{\text{b}}$ pair. Events are selected if the mass of the $\tau^+\tau^-$ pair is greater than 30 GeV/c^2 and the absolute value of the difference between the invariant

masses is below 20 GeV/c^2. The b-tagging variable, P_E^+ , is required to be below 0.1, as previously.

$\sqrt{s}$ = 161 GeV								
Selection	data	total bg.	q$\bar{\text{q}}(\gamma)$	WW	ZZ	Zee	$\gamma\gamma$	hA (ε%)
$m_{\tau\tau} > 30$GeV/c^2	2	2.51 ± 0.5	1.43	0.31	0.21	0.11	0.44	24.8
$\Delta m < 20$GeV/c^2	0	0.82 ± 0.28	0.60	0.15	0.03	0.04	0	22.1
$P_E^+ < 0.1$	0	0.20 ± 0.08	0.14	0.04	0.01	0.01	0	20.0
$\sqrt{s}$ = 172 GeV								
Selection	data	total bg.	q$\bar{\text{q}}(\gamma)$	WW	ZZ	Zee	$\gamma\gamma$	hA (ε%)
$m_{\tau\tau} > 30$GeV/c^2	4	3.34 ± 0.20	1.03	1.64	0.35	0.31	0	27.8
$\Delta m < 20$GeV/c^2	0	1.54 ± 0.15	0.75	0.72	0.04	0.13	0	24.8
$P_E^+ < 0.1$	0	0.42 ± 0.08	0.20	0.18	0	0.03	0	22.5

Table 21: Analysis in the hA $\rightarrow$ $\tau^+\tau^-$q$\bar{\text{q}}$ channel: effect of the final selections at $\sqrt{s}$ = 161 GeV and $\sqrt{s}$ = 172 GeV on data, simulated backgrounds and simulated hA $\rightarrow$ $\tau^+\tau^-$q$\bar{\text{q}}$ signal events with m_h = 60 GeV/c^2 at 161 GeV and m_h = 70 GeV/c^2 at 172 GeV.

m_h , m_A (GeV/c^2)	Efficiency at 161 GeV (%)	Efficiency at 172 GeV (%)
45	$22.4 \pm 0.9 \pm 1.8$	$23.8 \pm 0.9 \pm 2.0$
50	$23.7 \pm 0.9 \pm 1.8$	$26.4 \pm 0.9 \pm 2.0$
55	$23.2 \pm 0.9 \pm 1.8$	$23.9 \pm 0.9 \pm 2.0$
60	$20.0 \pm 0.9 \pm 1.8$	$24.9 \pm 0.9 \pm 2.0$
65	$21.8 \pm 0.9 \pm 1.8$	$23.2 \pm 0.9 \pm 2.0$
70	-	$22.5 \pm 0.9 \pm 2.0$

Table 22: Efficiency of the Higgs boson selection in the hA $\rightarrow$ $\tau^+\tau^-$q$\bar{\text{q}}$ channel at $\sqrt{s}$ = 161 GeV and $\sqrt{s}$ = 172 GeV, as a function of the common Higgs boson mass. The first uncertainty quoted is statistical, the second is systematic.

Table 21 presents the effect of the selections on data, simulated backgrounds, and simulated signal events. Table 22 gives the signal efficiencies. At the end of the analysis, no event is selected in the data while the expected background amounts to 0.20 ± 0.08 (*stat.*) ± 0.03 (*syst.*) events, mainly from the q$\bar{\text{q}}(\gamma)$ process, and to 0.42 ± 0.08 (*stat.*) ± 0.03 (*syst.*) events, from both the q$\bar{\text{q}}(\gamma)$ and WW processes.

5 Higgs boson searches in events with four jets

This channel is the dominant topology in both the hZ and hA production modes, with branching fractions around 60% and 85%, respectively. The difficulty arises from the high background from q$\bar{\text{q}}(\gamma)$ and WW events, and from the ambiguity in identifying the jets

which come from the same boson, especially in the hZ channel. After a common four-jet selection, b-tagging and dijet mass reconstruction play a crucial role in both respects.

5.1 Four-jet selection

The selection procedure is the same for all four-jet channels and thus is not optimised for any particular signal. It consists of three steps: a hadronic preselection, a search for a four-jet shape and a final decision after a kinematic fit.

5.1.1 Hadronic preselection

Hadronic events are selected by requiring at least twelve charged particles, a total charged energy above $0.30\sqrt{s}$ and a total energy exceeding $0.40\sqrt{s}$. These selections eliminate almost all $e^+e^-(\gamma)$ and $\gamma\gamma$ events without affecting the signal.

Many of the remaining events are radiative $q\bar{q}(\gamma)$ events, either with a visible initial state radiation photon seen in the luminometer or in the electromagnetic calorimeters, or with an undetected one aligned along the beam axis. In this last case, the missing photon energy is computed from energy and momentum conservation, assuming a photon collinear to the beam axis. Events with a photon (seen or invisible) of more than 35 GeV are rejected.

5.1.2 Four-jet shape

Four-jet events are then selected by demanding three conditions: firstly, the sum of the Fox-Wolfram moments [27] of order two and four has to be less than 1.1 (to eliminate 'cigar-like' events); secondly, the JADE algorithm [28] is applied with a y_{cut} value of 0.004 and the event has to cluster in at least four jets (to eliminate most of the three-jet events); finally, after forcing a four-jet configuration, the product of the energy of the least energetic jet and the minimum opening angle of any pair of jets has to be greater than 6 GeV·rad, thus removing configurations with a soft gluon jet radiated along a hard parton.

5.1.3 Final selection

A four constraint kinematic fit [19] is applied, requiring total energy and momentum conservation, and events are kept if the χ^2 probability of the fit is above 7.3×10^{-3}. Since the signal is characterized by four hadronic jets, the charged multiplicity of each jet is required to be at least 2.

Table 23 summarizes the results of each step of the selection on data and simulated samples of the main background processes. Figure 11 shows a comparison at 161 GeV between data and all simulated backgrounds. Also given are the expected distributions for a hq$\bar{q}$ signal with a 60 GeV/c^2 Higgs boson. The first distribution refers to the effective centre-of-mass energy after the hadronic selection. There is a disagreement between data and simulation which affects the absolute normalisation but the shape of the distribution is correctly reproduced. The three other distributions show the sum of the second and fourth Fox-Wolfram moments, the product of the energy of the least energetic jet and the minimum opening angle of any pair of jets, and the minimal jet charged multiplicity, after the veto against radiative events. Some disagreement between data and simulation remains at this level, but only in regions where no signal is expected. This explains why, after the requirement of a four-jet configuration, the 161 GeV data and simulation are
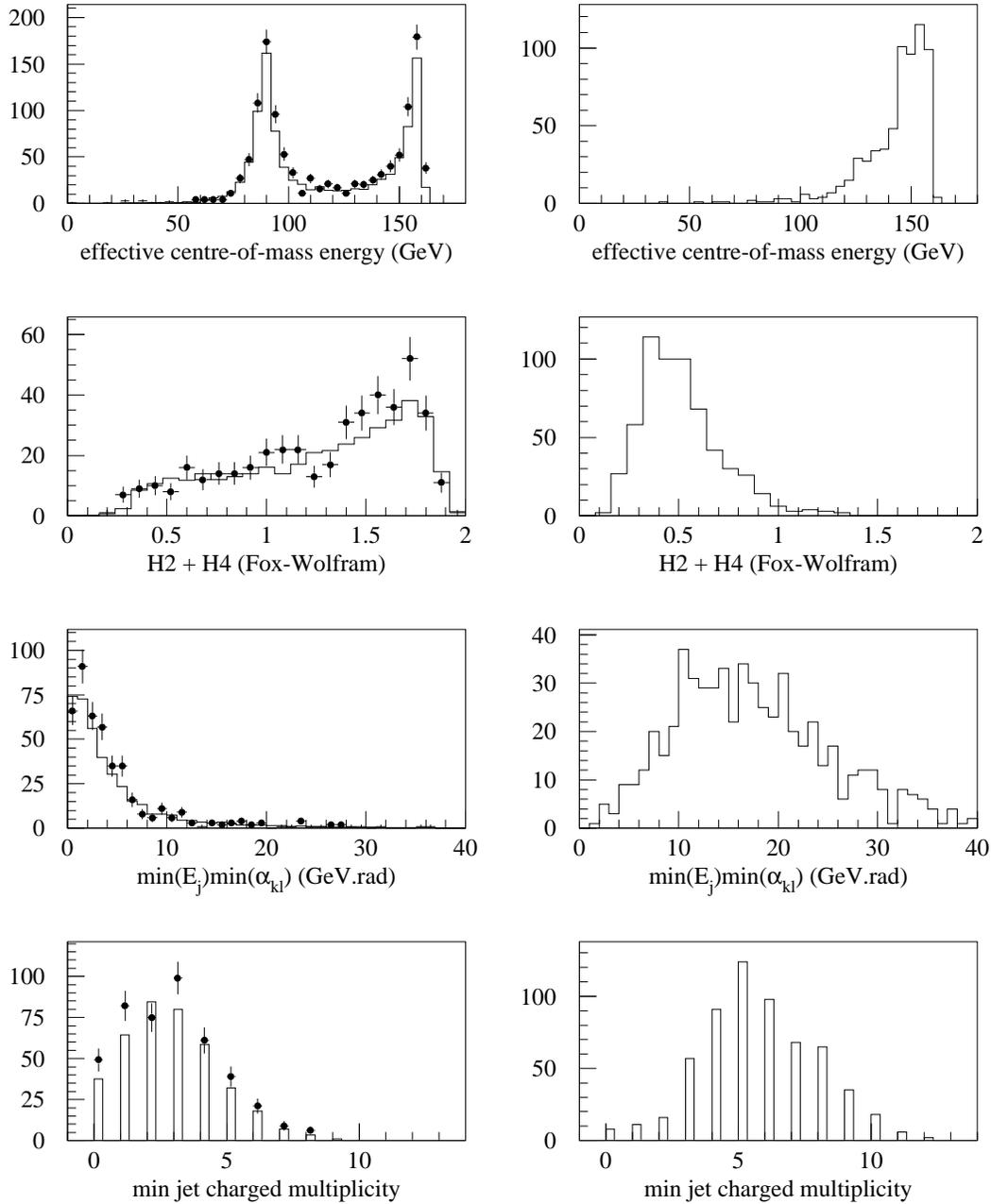
DELPHI - √s = 161 GeV

Figure 11: Four-jet channels: distributions of some analysis variables as described in the text. Plots on the left show a comparison between 161 GeV data and simulated background events (solid line) normalised to the experimental luminosity. Plots on the right show the (unnormalised) expected distributions for the $h q \bar{q}$ process with $m_h = 60$ GeV/c^2.

$\sqrt{s} = 161$ GeV							
selection	data	total bg.	$q\bar{q}(\gamma)$	WW	ZZ	other bg.	$hq\bar{q}$ $\varepsilon(\%)$
hadronic selection	1192	1055 ± 13	999	27	2.7	26	98.1
had. non rad. events	441	393 ± 6	369	20	2.2	2	87.6
4-jet configuration	70	68 ± 2	52	15	1.6	0	82.0
kin. constraints	57	62 ± 2	47	13	1.5	0	80.3
jet multiplicities	50	57 ± 2	43	13	1.0	0	77.1
$\sqrt{s} = 172$ GeV							
selection	data	total bg.	$q\bar{q}(\gamma)$	WW	ZZ	other bg.	$hq\bar{q}$ $\varepsilon(\%)$
hadronic selection	984	910 ± 11	788	98	7	18	98.8
had. non rad. events	366	355 ± 4	285	63	4	3	86.7
4-jet configuration	101	95 ± 2	42	51	2	0	81.8
kin. constraints	88	88.0 ± 1.5	39	47	2	0	79.9
jet multiplicities	82	83.0 ± 1.3	36	45	2	0	78.0

Table 23: Selection of four-jet events: effect of the selections at $\sqrt{s} = 161$ GeV and $\sqrt{s} = 172$ GeV on data, simulated backgrounds and simulated $hq\bar{q}$ signal events with m_h = 60 GeV/c^2 at 161 GeV and m_h = 70 GeV/c^2 at 172 GeV. Efficiencies are given for the signal.

in agreement, as can be seen in Table 23. At 172 GeV, the agreement between data and simulation is reached, both in shape and absolute normalisation, at the earlier stage of the veto against radiative events.

The common four-jet selection is the starting point of the searches for neutral Higgs bosons in the hZ and hA modes, described in the following subsection, and the preselection of the searches for charged Higgs bosons in the purely hadronic mode, described in Section 6.3. The systematic uncertainties in all four-jet analyses are also derived at this level. Apart from small uncertainties on the luminosity measurement and cross-section estimates (globally estimated to less than 0.7% relative), the main systematics comes from the observed differences between data and simulation at two levels: the hadronic selection and the four-jet selection. As already noted, there is a big difference at the hadronic selection level (especially at 161 GeV where the disagreement is around 13%), but this is not due to four-jet events since a good agreement is observed for both energies after the four-jet selection. The evolution of the data to simulation ratio after the four-jet selection has been studied by varying each selection criterion by 4 times the experimental resolution on the corresponding variable. Simulation samples using a different hadronization and fragmentation scheme (ARIADNE [29] instead of JETSET [11]) have also been used to check the modelling of these effects. The best agreement is obtained with ARIADNE and a selection in the Fox-Wolfram moments at 1.1. From this study, the systematic uncertainty at the four-jet selection level is estimated to 2.5% (relative) by taking the quadratic sum of all contributions. Such a study, done at the four-jet selection level, does not explain the difference at the hadronic selection level. This difference

is attributed to an imperfect modelling of the $q\bar{q}(\gamma)$ background only and leads to an additional relative systematic uncertainty of 8% on the fraction of the background estimate due to the $q\bar{q}(\gamma)$ process. Thus, the total systematic uncertainties are $\pm 7.0\%$ at 161 GeV and $\pm 5.1\%$ at 172 GeV on the expected background, and $\pm 2.6\%$ on the signal efficiencies at both energies, whatever the Higgs boson masses. When b-tagging is used in the analysis, an additional relative error of $\pm 3\%$ is added quadratically.

5.2   Search for neutral Higgs bosons

5.2.1   Tight four-jet selection

To reduce the $q\bar{q}(\gamma)$ background further, two of the previous criteria are tightened. The sum of the Fox-Wolfram moments is required to be below 0.9 instead of 1.1, and the selection on the product of the energy of the least energetic jet and the minimum opening angle of any pair of jets is set at 10 GeV·rad instead of 6 GeV·rad. Figure 12 shows the distribution, at this stage of the analysis, of the sum of the dijet masses given by the kinematic fit. The rise of the WW contribution at 172 GeV is clearly seen.
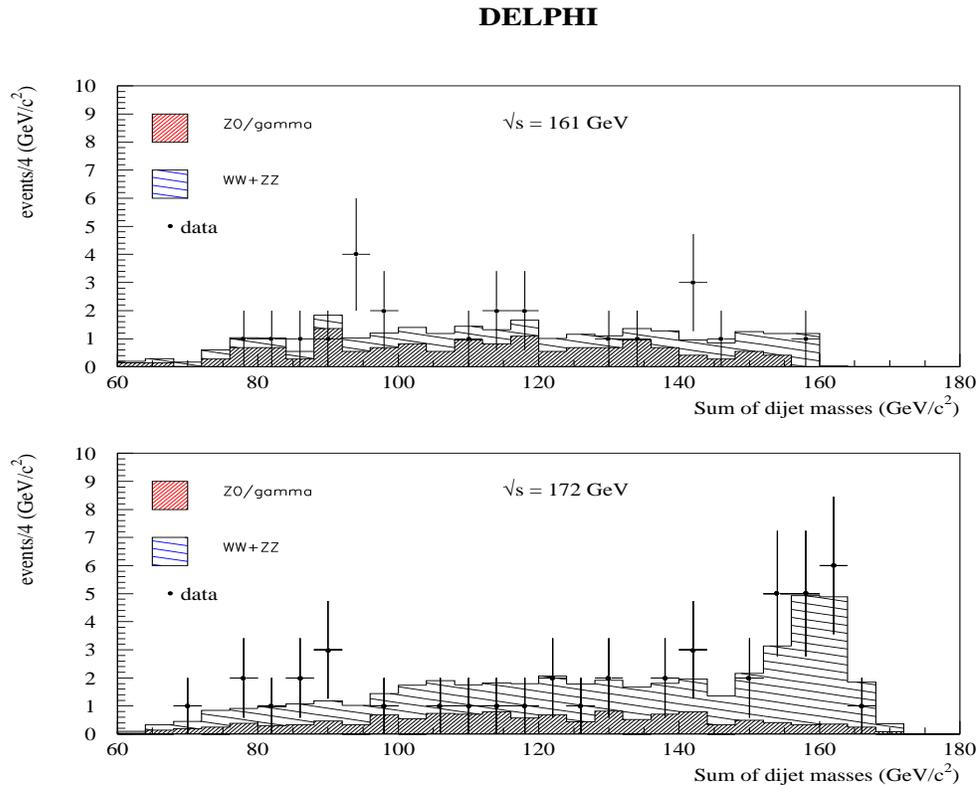

Figure 12: Four-jet channel after the tight four-jet selection: distribution of the sum of the dijet masses when the jets are paired so to minimize the difference between the dijet masses. Data at $\sqrt{s} = 161$ and $\sqrt{s} = 172$ GeV are compared with background expectations normalised to the experimental luminosity. The ZZ contribution is marginal and has been added to the WW contribution.

5.2.2 b-tagging

As a first loose b-tagging requirement, a minimum value of 3.0 is required for the event b-tagging variable, $-\log_{10}(P_E^+)$. The efficiency of this selection on four-jet final states is 60% in hZ events, 80% in hA events and 3% in WW pairs. Figure 13 shows the distribution of $-\log_{10}(P_E^+)$ after the tight four-jet selection at 161 and 172 GeV. Data are compared with the expectations from $q\bar{q}(\gamma)$, ZZ and WW backgrounds. The distribution from a signal in the $hq\bar{q}$ channel is also added to illustrate the discriminating power of the b-tagging.

DELPHI
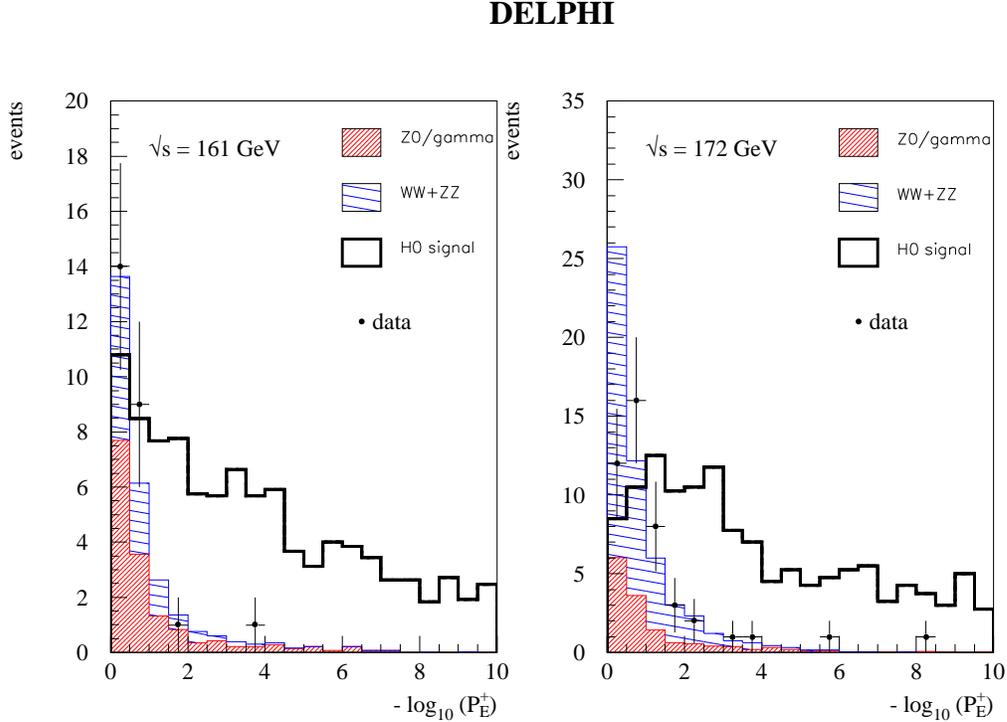
Figure 13: Four-jet channel: distribution of the b-tagging variable in four-jet events. Data at $\sqrt{s} =$161 and 172 GeV are compared with background expectations normalised to the experimental luminosity. The (unnormalised) contribution from simulated $hq\bar{q}$ signal events is also indicated.

Table 24 summarizes the effect of the selections up to now, which define the common starting sample for the searches in the $hq\bar{q}$ and hA channels. Prior to any further selection, the events are clustered into four jets with the Durham algorithm [18] and a four constraint kinematic fit is applied to define the final jet momenta.

5.2.3 The hZ channel

The final state is expected to consist of two heavy dijets, one with a mass close of m_Z and the other from the Higgs boson decay characterized by the b-content of its two hadronic jets. For each of the events selected so far, the three different combinations into dijets are considered in turn. Events are required to have at least one pairing in

$\sqrt{s}$	161 GeV					172 GeV				
selection	data	total bg.	$q\bar{q}(\gamma)$	WW ZZ	hq$\bar{q}$ $\varepsilon(\%)$	data	total bg.	$q\bar{q}(\gamma)$	WW ZZ	hq$\bar{q}$ $\varepsilon(\%)$
4-jet selection	50	57 ± 2	43	14	77.1	82	83.0 ± 1.3	36	47	78.0
tight q$\bar{q}(\gamma)$ veto	25	28.2 ± 1.1	16.2	12	60.8	45	53.2 ± 1.2	14.2	39	61.5
event b-tagging	1	2.5 ± 0.4	2.	0.5	36.2	4	2.8 ± 0.3	1.6	1.2	35.9

Table 24: Four-jet channels: common selection of events in the hZ and hA modes at $\sqrt{s} = 161$ GeV and $\sqrt{s} = 172$ GeV. Effect of the selections on data, simulated backgrounds and simulated hq$\bar{q}$ signal events with $m_h = 60$ GeV/c^2 at 161 GeV and $m_h = 70$ GeV/c^2 at 172 GeV. Efficiencies are given for the signal.

which one dijet has a mass within 20 GeV/c^2 of m_Z and the other dijet is b-tagged. The b-tagging selection is rather loose and requires the sum of the two jet b-tagging variables, $-(\log_{10}(P_{jet1}^+) + \log_{10}(P_{jet2}^+))$, to be above 2.0. If two such pairings are found, the pairing with the smallest $|m_{dijet} - m_Z|$ is considered. The mass of the Higgs boson is then estimated as $m_{dijet1} + m_{dijet2} - m_Z$ and configurations corresponding to masses below 35 GeV/c^2 are not considered any further.

A tight b-tagging is imposed in order to confirm the production of a Higgs boson in the final state. All pairings with one dijet compatible with a Z boson, as previously defined, are again considered in turn. Defining p_1 and p_2 as minus the logarithms of the b-tagging variables of the two jets in the dijet opposite to the Z, the final selection is defined as $(p_1 + k)(p_2 + k) \geq 4k^2$, where k is a parameter greater than 2. This definition is found to provide the best discrimination between the signal and the background from q$\bar{q}(\gamma)$ and WW events, as illustrated in Figure 14. The signal efficiency and background expectation as a function of k have been studied in simulation for a Higgs boson mass of 70 GeV/c^2 at 172 GeV. In order to keep a reasonable efficiency at a low background level, a value of 2.75 is chosen for k. If more than one pairing is confirmed by the tight b-tagging, the pairing with the smallest $|m_{dijet} - m_Z|$ is considered, and the final Higgs boson mass is estimated as $m_{dijet1} + m_{dijet2} - m_Z$. Note that the final pairing may differ from the one selected in the previous step when applying the loose dijet b-tagging.

$\sqrt{s}$	161 GeV					172 GeV				
selection	data	total bg.	$q\bar{q}(\gamma)$	WW ZZ	hq$\bar{q}$ $\varepsilon(\%)$	data	total bg.	$q\bar{q}(\gamma)$	WW ZZ	hq$\bar{q}$ $\varepsilon(\%)$
event b-tagging	1	2.5 ± 0.4	2.	0.5	36.2	4	2.8 ± 0.3	1.6	1.2	35.9
hZ compatibility	1	1.2 ± 0.3	0.9	0.32	32.1	3	2.0 ± 0.3	1.1	0.9	32.9
tight b-tagging	0	0.3 ± 0.1	0.2	0.07	22.8	1	0.5 ± 0.15	0.3	0.2	23.6

Table 25: hq$\bar{q}$ channel: effect of the selections at $\sqrt{s} = 161$ GeV and $\sqrt{s} = 172$ GeV on data, simulated backgrounds and simulated hq$\bar{q}$ signal events with $m_h = 60$ GeV/c^2 at 161 GeV and $m_h = 70$ GeV/c^2 at 172 GeV. Efficiencies are given for the signal.
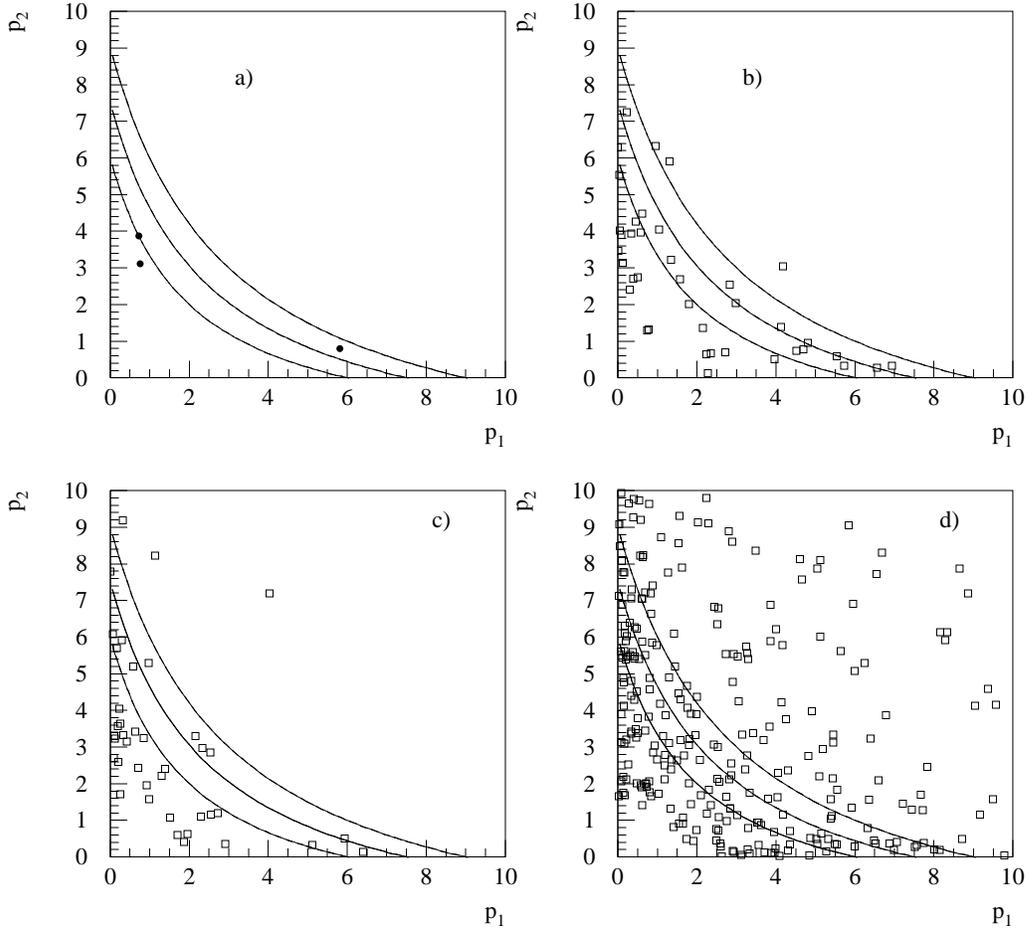
DELPHI - √s = 172 GeV

Figure 14: hq$\bar{\text{q}}$ channel: distributions of the b-tagging variables of the two jets in the dijet opposite to the Z, as a function of each other, for (a) 172 GeV data , simulated (b) WW and (c) q$\bar{\text{q}}(\gamma)$ events, and (d) simulated hq$\bar{\text{q}}$ signal events with $m_{\text{h}} = 70$ GeV/c^2. The curves correspond to different values of k (2.0, 2.5 and 3.0 from lower to upper curve) in the last b-tagging requirement, as defined in the text. The normalisation of the simulated samples is arbitrary.

Table 25 details the effect of the selections on data and simulation, while Table 26 gives the selection efficiencies. The final expected background amounts to 0.30 ± 0.10 (*stat.*) $\pm$ 0.02 (*syst.*) events at 161 GeV, mostly from the $q\bar{q}(\gamma)$ process, and to 0.50 ± 0.15 (*stat.*) $\pm$ 0.03 (*syst.*) events at 172 GeV, with equal contributions from $q\bar{q}(\gamma)$ and WW events.

m_h (GeV/c^2)	Efficiency at 161 GeV (%)	Efficiency at 172 GeV (%)
45	$19.5 \pm 1.2 \pm 0.8$	$17.2 \pm 1.3 \pm 0.7$
50	$17.8 \pm 1.2 \pm 0.7$	$18.0 \pm 1.4 \pm 0.7$
55	$18.9 \pm 1.3 \pm 0.7$	$21.0 \pm 1.5 \pm 0.8$
60	$22.8 \pm 1.0 \pm 0.9$	$24.1 \pm 1.6 \pm 0.9$
65	$23.9 \pm 1.0 \pm 0.9$	$25.0 \pm 1.6 \pm 1.0$
70	$21.6 \pm 0.8 \pm 0.8$	$23.6 \pm 1.5 \pm 0.9$
75	-	$23.7 \pm 1.5 \pm 0.9$
80	-	$27.1 \pm 1.6 \pm 1.1$

Table 26: Efficiency of the Higgs boson selection in the hq$\bar{q}$ channel at $\sqrt{s} = 161$ GeV and $\sqrt{s} = 172$ GeV, as a function of the particle mass. The first uncertainty quoted is statistical, the second is systematic.

One event is selected in the data at 172 GeV. It has two pairings with one dijet compatible with a Z boson and another dijet fulfilling the loose b-tagging requirement. The tight b-tagging selection confirms only one pairing, with dijet masses of 106.2 GeV/c^2 and 43.5 GeV/c^2. Figure 15 gives the distribution of the sum of the masses of the dijets selected by the final pairing, for simulated background and signal events and for the selected event. The Higgs boson mass, estimated as $m_{dijet1} + m_{dijet2} - m_Z$, gives 58.7 GeV/c^2 for this event. Note that the second pairing selected when the loose b-tagging is applied leads to a mass of 69 GeV/c^2. Typical resolutions on the Higgs boson mass are 3.5 GeV/c^2 at $m_h = 60$ GeV/c^2 and 2.8 GeV/c^2 at $m_h = 70$ GeV/c^2, when estimated by a Gaussian fit to the central part of the mass distributions.

The other characteristics of the selected event are the following: one of the jets used in the reconstruction of the Higgs boson candidate contains two tracks with large offsets relative to the primary vertex. They form a secondary vertex with a decay distance of 9.6 ± 0.5 mm. One of the tracks comes from a positive muon with a momentum of 9.8 GeV/c seen in the surrounding muon chambers and in the finely segmented cathode readout of the hadron calorimeter. The other track is due to a negative pion of 4.5 GeV/c. As the secondary vertex is well separated from the interaction point no other charged particle, even of low momentum, is found to be compatible with it. The estimated jet energy is 34 GeV. The large decay length and the relatively low momentum of the charged pion are not in favour of a $D°$ semileptonic decay. However, the low mass of the pion-muon system (0.72 GeV/c^2) and the low value of the muon transverse momentum (380 MeV/c) with respect to the direction from the primary vertex to the secondary vertex cannot exclude this possibility.

5.2.4   The hA channel

The final state contains two heavy dijets giving rise to four b-jets. In addition, when the hA channel dominates the production of neutral Higgs bosons, that is at large $\tan \beta$,
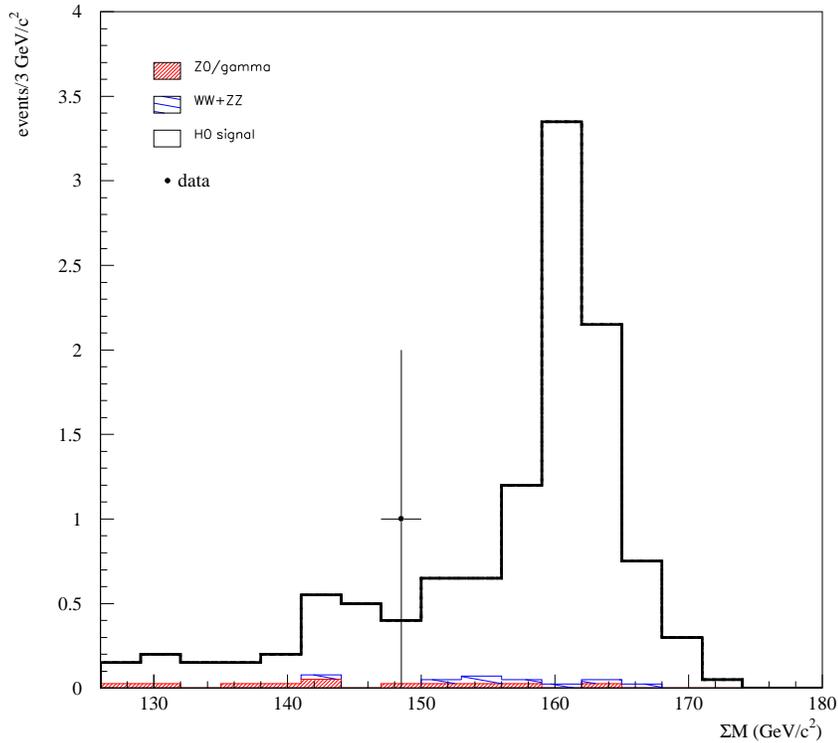
DELPHI - √s = 172 GeV

Figure 15: hqq̄ channel: distribution of the sum of the dijet masses at the end of the analysis. Data at $\sqrt{s} = 172$ GeV are compared with background expectations normalised to the experimental luminosity. The (unnormalised) contribution from simulated hqq̄ signal events with $m_{\mathrm{h}} = 70$ GeV/c^2 is also indicated.

the masses of the two dijets are expected to be nearly equal. For each of the events selected after the loose event b-tagging defined in Section 5.2.2, the dijet four-momenta are taken from the four constraint kinematic fit. Of the three dijet combinations, the jet pairing giving the smallest dijet mass difference is chosen, and the Higgs boson mass is estimated as half of the sum of the dijet masses. The dijet mass resolution is typically about 3 GeV/c^2.

A tight b-tagging selection is then applied. Defining p_1 and p_2 as minus the logarithms of the b-tagging variables of the two jets in one dijet, the dijet with the smallest $p_1 + p_2$ is required to have this sum above 1.1. In addition, the event must contain at least one jet with $-\log_{10}(P_{jet}^+)$ above 3. This reduces the qq̄gg background because gluon jets are characterized by lower values of the jet b-tagging variable. Finally, the sum of the dijet masses is required to be greater than 80 GeV/c^2 since the search is restricted to massive Higgs bosons. Table 27 details the effect of the selections on data, simulated background and signal events, while Figure 16 compares data and simulation at 172 GeV.

The final expected background is 0.6 ± 0.2 (*stat.*) ± 0.05(*syst.*) events at 161 GeV and 1.2 ± 0.1 (*stat.*) ± 0.07(*syst.*) events at 172 GeV. No event remains in the data. The signal efficiencies at large $\tan \beta$ are presented in Table 28. The dependence on $\tan \beta$ has been

$\sqrt{s}$	161 GeV					172 GeV				
selection	data	total bg.	$q\bar{q}(\gamma)$	WW ZZ	hA $\varepsilon(\%)$	data	total bg.	$q\bar{q}(\gamma)$	WW ZZ	hA $\varepsilon(\%)$
tight $q\bar{q}(\gamma)$ veto	25	28.2 ± 1.1	16.2	12	53.3	45	53.2 ± 1.2	14.2	39	52.6
event b-tagging	1	2.5 ± 0.4	2.	0.5	47.6	4	2.8 ± 0.3	1.6	1.2	46.4
tight b-tagging	0	0.9 ± 0.3	0.7	0.2	40.4	1	1.4 ± 0.2	0.9	0.5	41.5
mass sum	0	0.6 ± 0.2	0.4	0.2	40.2	0	1.2 ± 0.1	0.7	0.5	41.5

Table 27: Four-jet analysis of the hA process: effect of the selections at $\sqrt{s} = 161$ GeV and $\sqrt{s} = 172$ GeV on data, simulated backgrounds and simulated hA events with $m_A = 60$ GeV/c^2, $\tan\beta = 20$ at $\sqrt{s} = 161$ GeV and $m_A = 65$ GeV/c^2, $\tan\beta = 20$ at $\sqrt{s} = 172$ GeV. Efficiencies are given for the signal.

DELPHI - √s = 172 GeV
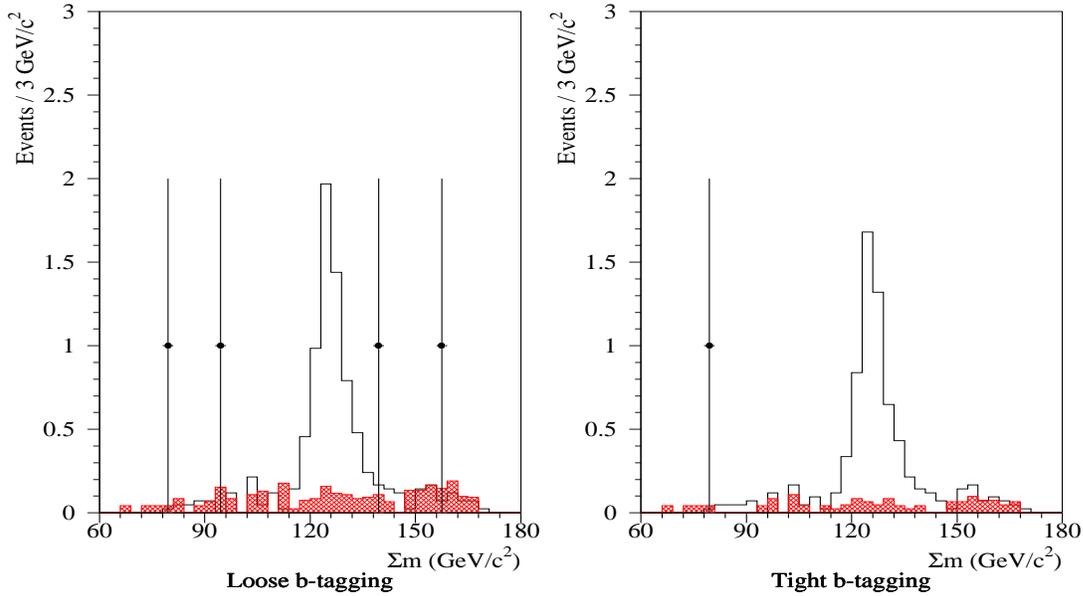
Figure 16: Four-jet analysis of the hA process: distributions of the sum of the dijet masses when the jets are paired so to minimize the dijet mass difference, after the loose event b-tagging and the final tight b-tagging, as described in the text. Data at 172 GeV (dots) are compared with simulated background events (dark cross-hatched histogram) normalised to the experimental luminosity. The white histogram shows the unnormalised expectation from signal events at $m_A = 65$ GeV/c^2 and $\tan\beta = 5$, for which $m_h = 62$ GeV/c^2.

m_A (GeV/c^2), $\tan\beta$	Efficiency at 161 GeV (%)	Efficiency at 172 GeV (%)
45, 20	$31.8 \pm 1.6 \pm 1.3$	$28.0 \pm 1.4 \pm 1.1$
50, 20	$36.8 \pm 1.5 \pm 1.5$	$35.5 \pm 1.5 \pm 1.4$
55, 20	$39.0 \pm 1.5 \pm 1.5$	$38.6 \pm 1.5 \pm 1.5$
60, 20	$40.2 \pm 1.7 \pm 1.6$	$38.2 \pm 1.5 \pm 1.5$
65, 20	$39.9 \pm 1.5 \pm 1.6$	$41.4 \pm 1.6 \pm 1.6$
70, 20	-	$38.8 \pm 1.5 \pm 1.5$

Table 28: Efficiency of the Higgs boson selection in the four-jet analysis of the hA process at $\sqrt{s} = 161$ GeV and $\sqrt{s} = 172$ GeV, as a function of m_A for $\tan\beta = 20$. The efficiency is relative to Higgs bosons decaying in all possible channels. The first uncertainty quoted is statistical, the second is systematic.

checked at a few points at 172 GeV. For $m_A = 60$ GeV/c^2 and $\tan\beta = 2$, the efficiency is $38.0\% \pm 1.5\%$ (stat) to be compared with 38.2% at $\tan\beta = 20$. For $m_A = 65$ GeV/c^2, the efficiency is $40.3\% \pm 1.8\%$ (stat.) at $\tan\beta = 5$, and $41.1\% \pm 1.6\%$ (stat.) at $\tan\beta = 40$ in agreement with the efficiency of 41.4% at $\tan\beta = 20$. The dependence on $\tan\beta$ is thus negligible and the efficiencies at $\tan\beta = 20$ can be applied on the whole parameter space.

6   Charged Higgs boson searches

The search for charged Higgs bosons is restricted to 161 GeV data which offer a better sensitivity due to the low cross-section of the irreducible WW background. In order to cover all possible decay channels, three analyses are performed searching for $\tau^+\nu_\tau\tau^-\bar{\nu}_\tau$, $cs\tau\nu_\tau$, or $c\bar{s}\bar{c}s$ final states.

6.1   Leptonic final state, $H^+H^- \to \tau^+\nu_\tau\tau^-\bar{\nu}_\tau$

This analysis relies on the identification of two acollinear tau jets and a large missing energy due to the production of four neutrinos in the final state. As the final charged multiplicity is expected to be low, attention must be paid to cosmic rays and detector backgrounds resulting in false tracks, thus leading to unphysical events. Therefore, the standard particle selection described in Section 1.4 is tightened for this analysis to ensure a high reconstruction quality. Charged particles must have a track length above 60 cm, a relative momentum error lower than 100%, and impact parameters below 1 cm in the plane transverse to the beam axis and 2.5 cm along it. Neutrals are taken into account if their energy is greater than 0.2 GeV for electromagnetic clusters, and greater than 0.5 GeV for hadronic clusters.

6.1.1   Preselection and rejection of $\gamma\gamma$ processes

Events with a low multiplicity and a large missing energy are selected by requiring the total charged multiplicity to be between 2 and 5, and the total energy to be lower than $0.55\sqrt{s}$. The $\gamma\gamma$ background is further reduced by requiring the total energy from charged particles to be greater than $0.04\sqrt{s}$ and the transverse component of the visible momentum, P_T, to be larger than 9 GeV/c. An additional selection on the visible energy

in the forward regions is introduced to reject $e^+e^-(\gamma)$ events more efficiently: the total energy in regions corresponding to polar angles $\theta < 30°$ and $\theta > 150°$ must be lower than $0.07\sqrt{s}$.

DELPHI - √s = 161 GeV
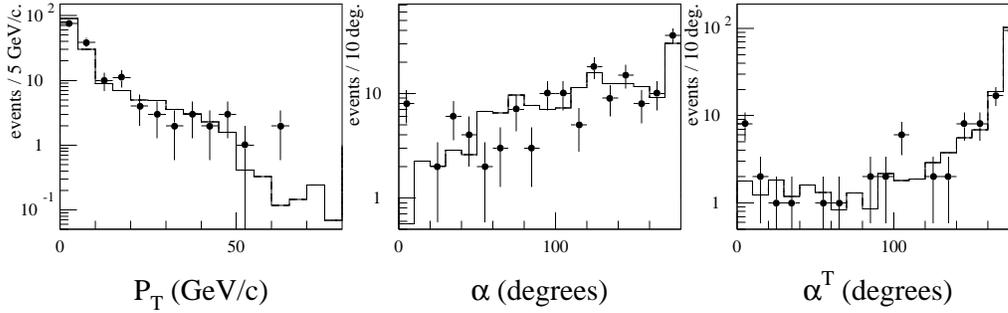

Figure 17: $H^+H^- \to \tau^+\nu_\tau\tau^-\bar{\nu}_\tau$ analysis: distributions of the transverse momentum, P_T, the angle in space between the two τ jet momenta, α, and the angle between the two τ jet transverse momenta, α^T. Data at 161 GeV (dots) are compared to background simulation (solid line) normalised to the experimental luminosity.

Comparison between data and simulation is shown at this stage of the analysis in Figure 17, where the selection on P_T has been loosened to 3 GeV/c to select larger data samples. The agreement is satisfactory, except at very low angle between the two τ jets, a region however not favoured by signal events and mostly populated by low P_T events.

6.1.2 Clustering into two jets

The particles are clustered into two jets by the JADE [28] algorithm. As the τ leptons from the Higgs bosons have acollinear momenta, the $l^+l^-(\gamma)$ background is reduced by requiring $\max(\alpha, \alpha^T) < 167°$ where α is the angle between the two jets and α^T the angle between their transverse momenta. To reject events where the jets are too close to each other (as in the $\gamma\gamma \to \tau^+\tau^-$ process) the condition $\alpha > 20°$ is also imposed.

Quality requirements are applied to both jets. The energy carried by the charged particles of each jet must be greater than 1 GeV, and the greatest angle between any pair of particles inside a jet must be lower than 28°. Finally, to reduce the contamination of prompt electrons and muons from $l^+l^-(\gamma)$ or WW final states, the energy of the more energetic jet is required to be below 58 GeV and that of the less energetic jet below 30 GeV.

Table 29 summarizes the effect of the selections on data, simulated backgrounds and simulated signal events with $m_{H^\pm} = 50$ GeV/c^2. The final expected background, mainly from WW pairs, is 1.4 ± 0.2 ($stat.$) ± 0.3 ($sys.$) events, while no event is left in the data. The final efficiencies are shown in Table 30.

Systematic uncertainties may come from the limited precision in the integrated luminosity or from the choice of the signal generator, but the dominant source is the imperfection of the detector simulation. In order to estimate this uncertainty, the distributions

of the main analysis variables in real and simulated data were precisely compared. These variables are P_T, α, α^T and the jet energies. The comparison was made at the leptonic preselection level with the loose selection in P_T. For each variable, the difference between the average values of the distributions in real and simulated events was calculated, the selection on the variable was then shifted by the value of this difference and the changes in efficiency and selected background were recorded. The same procedure was applied for the four variables, and the corresponding variations in the selection efficiency and expected background were added quadratically.

Selection	data	total bg.	$l^+l^-(\gamma)$	$\gamma\gamma$	WW	other bg.	H^+H^- $\epsilon(\%)$
preselection	156	158 ± 6	46	109	2.1	1.0	70.4
P_T	46	40.7 ± 2.2	33.9	4.3	2.0	0.5	60.1
α, α^T	6	5.35 ± 0.58	2.15	1.13	1.84	0.23	52.0
τ jet energies	0	1.44 ± 0.19	0.20	0.20	0.90	0.14	38.0

Table 29: $H^+H^- \to \tau^+\nu_\tau\tau^-\bar{\nu}_\tau$ analysis: effect of the selections at $\sqrt{s} = 161$ GeV on data and simulated backgrounds. The efficiency on simulated signal events with $m_{H^\pm} = 50$ GeV/c^2 is also quoted.

$m_{H^\pm}$ (GeV/c^2)	Efficiency (%)
42.0	$31.0 \pm 1.2\,^{+2.2}_{-2.2}$
46.0	$39.8 \pm 1.3\,^{+2.1}_{-3.0}$
50.0	$38.0 \pm 1.3\,^{+2.5}_{-2.5}$
54.0	$36.1 \pm 1.3\,^{+2.1}_{-1.8}$
60.0	$39.7 \pm 1.3\,^{+2.5}_{-1.7}$
66.0	$43.9 \pm 1.3\,^{+1.8}_{-2.0}$

Table 30: $H^+H^- \to \tau^+\nu_\tau\tau^-\bar{\nu}_\tau$ analysis: selection efficiency at $\sqrt{s} = 161$ GeV as a function of the charged Higgs boson mass. The first uncertainty quoted is statistical, the second is systematic.

6.2 Semi-leptonic final state, $H^+H^- \to cs\tau\nu_\tau$

This analysis relies first on the identification of isolated τ jet candidates in a hadronic environment. A Fisher discriminant analysis [25] is then used to reject 90% of the background while retaining 90% of the signal. Finally a kinematic fit is used to identify candidates consistent with H^+H^- pair production for a given $H^\pm$ mass.

6.2.1 Preselection

Hadronic events are selected if the charged multiplicity is at least seven, the total energy from the charged particles is greater than $0.15\sqrt{s}$, and the total energy is greater

than $0.25\sqrt{s}$. To remove two-jet events in a back-to-back topology, events are divided into two hemispheres with respect to the plane perpendicular to the sphericity axis and the acollinearity between the two hemispheric jets is required to be larger than 9°.

6.2.2 Rejection of $q\bar{q}(\gamma)$ events with a visible photon

In order to reject $q\bar{q}(\gamma)$ events having an energetic photon seen by the detector, two more requirements are made. The energy of the most energetic electromagnetic cluster must be lower than 35 GeV and the total energy from particles emitted at polar angles lower than 20° (30°) and greater than 160° (150°) must be below 50 GeV (80 GeV).

6.2.3 Tagging of the τ jet

Events are clustered into three jets using the JADE [28] algorithm, and the jet of lowest charged multiplicity is attributed to the τ decay. If two jets have the same charged multiplicity, the less energetic one is considered as the τ jet.

Further requirements on the τ jet characteristics are made to achieve a good purity in the τ identification. The jet charged multiplicity must be between 1 and 3, its total multiplicity must be 7 or less, and its total energy must not exceed 60 GeV. In order to reject $q\bar{q}(\gamma)$ events where the radiated photon gives a thin jet due to conversion or showering in the detector material, the electromagnetic energy in the τ jet has to be below 45 GeV and the jet must not contain a track starting in the time projection chamber. The distributions, at preselection level, of three of these variables are shown in Figure 18. A disagreement in the absolute normalisation is observed between data and simulation.
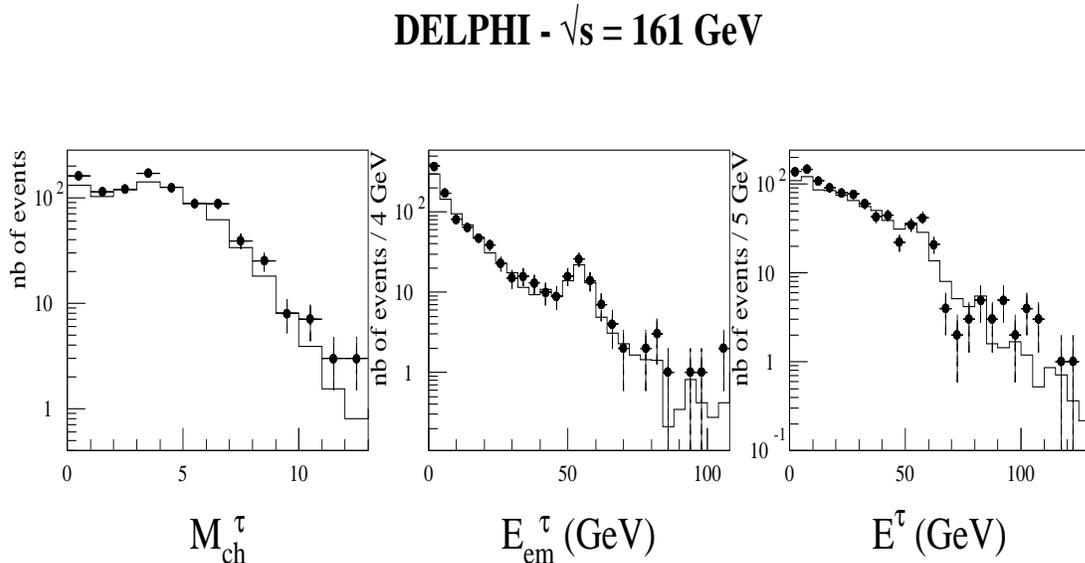

Figure 18: $H^+H^- \to cs\tau\nu_\tau$ analysis: distributions of the charged multiplicity, the electromagnetic energy and the total energy of the τ jet candidate, at preselection level. Data at 161 GeV (dots) are compared to background simulation (solid line) normalised to the experimental luminosity.

6.2.4 Fisher discriminant analysis

A discriminant analysis is performed using the Fisher method [25]. The distributions used to define the discriminating variable are obtained with a sample of 3000 signal events (with $m_{\mathrm{H}\pm} = 45$, 48, and 51 GeV/c^2) and a sample of 6000 q$\bar{\mathrm{q}}(\gamma)$ background events, both samples taken after the preselection. The input variables are chosen among different jet and shape variables which show important differences between signal and background, such as the polar angle of the visible momentum, Fox-Wolfram moments [27] and the different opening angles between the three jets (angles in space and angles measured in the plane transverse to the beam axis). If two variables are very correlated for the signal (for example, the polar angle of the total momentum and the polar angle of the hadronic dijet momentum), only the most discriminating one according to the Fisher algorithm is kept. The variables selected for the analysis are, in order of decreasing discriminating power:

- $\theta_{vis}^f = |\pi/2 - \theta_{vis}|$, where θ_{vis} is the polar angle of the total momentum; this variable offers a good discrimination since signal events are distributed as $\sin^2\theta_{vis}$;
- $\min_j(E_j) \cdot \alpha_{j_1 j_2}$, the product of the energy of the less energetic hadronic jet (in GeV) and the angle between the two hadronic jets (in radians);
- $\alpha_{\tau, j1+j2}$, the angle between the τ jet and the system of the two hadronic jets;
- y_{23}^{JADE}, the minimal value of the clustering distance, in the JADE algorithm, between any two jets among the three jets in the event.

The three last variables allow to separate the signal from the dominant background of q$\bar{\mathrm{q}}(\gamma)$ events with an undetected photon along the beam axis, which lead to different configurations with a fake τ jet from a radiated gluon, part of a quark jet or a low mutliplicity quark jet. The linear combination is:

$$F_{cs\tau\nu} = 2.55 \cdot \theta_{vis}^f + 0.02 \cdot \min_j(E_j) \cdot \alpha_{j_1 j_2} + 0.352 \cdot \alpha_{\tau, j1+j2} - 0.189 \cdot \ln(y_{23}^{\mathrm{JADE}})$$

and the selection, $F_{cs\tau\nu} < 4.2$, is chosen to keep 90% of the signal events at 48 GeV/c^2. Figure 19 shows the distribution of $F_{cs\tau\nu}$ for real and simulated data after the requirements on the τ jet variables. Also shown is the expected distribution for signal events.

6.2.5 Kinematic fit

A kinematic fit is performed [19] in order to check the compatibility of the selected events with the hypothesis of the production of two particles of equal mass. To refine the τ four-momentum reconstruction, a hypothetical neutrino is added to the τ jet and the mass of the τ jet-neutrino system is assumed to be consistent with the τ mass in the fit procedure. In addition to the usual constraints of total energy and momentum conservation, the hadronic system, made of the two hadronic jets, and the leptonic system, defined by the τ and a hypothetical neutrino from the Higgs boson decay, are required to have equal invariant masses. Events are selected if the overall χ^2 is lower than 10.0, which is safely above the average value of 3.1 observed for signal events. Figure 19 shows the distribution of the common invariant mass of the cs and $\tau\nu_\tau$ systems as given by the fit, $m_{\mathrm{H}+}^{rec}$, for data, simulated backgrounds and simulated signal events. A total of 12 events remain in the data, in agreement with the expected background of 11.1 ± 0.6 (*stat.*) ± 0.3 (*syst.*). The lowest mass in these events is found to be equal to 60.2 GeV/c^2.

Finally, events are selected in a mass window around a given value of $m_{\mathrm{H}\pm}$ to be tested. The mass window is chosen to keep 90% of the signal events: $m_{\mathrm{H}+} - 20 < m_{\mathrm{H}+}^{rec} < m_{\mathrm{H}+} + 6$.
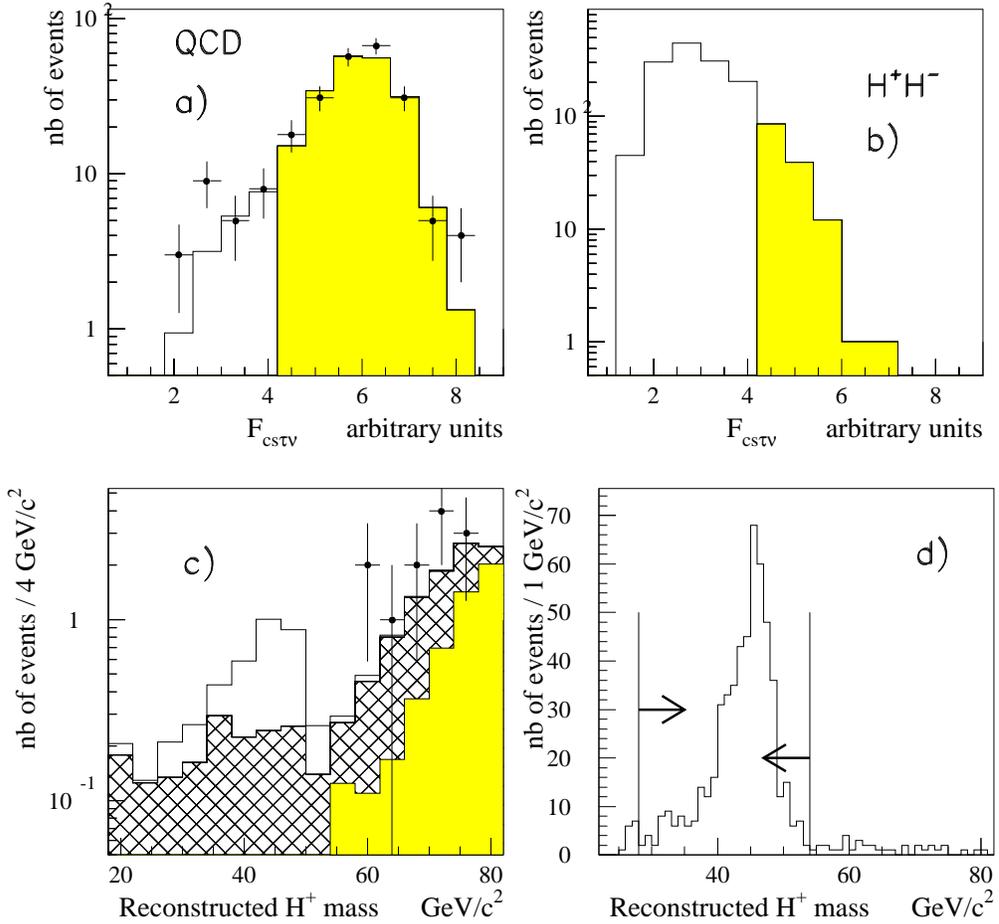
DELPHI - √s = 161 GeV

Figure 19: $H^+H^- \to cs\tau\nu_\tau$ analysis: a) and b): distribution of the multidimensional function $F_{cs\tau\nu}$ after the requirements on the τ jet (in grey, the events rejected by the selection on $F_{cs\tau\nu}$); c) and d): distribution of the reconstructed H^+mass after the fit. Plots in a) and c) compare data (dots) to background simulation (solid line) normalised to the experimental luminosity. In c) the grey histogram is the WW contamination and the hatched histogram is the $q\bar{q}(\gamma)$ contribution. Also added is the normalised distribution of simulated signal events at 48 GeV/c^2 (in white). Plots in b) and d) show unnormalised signal distributions with $m_{H\pm} = 48$ and 51 GeV/c^2 in b) and $m_{H\pm} = 48$ GeV/c^2 in d). Arrows in d) indicate the final selection.

The asymmetry reflects the distortion of the mass distribution due to the missing energy carried by the neutrino, which is only partly corrected by the kinematic fit. Table 31 summarizes the effect the selections on data, simulated backgrounds and simulated signal events. The last selection in the table corresponds to testing the hypothesis of a 48 GeV/c^2 Higgs boson. Table 32 shows, for different tested masses, the number of selected events in the data, the expected background and the signal efficiency.

The systematic uncertainties have been obtained with the same method as in the previous topology. The variables used to compare data and simulation are the acollinearity, the discriminating function, the χ^2 of the fit, and the reconstructed mass. The acollinearity distributions obtained from data and simulation were compared after the hadronic preselection, while the other distributions were compared after the acollinearity cut.

Selection	data	total bg.	$q\bar{q}$	$\gamma\gamma$	WW	other bg.	H^+H^- $\epsilon(\%)$
preselection	947	836 ± 7	769	28	19	20	92.6
no vis. γ	724	633 ± 6	581	18	17	17	90.0
τ jet	243	218 ± 4	191	12	8.8	6.5	69.2
$F_{cs\tau\nu} < 4.2$	25	17.6 ± 0.9	11.2	0	5.3	1.1	62.8
kinem. fit	12	11.1 ± 0.6	5.7	0	4.8	0.6	57.5
$28 < m_{H+}^{rec} < 54$	0	1.22 ± 0.25	0.95	0	0.18	0.07	51.5

Table 31: $H^+H^- \rightarrow cs\tau\nu_\tau$ analysis: effect of the selections at $\sqrt{s} = 161$ GeV on data and all simulated backgrounds. The efficiency on simulated signal events with $m_{H^\pm}$ = 48 GeV/c^2 is also quoted.

$m_{H^\pm}$ (GeV/c^2)	mass window	data	total bg.	Efficiency (%)
42.0	$22 < m_{H+}^{rec} < 48$	0	$1.07 \pm 0.23 \pm 0.21$	$47.3 \pm 1.5 \, ^{+1.1}_{-1.0}$
45.0	$25 < m_{H+}^{rec} < 51$	0	$1.17 \pm 0.24 \pm 0.12$	$48.0 \pm 1.5 \, ^{+1.2}_{-1.3}$
48.0	$28 < m_{H+}^{rec} < 54$	0	$1.22 \pm 0.25 \pm 0.11$	$51.5 \pm 1.5 \, ^{+1.0}_{-0.9}$
51.0	$31 < m_{H+}^{rec} < 57$	0	$1.33 \pm 0.25 \pm 0.13$	$50.2 \pm 1.5 \, ^{+0.7}_{-0.8}$
54.0	$34 < m_{H+}^{rec} < 60$	0	$1.53 \pm 0.26 \pm 0.18$	$46.7 \pm 1.5 \, ^{+0.8}_{-1.3}$
57.0	$37 < m_{H+}^{rec} < 63$	2	$1.73 \pm 0.27 \pm 0.24$	$46.9 \pm 1.5 \, ^{+0.6}_{-1.5}$

Table 32: $H^+H^- \rightarrow cs\tau\nu_\tau$ analysis: window in the reconstructed mass used as final selection, number of selected events in the data, expected background and signal efficiency at $\sqrt{s} = 161$ GeV as a function of the charged Higgs boson mass. The first uncertainty quoted is statistical, the second is systematic.

6.3 Hadronic final state, $H^+H^- \rightarrow c\bar{s}\bar{c}s$

The analysis starts from the common four-jet sample described in Section 5.1.3. It again relies on a Fisher discriminant analysis to separate the bulk of the signal events

from the bulk of the background from $q\bar{q}(\gamma)$ and WW processes, followed by kinematic fits to reconstruct the mass of the initial bosons with good resolution.

6.3.1 Fisher discriminant analysis

A multidimensional function, F_{cscs}, is calculated as in the semi-leptonic analysis. The two samples used for the discrimination are composed of 1600 signal events (with $m_{H\pm}$ = 47, 50 GeV/c^2), and of 3000 $q\bar{q}(\gamma)$ events for the background, both samples fulfilling the four-jet selection. F_{cscs} is a combination of the following variables, in order of decreasing discriminating power:

- $\mathcal{J}$, defined as the product of the energy of the least energetic jet and the minimum opening angle between any two jets (in GeV.rad), the event being forced into four jets by the JADE algorithm,
- H_2, the second Fox-Wolfram moment [27];
- $\theta_{sph}^f = |\pi/2 - \theta_{sph}|$, where θ_{sph} is the polar angle of the *sphericity* axis.

The linear combination is:

$$F_{cscs} = 0.087 \cdot \mathcal{J} - 3.03 \cdot H_2 - 0.939 \cdot \theta_{sph}^f$$

Figure 20 shows the distribution of F_{cscs} for real and simulated data after the four-jet selection. For the signal, the $\mathcal{J}$ variable depends on the opening angle between the decay products of each Higgs boson, and thus varies with $m_{H\pm}$. As a consequence, the mean value of F_{cscs} increases with $m_{H\pm}$. Therefore, two selections on F_{cscs} are applied depending on the mass hypothesis. The first one, $F_{cscs} > -0.58$, is applied when testing mass hypotheses below 49 GeV/c^2, and is chosen to keep 75% of the signal events with m_{H+} in this mass range. The second selection, $F_{cscs} > -0.36$, is applied when testing hypotheses above 49 GeV/c^2 and is designed to keep 80% of the signal events generated with higher masses. This criterion is looser than previously because of the fast decrease of the cross-section with increasing mass.

6.3.2 Kinematic fits

Two kinematic fits are applied in order to reconstruct the initial four-jet topology and to have an estimate of the mass of the Higgs particle. The first fit, applied at the level of the common four-jet selection, constrains the measured energy and angles of the jets to satisfy total energy and momentum conservation. Using the fitted values of the jet momenta, the invariant mass of each combination of two jets is calculated, and the pairing which gives the smallest difference between the two dijet invariant masses is selected. The second fit requires, as a fifth constraint, the masses of the two dijets in this pairing to be equal. Events are kept if the overall χ^2 of the second fit is lower than 12.5, which has to be compared to an average value of 10 for the signal.

The final selection depends on the hypothesised H^+ mass, $m_{H\pm}$: the reconstructed H^+mass, m_{H+}^{rec}, as given by the fit, is required to be equal to m_{H+} within 3 GeV/c^2, to keep 70% of the signal events generated with $m_{H\pm}$ = 50 GeV/c^2.

Figure 20 shows the distribution of m_{H+}^{rec} for data, simulated backgrounds and simulated signal events at 47 GeV/c^2, after the requirement on the χ^2 of the first fit. A total of 13 events remain in the data in agreement with the expected background of 16.9 $\pm$ 0.8 (*stat.*) $\pm$ 1.2 (*syst.*). All events have reconstructed masses greater than 59.7 GeV/c^2, except one which has a mass of 46.2 GeV/c^2. It has four clear jets, one with only three
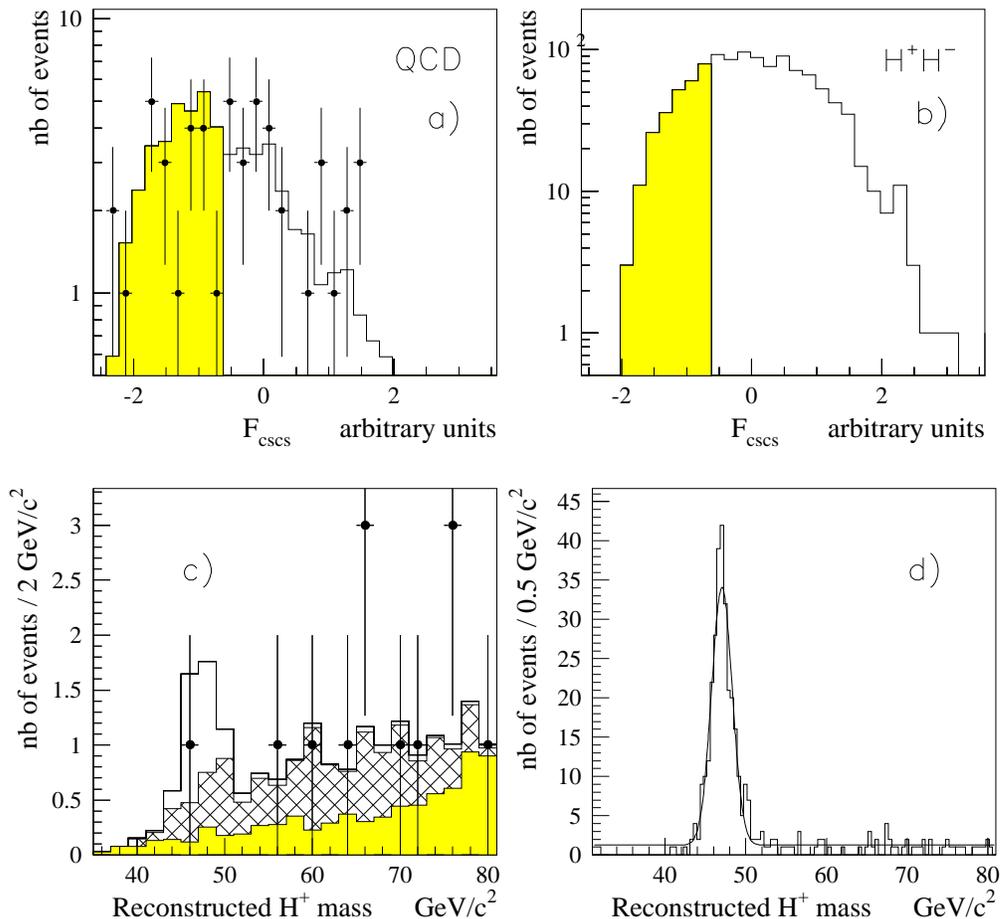
DELPHI - √s = 161 GeV

Figure 20: $H^+H^- \to c\bar{s}\bar{c}s$ analysis: a) and b): distribution of the multidimensional function F_{cscs} after the four-jet selection (in grey, the events rejected by the selection on F_{cscs}); c) and d): distribution of the reconstructed H^+ mass after the fit. Plots in a) and c) compare data (dots) to background simulation (solid line) normalised to the experimental luminosity. In c) the grey histogram is the WW contamination and the hatched histogram is the $q\bar{q}(\gamma)$ contribution. Also added is the normalised distribution of simulated signal events with $m_{H^\pm} = 47$ GeV/c^2 (in white). Plots in b) and d) show unnormalised signal distributions with $m_{H^\pm} = 44$ and 47 GeV/c^2 in b) and $m_{H^\pm} = 47$ GeV/c^2 in d). The Gaussian fit in d) has a mean of 47.0 GeV/c^2 and a r.m.s of 1.3 GeV/c^2.

charged particles but taking 80% of the jet energy. The lowest polar angle of the jets is equal to 28°, which is high enough to ensure a good reconstruction. The χ^2 of the four (five) constraint fit is equal to 4.6 (4.7). All these values are stable if the jets are clustered using the Durham [18] distance. Moreover, one of the charged particles has a momentum of 7.8 GeV/c and is identified by the central RICH detector as a kaon, one standard deviation away from the proton hypothesis. Such charged kaons are expected from the hadronization of s-quarks. This event can thus be considered as a good candidate for the signal but is also compatible with what is expected from the simulated $q\bar{q}$ or WW backgrounds.

Selection	data	total bg.	$q\bar{q}$	WW	other bg.	H^+H^- (%)
four jets	50	57.1 ± 1.7	43.2	12.9	1.03	71.2
$F_{cscs} > -0.58$	27	25.2 ± 1.0	14.2	10.4	0.70	55.0
kinem. fit	13	16.9 ± 0.8	9.0	7.4	0.48	45.4
$44 < m_{H^+}^{rec} < 50$	1	1.86 ± 0.30	1.32	0.52	0.02	34.2

Table 33: $H^+H^- \to c\bar{s}\bar{c}s$ analysis: effect of the selection at $\sqrt{s} = 161$ GeV on data and all simulated backgrounds. The efficiency on simulated signal events with $m_{H^\pm} = 47$ GeV/c^2 is also quoted.

$m_{H^\pm}$ (GeV/c^2)	mass window	data	total bg.	Efficiency (%)
41.0	$38 < m_{H^+}^{rec} < 44$	0	$0.56 \pm 0.12 \pm 0.04$	$23.4 \pm 1.5 \pm 0.6$
44.0	$41 < m_{H^+}^{rec} < 47$	1	$1.16 \pm 0.23 \pm 0.08$	$30.0 \pm 1.6 \pm 0.8$
47.0	$44 < m_{H^+}^{rec} < 50$	1	$1.86 \pm 0.30 \pm 0.13$	$34.2 \pm 1.7 \pm 0.9$
50.0	$47 < m_{H^+}^{rec} < 53$	0	$1.71 \pm 0.28 \pm 0.12$	$32.7 \pm 1.6 \pm 0.8$
53.0	$50 < m_{H^+}^{rec} < 56$	0	$1.85 \pm 0.30 \pm 0.13$	$37.1 \pm 1.7 \pm 1.0$
56.0	$53 < m_{H^+}^{rec} < 59$	0	$2.07 \pm 0.30 \pm 0.14$	$31.4 \pm 1.5 \pm 0.8$

Table 34: $H^+H^- \to c\bar{s}\bar{c}s$ analysis: window in the reconstructed mass used as final selection, number of selected events in the data, expected background and signal efficiency at $\sqrt{s} = 161$ GeV as a function of the charged Higgs boson mass. The first uncertainty quoted is statistical, the second is systematic.

Table 33 summarizes the result of the selections on data, simulated backgrounds and simulated signal events at 47 GeV/c^2. The last line in the table corresponds to testing the 47 GeV/c^2 mass hypothesis. Table 34 shows, for different tested masses, the number of selected events in the data, the expected background, and the signal efficiency.

6.4 Reanalysis of earlier high energy data

Data taken at 130-136 GeV in 1995 [30] were reanalysed with an analysis similar to that just presented. The final expected background is 0.61 ± 0.23 ($stat.$) ± 0.25 ($syst.$) events in the leptonic topology and no event is selected in the data. The signal efficiency is above

41% for masses between 46 and 55 GeV/c^2. The expected backgrounds before the last selection based on the analysis in a mass window amount to 5.7 ± 0.6 (*stat.*) ± 0.5 (*syst*) events in the mixed topology and to 5.1 ± 0.5 (*stat.*) ± 0.8 (*syst.*) events in the four-jet topology. The respective numbers of observed events are 6 and 2. The reconstructed masses in the selected events are higher than 57.7 GeV/c^2 in the mixed topology and higher than 59.2 GeV/c^2 in the four-jet analysis. The final signal efficiencies range from 33% to 26% for masses between 45 and 53 GeV/c^2 in the mixed topology, and from 28% to 19% for masses between 44 and 55 GeV/c^2 in the four-jet analysis.

7   Results

The results of the searches presented in the previous sections translate into exclusion limits on the production cross-sections of the $e^+e^- \to hZ$, $e^+e^- \to hA$ and $e^+e^- \to H^+H^-$ processes. The procedure to derive the limits is detailed for the neutral Higgs bosons as a first example to introduce the method. The charged Higgs bosons are treated afterwards with less detail, but the method is the same.

7.1   Neutral Higgs bosons

For each analysis of the hZ and hA channels at 161 and 172 GeV, Tables 35 and 36 summarize the expected background, the error on it, the integrated luminosity and number of observed events. The errors are obtained by summing the statistical and systematic uncertainties quadratically. For asymmetric uncertainties, the larger error is taken into account. To illustrate the relative importance of the different channels, the signal expectations are given for Higgs boson masses of 65 GeV/c^2.

It should be noted that there is an overlap between some analyses in the selected background only, i.e. between the analyses of the two missing energy channels, between the three analyses of the topology with two jets and two τ leptons and between the two four-jet analyses. There is no overlap however between the four-jet analyses and the analyses in the τ channels. After subtraction of the common background, the total background is 2.88 events in the two missing energy channels, 2.08 events in the three channels with τ in the final state, and 2.04 events in the two four-jet channels. In total, 3 events are observed in the data while 7.49 events are expected. When excluding the invisible decays of the Higgs boson h, 2 events are selected in the data and 5.87 events are expected from the simulation.

7.1.1   Limits on cross-sections and masses

As a first step, limits at the 95% confidence level (CL) are derived for each process separately, i.e. the hZ process with standard decays of the Higgs boson, the hZ process with the Higgs boson decaying into invisible products, and the hA process at large $\tan\beta$. The limits are computed at each centre-of-mass energy and combining the two energies.

The multi-channel approach as described in [31] is applied to combine the results of the different analyses while preserving the information about efficiency, expected background, number of candidates, and centre-of-mass energy in each analysis. The definition of the confidence level is derived in the Bayesian approach and assumes that the probability function for the observation of the total number of events is a product of independent Poisson distributions, one for each channel, with parameters given by the number of candidates and the sum of the background and signal expectations in the channel. In the

$\sqrt{s}$	161 GeV					172 GeV				
channel	bg.	error	lum.	evts	sig	bg.	error	lum.	evts	sig.
$h\mu^+\mu^-$	0.04	0.01	9.96	0	0.16	0.13	0.03	10.0	0	0.22
he^+e^-	0.13	0.04	9.96	0	0.09	0.20	0.06	10.0	0	0.12
$h\nu\bar{\nu}$	0.65	0.19	9.74	1	0.57	0.61	0.12	10.0	0	0.89
$(h \to \tau^+\tau^-)q\bar{q}$	0.32	0.09	9.96	0	0.08	0.91	0.14	10.0	0	0.12
$(h \to q\bar{q})\tau^+\tau^-$	0.31	0.10	9.96	0	0.05	0.22	0.07	10.0	0	0.06
$hq\bar{q}$	0.30	0.10	9.96	0	1.10	0.50	0.15	10.0	1	1.65
$h \to$ inv., $Z \to q\bar{q}$	0.78	0.27	9.74	0	0.81	1.40	0.34	10.0	1	1.51

Table 35: Expected background, uncertainty on it, integrated luminosity, number of observed events and signal expectation at 65 GeV/c^2 in all channels analysed in the hZ search at $\sqrt{s} = 161$ GeV and $\sqrt{s} = 172$ GeV.

$\sqrt{s}$	161 GeV					172 GeV				
channel	bg.	error	lum.	evts	sig	bg.	error	lum.	evts	sig
$hA \to \tau^+\tau^-q\bar{q}$	0.20	0.09	9.96	0	0.06	0.42	0.09	10.0	0	0.07
$hA \to b\bar{b}b\bar{b}$	0.60	0.21	9.96	0	0.73	1.20	0.12	10.0	0	0.84

Table 36: Expected background, uncertainty on it, integrated luminosity, number of observed events and signal expectation at 65 GeV/c^2 in all channels analysed in the hA search at $\sqrt{s} = 161$ GeV and $\sqrt{s} = 172$ GeV.

limit derivation, a total cross-section is assumed, the signal expectations in each channel are deduced from the channel luminosities, efficiencies and branching fractions, and the input cross-section is varied until a 95% confidence level is reached. As the efficiencies depend on the mass of the Higgs boson, the limit on the cross-section also depends on it.

The definition of the confidence level in the Bayesian approach makes the expected background important only in channels with candidates. Thus, the possible overlap between two analyses makes this method inappropriate to combine their results only if candidates are selected in the two analyses, which is not the case here. To account for errors in the background and efficiency estimates, the statistical and systematic uncertainties are added quadratically, considering only the larger error in case of assymmetric uncertainties, and the individual Poisson distributions are folded with Gaussian resolution functions. No mass information about the selected events and remaining background is included in the computation.

Tables 37 to 39 show the 95% CL upper limits on the cross-sections in each process at 161 GeV, 172 GeV, and after combining both energies. The limits on cross-sections at 161 and 172 GeV are valid in any model in which the Higgs decay branching fractions are as in the SM for the hZ process and as in the MSSM for the hA process. The limits achieved when combining the two energies, expressed as upper limits in the cross-sections at 172 GeV, assume in addition that the cross-section ratio between the two energies is as in the previous models.

$\sqrt{s}$	$m_{\mathrm h}$ (GeV/c^2)	45	50	55	60	65	70	75	80
161 GeV	limit on σ_{161} (pb)	1.44	1.40	1.35	1.21	1.20	1.34	-	-
172 GeV	limit on σ_{172} (pb)	1.93	1.58	1.37	1.28	1.27	1.35	1.39	1.40
combined	limit on σ_{172} (pb)	0.87	0.80	0.76	0.74	0.82	1.17	1.39	1.40
	for $\sigma_{161}^{\mathrm{hZ}}$ / $\sigma_{172}^{\mathrm{hZ}}$ =	1.163	1.111	1.035	0.915	0.698	0.224	0	0
172 GeV	SM σ_{172} (pb)	1.64	1.48	1.31	1.13	0.94	0.73	0.49	0.17
combined	exclusion CL (%)	99.8	99.8	99.6	99.3	97.0	82.7	59.3	23.3

Table 37: Upper limits at the 95% CL on the SM hZ cross-section as a function of $m_{\mathrm h}$ at $\sqrt{s} = 161$ GeV, at $\sqrt{s} = 172$ GeV and after combining both centre-of-mass energies. The last two lines give the SM cross-section at $\sqrt{s} = 172$ GeV and the confidence level at which this is excluded by the combination of 161 and 172 GeV data.

$\sqrt{s}$	$m_{\mathrm h}$ (GeV/c^2)	45	50	55	60	65	70	75	80
161 GeV	limit on σ_{161} (pb)	3.08	3.12	2.39	2.18	2.43	3.10	-	-
172 GeV	limit on σ_{172} (pb)	4.00	3.30	3.05	2.64	2.48	2.36	2.56	3.36
combined	limit on σ_{172} (pb)	1.71	1.63	1.41	1.34	1.54	2.06	2.56	3.36

Table 38: Upper limits at the 95% CL on the hZ·Br(h → invisible) cross-section as a function of $m_{\mathrm h}$ at $\sqrt{s} = 161$ GeV, at $\sqrt{s} = 172$ GeV, and after combining both centre-of-mass energies.

$\sqrt{s}$	$m_{\mathrm A}$ (GeV/c^2)	45	50	55	60	65	70
161 GeV	limit on σ_{161} (pb)	0.86	0.75	0.71	0.70	0.70	-
172 GeV	limit on σ_{172} (pb)	0.96	0.76	0.71	0.72	0.67	0.71
combined	limit on σ_{172} (pb)	0.42	0.35	0.34	0.35	0.36	0.71
	for $\sigma_{161}^{\mathrm{hA}}$ / $\sigma_{172}^{\mathrm{hA}}$ =	1.164	1.126	1.073	1.007	0.911	0
172 GeV	MSSM σ_{172} (pb)	0.59	0.45	0.36	0.28	0.20	0.14
combined	exclusion CL (%)	98.5	97.7	95.5	90.4	81.6	43.6

Table 39: Upper limits at the 95% CL on the hA cross-section at large $\tan\beta$ as a function of $m_{\mathrm A}$ at $\sqrt{s} = 161$ GeV, at $\sqrt{s} = 172$ GeV and after combining both centre-of-mass energies. The last two lines give the MSSM cross-section at $\sqrt{s} = 172$ GeV and the confidence level at which this is excluded by the combination of 161 and 172 GeV data.

Tables 37 and 39 also show the SM hZ and MSSM hA cross-sections. Except in the case of the hZ·Br(h → invisible) channel, the upper limits exclude part of the theoretical cross-sections and lead to lower limits on the Higgs boson masses. The result for the SM Higgs boson is presented in Figure 21. The 95% CL lower limit on the mass [§] is:
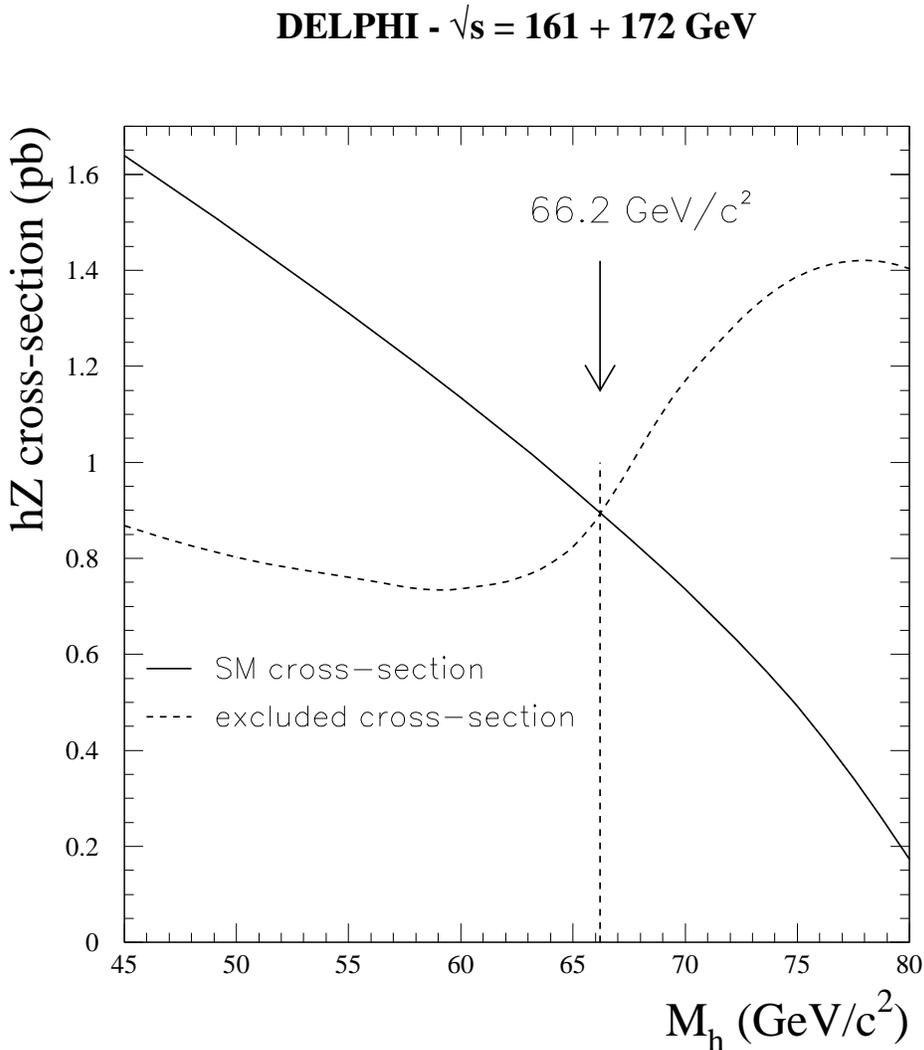
$$m_\mathrm{h} > 66.2 \ \mathrm{GeV}/c^2 \qquad\qquad (95\%\mathrm{CL}) \ .$$

DELPHI - √s = 161 + 172 GeV

Figure 21: hZ production cross-section in the Standard Model compared with the 95% CL upper limit on the hZ cross-section derived from the results of the hZ searches at $\sqrt{s} = 161$ GeV and $\sqrt{s} = 172$ GeV. The sharp rise in the limit above 60 GeV/c^2 is due to the fact that the 161 GeV data do no longer contribute.

To check whether fusion diagrams, not included in the simulation, would lead to a weaker limit due to the candidate in the h$\nu\bar{\nu}$ channel, the signal expectations of this channel have been enhanced by the ratio of the total h$\nu\bar{\nu}$ cross-section to the pure hZ

[§] This limit was also evaluated using the Modified Frequentist Likelihood Ratio method [32] including mass information. This method gave the same mass limit but gave lower cross-section limits at lower and higher mass values away from the masses of the two candidates.

cross-section, as obtained with the WPHACT generator [33]. This assumes that the selection efficiency would remain unchanged for fusion final states, which is not guaranteed since the analysis relies on the assumption that the neutrino pair comes from a Z. However this is a way to test the maximal impact of fusion diagrams on the limit. The effect of this correction is an increase of the limit by 0.2 GeV/c^2. Neglecting fusion diagrams thus leads to a more conservative limit. It has also been checked that the limit remains unchanged when the exact splitting of the 172 GeV data sample between 170.3 GeV and 172.3 GeV is taken into account.

For completeness, the result for the pseudoscalar Higgs boson A, valid at high $\tan \beta$, is:

$$m_A > 55.7 \text{ GeV}/c^2 \hspace{3cm} (95\%\text{CL}) .$$

7.1.2 Neutral Higgs bosons in the MSSM

The results in the hZ and hA processes are combined using the multi-channel approach and including earlier results at $\sqrt{s} = 130\text{-}136$ GeV [30] for the hA process. For the hZ process, the efficiencies obtained for a SM Higgs boson are first corrected to account for higher branching fractions of the h boson into $b\bar{b}$ in the MSSM. To derive the exclusion regions, the MSSM parameter space is scanned and in each point the hZ and hA cross-sections are computed, assuming a top mass of 175 GeV/c^2, a SUSY scale at 1 TeV, a range of variation for m_A between 0 and 400 GeV/c^2 [34] and a given hypothesis about the mixing in the stop sector. The signal expectations in each analysis are derived from the cross-sections and used with the expected backgrounds and numbers of candidates to compute the confidence level at which the input point is excluded. The results thus translate into regions of the MSSM parameter space excluded at 95% CL. They are strongly dependent on the assumption about the mixing in the stop sector. To include all cases, the three usual hypotheses [34] have been made, the two extreme cases of no mixing and maximal mixing (with a value of -100 GeV for the SUSY Higgs boson mixing term μ) and the third case called typical mixing.

The results are first presented in the (m_h, $\tan \beta$) plane in Figure 22. Whatever the assumption on the mixing, a 95% CL lower limit on m_h is derived for all values of $\tan \beta$ greater than or equal to unity:

$$m_h > 59.5 \text{ GeV}/c^2 \hspace{3cm} (95\%\text{CL}) .$$

This limit comes from the performance of the searches at large $\tan \beta$ (ie in the hA channel) and the assumption of a typical mixing.

The results can also be presented in the (m_A, $\tan \beta$) plane as shown in Figure 23. A 95% CL lower limit on m_A is derived for all values of $\tan \beta$ above or equal to unity and all mixing scenarios:

$$m_A > 51.0 \text{ GeV}/c^2 \hspace{3cm} (95\%\text{CL}) .$$

This limit is driven by the performance of the searches at low $\tan \beta$ (hence mainly by the hZ channel) and the assumption of maximal mixing. The same figure shows that the lower limit on m_A at large $\tan \beta$ is 60.1 GeV/c^2, 4.4 GeV/c^2 higher than the limit quoted in the previous section, due to the inclusion of the results at 130-136 GeV. Finally, Figure 24 presents the exclusion regions in the (m_h, m_A) plane.

The above results assume the Higgs bosons to decay into fermions. In the case of maximal mixing, however, there is a small area in the parameter space, close to the
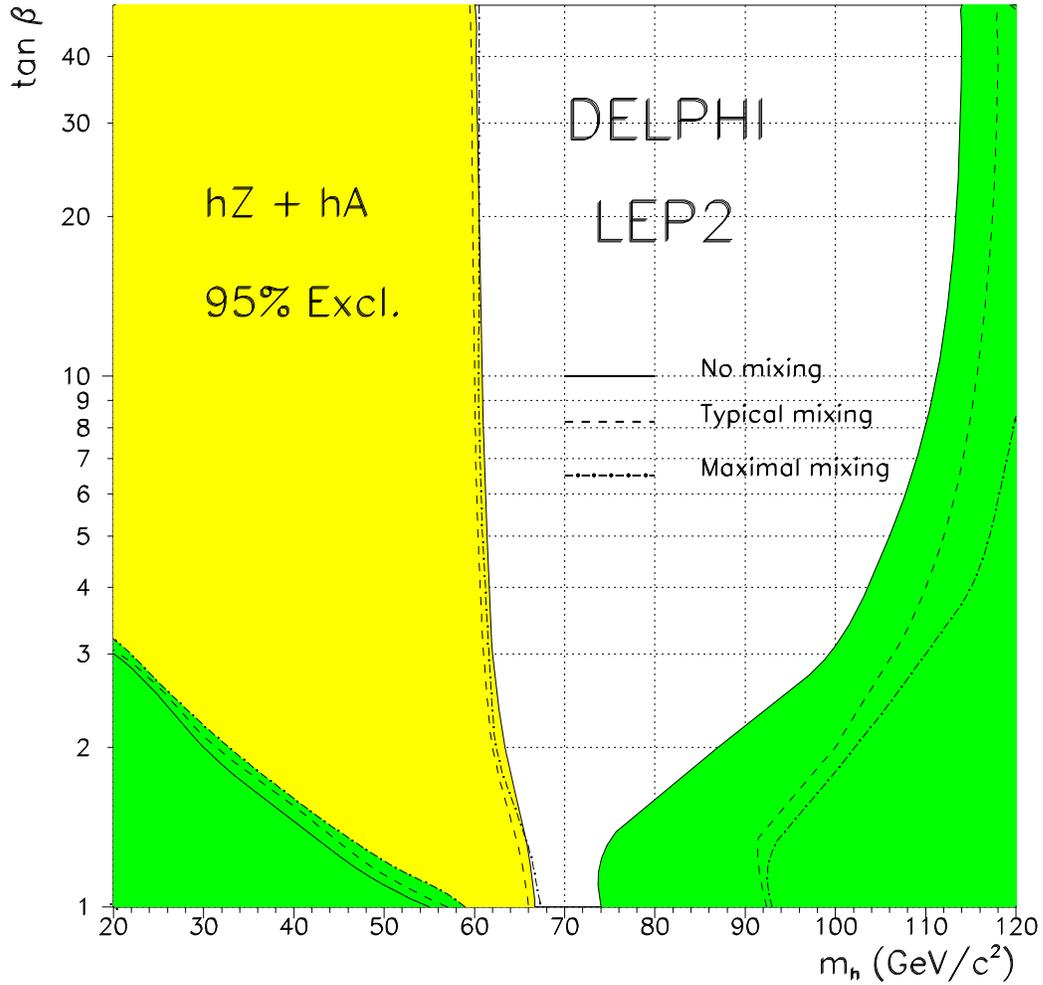
Figure 22: Regions in the $(m_h, \tan\beta)$ plane excluded at 95% CL by the negative result of the searches in the hZ and hA production modes at high energy. The regions not allowed by the MSSM model are in dark grey. Three hypotheses for the mixing in the stop sector have been considered.
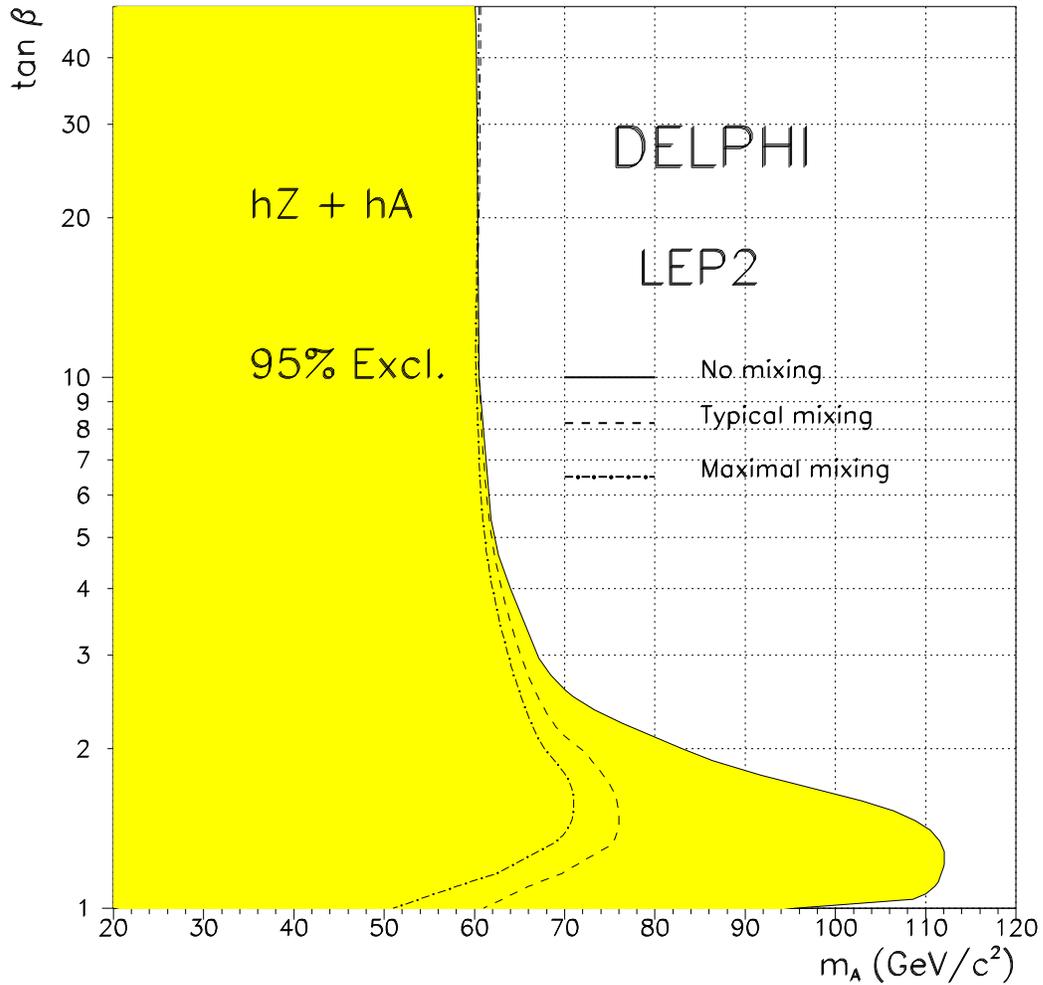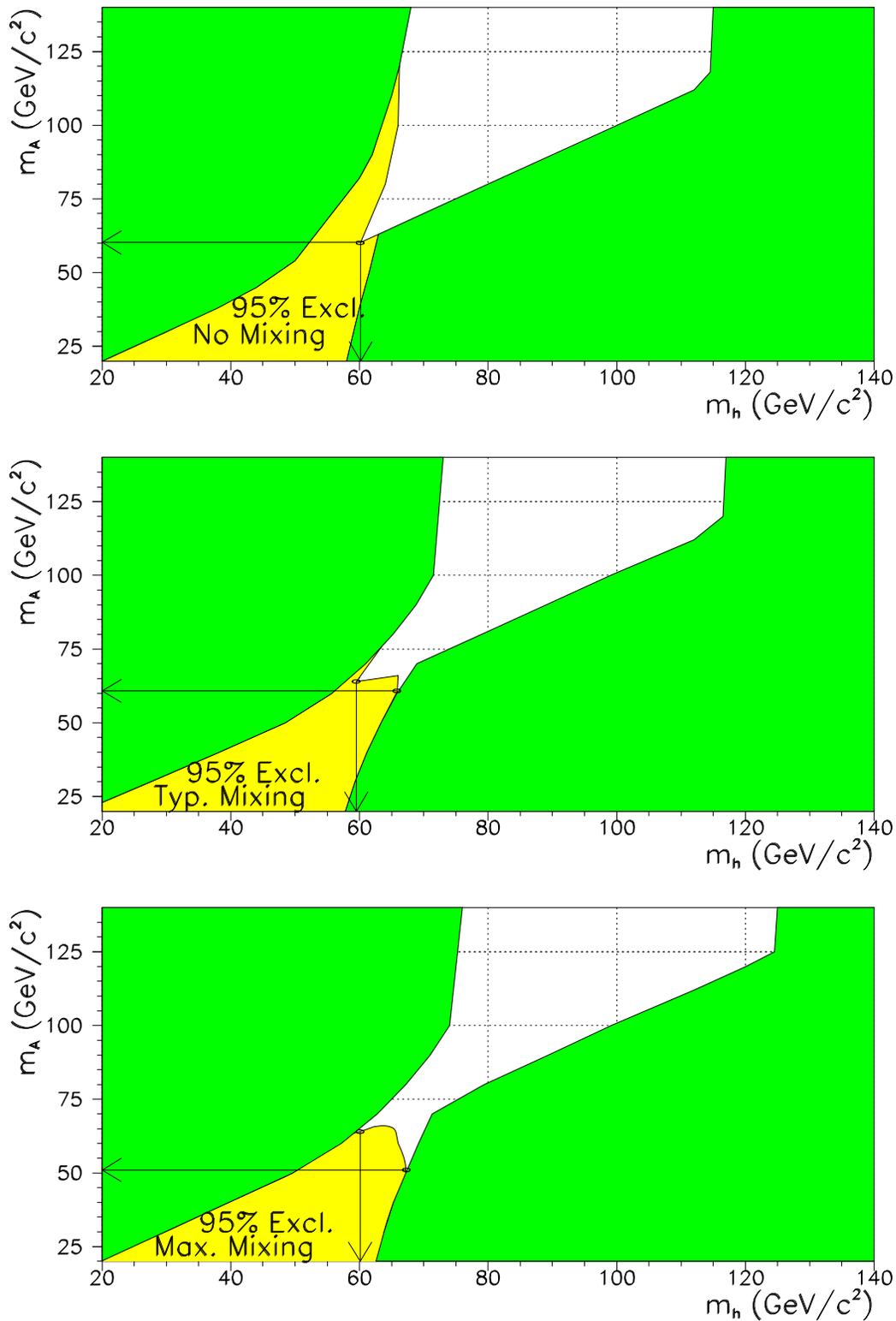
Figure 23: Region in the $(m_A, \tan\beta)$ plane excluded at 95% CL by the result of the searches in the hZ and hA channels at high energy. Three different hypotheses for the mixing in the stop sector are presented.

Figure 24: Region in the (m_h, m_A) plane excluded at 95% CL by the result of the searches in the hZ and hA channels at high energy. Three different hypotheses for the mixing in the stop sector are presented. The regions not allowed by the MSSM model for $m_{squark} = 1$ TeV/c² are in dark grey.

boundary of the forbidden region at low m_h, where $m_h > 2m_A$ so that the h $\to$ AA decay opens. The area extends from $m_h \sim 41$ GeV/c^2 and $\tan\beta = 1.8$, to $m_h \sim 64$ GeV/c^2 and $\tan\beta = 1$, and corresponds to large hZ or hA cross-sections. A simulation of hZ and hA events with h $\to$ AA has been performed in the dominant channels (h$\nu\bar{\nu}$ and 4 jets) and the efficiency of the previous analyses found to be sufficient to confirm the exclusion of this region.

7.2 Charged Higgs bosons

The multi-channel approach is also applied to the case of the charged Higgs bosons, which is valid since there is no overlap between the three analyses for either signal or background. The results are derived in the general framework of two-doublet models which are governed by only two parameters, the Higgs boson mass and its branching fraction into hadrons. A test of a given hypothesis (m_0,Br$_0$) on the values of the mass and branching ratio into hadrons is made by means of the multi-channel approach. Here, the signal expectation in each analysis is defined as the product of the theoretical cross-section calculated with $m_{H^\pm} = m_0$, the integrated luminosity used in the analysis, the analysis selection efficiency, and a factor depending on the branching ratio into hadrons. This factor is defined as $(1 - Br_0)^2$ in the purely leptonic analysis, as $2 \cdot Br_0 \cdot (1 - Br_0)$ in the semi-leptonic analysis, and as Br_0^2 in the purely hadronic analysis. Thus one obtains the confidence level with which the hypothesis (m_0,Br$_0$) is excluded. By scanning the (m_{H^+}, Br(H$^+$ $\to$ hadrons)) plane, it is then possible to determine the regions excluded at 95% CL, as shown in Figure 25.

8 Conclusions

The high energy runs of the LEP collider in 1996 opened a new era in the searches for Higgs bosons, especially for neutral Higgs bosons. Due to a more favorable signal to background ratio, it was possible for the first time to cover all final states expected from the production of neutral Higgs bosons. In particular, topologies with four jets or two jets and two τ leptons are now included in the analyses of the hZ production mode.

With 20pb^{-1} collected at $\sqrt{s} = 161$ GeV and $\sqrt{s} = 172$ GeV, DELPHI selected one event in the missing energy channel and one event in the four-jet channel, both in the hZ mode. In the hypothesis of a Higgs boson production, they would correspond to masses of 65 GeV/c^2 and 59 GeV/c^2 respectively. However, the background expectations make them compatible with standard processes.

The results were translated into limits at the 95% confidence level on the masses of the SM and MSSM Higgs bosons:

$$\text{SM}: \qquad m_h > 66.2 \text{ GeV}/c^2 \qquad\qquad (95\%\text{CL})$$

$$\text{MSSM, } \tan\beta \geq 1: \qquad m_h > 59.5 \text{ GeV}/c^2 \qquad\qquad (95\%\text{CL})$$

$$\text{MSSM, } \tan\beta \geq 1: \qquad m_A > 51.0 \text{ GeV}/c^2 \qquad\qquad (95\%\text{CL}).$$

These results significantly improve the limits reached with previous data taken at the Z resonance peak.

A search for charged Higgs bosons was also performed in the data sample at 161 GeV in all possible final-state topologies. One event was selected in the four-jet topology which would correspond to a 46 GeV/c^2 Higgs particle. The observation of one event is also fully consistent with the background expected from standard processes. Earlier high

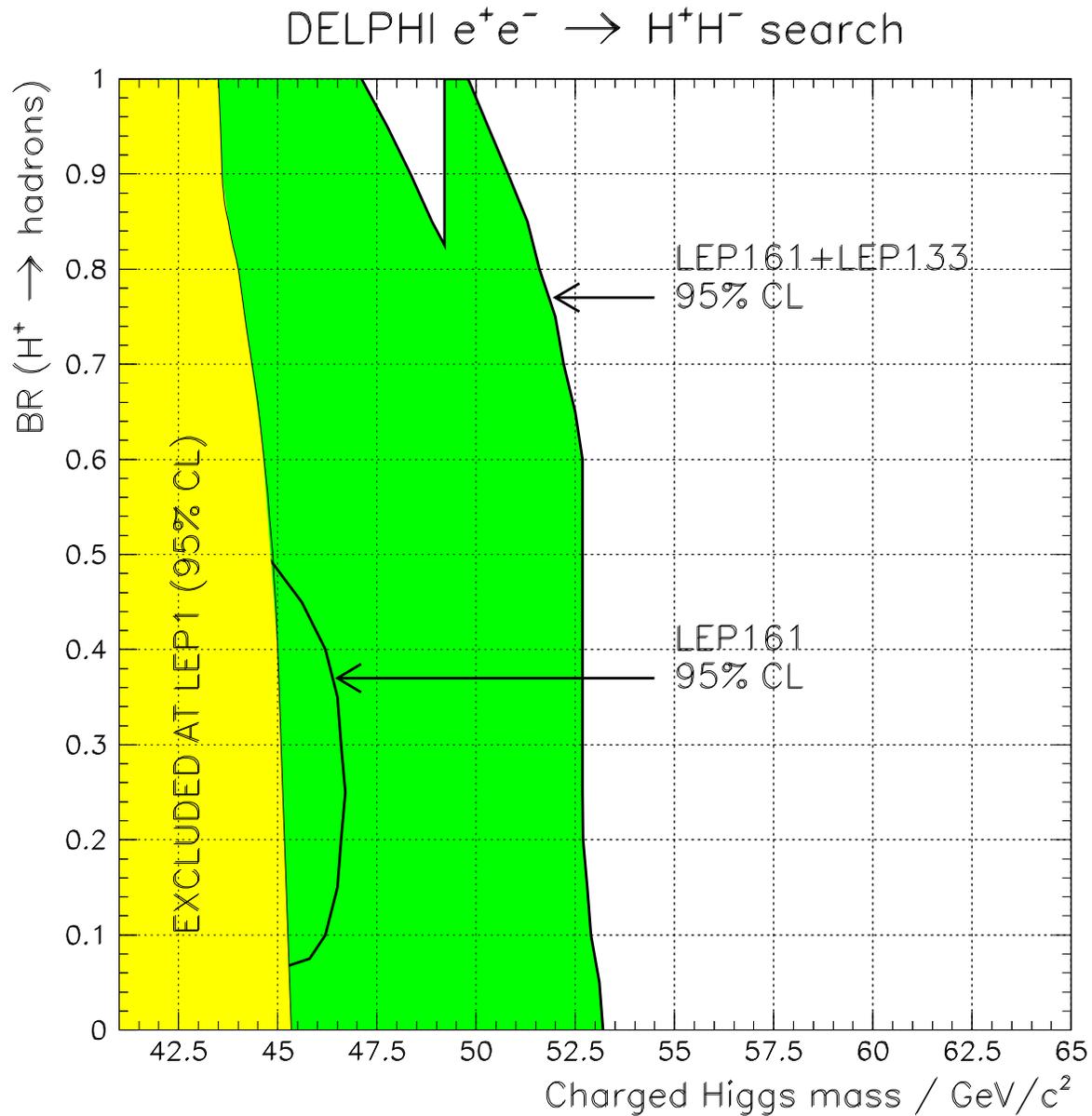Figure 25: $e^+e^- \to H^+H^-$ analysis: excluded regions in the m_{H^+}, $Br(H^+ \to hadrons)$. The light grey area is the domain excluded at LEP1 at 95% confidence level. The dark grey area is the region excluded at 95% confidence level by the combination of the analyses at 161 GeV and 130-136 GeV. The result at 95% confidence level obtained with 161 GeV data only is also indicated. The discontinuity in the upper part of the plot is due to the event selected at 161 GeV in the four-jet analysis at a mass of 46.2 GeV/c^2.

energy data were also reanalysed in a similar way. The following exclusion limit, valid in any two-doublet model, was derived:

$$m_{H\pm} > 51.5 \text{ GeV}/c^2 \quad \text{if } \text{Br}(H^+ \rightarrow \text{hadrons}) < 0.8 \qquad (95\%\,\text{CL}) \,.$$

Acknowledgements

References

[1] H.P. Nilles. Phys. Rep. 110 (1984) 1;
    H.E. Haber and G.L. Kane, Phys. Rep. 117 (1985) 75.

[2] CERN Report 96-01, Physics at LEP2, Vol. 1, page 388, fig. 14.

[3] DELPHI Collaboration, P. Abreu et al., Zeit. Phys. **C67** (1995) 69.

[4] DELPHI Collaboration, P. Abreu et al., Nucl. Phys. **B421** (1994) 3.

[5] DELPHI Collaboration, P. Abreu et al., Zeit. Phys. **C64** (1994) 183.

[6] DELPHI Collaboration, P. Abreu et al., Nucl. Instr. Meth. **A378** (1996) 57.

[7] DELPHI Collaboration, P. Abreu et al., Nucl. Instr. Meth. **A303** (1991) 233.

[8] P. Janot, in CERN Report 96-01, Vol. 2, p.309.

[9] E. Gross, B.A. Kniehl and G. Wolf, Zeit. Phys. **C63** (1994) 417; err. ibid. **C66** (1995) 32.

[10] A. Djouadi, M. Spira and P.M. Zerwas, Zeit. Phys. **C70** (1996) 427.
     A. Djouadi, J. Kalinowski and P.M. Zerwas, DESY Report 95-211.

[11] T. Sjöstrand, Comp. Phys. Comm. **39** (1986) 347.

[12] R. Decker, S. Jadach, J. Kühn and Z. Was, Comp. Phys. Comm. **76** (1993) 361.

[13] H. Baer et al., in CERN Report 86-02, Vol. 1, p.297.

[14] F.A. Berends, R.Kleiss, W.Hollik, Nucl. Phys. **B304** (1988) 712.

[15] S. Nova, A.Olchevski and T.Todorov, in CERN Report 96-01, Vol. 2, p.224.

[16] F.A. Berends, P.H. Daverveldt, R. Kleiss, Comp. Phys. Comm. **40** (1986) 271, 285 and 309.

[17] G. Borisov, C. Mariotti, DAPNIA/Spp Report 97-06 and INFN/ISS Report 97-03, 'Performance of b-tagging in DELPHI at LEP2'.

[18] S. Catani, Yu.L. Dokshitzer, M. Olson, G. Turnock and B.R. Webber Phys. Lett. **B269** (1991) 432.

[19] N.J. Kjaer, Ph.D. thesis, Niels Bohr Institute Copenhagen, 1991.

[20] T. Sjöstrand, Comp. Phys. Comm. **28** (1983) 227.

[21] F.A. Berends, R. Kleiss and R. Pittau, in CERN Report 96-01, Vol. 2, p.23.

[22] I. Helleren, R. Keranen, Bergen Report 1997-07, 'Analysis of hadronic events with missing energy and momentum for Higgs boson searches in DELPHI data at $\sqrt{s} =$161 and 172 GeV'.

[23] T.G.M. Malmgren, K.E. Johansson, 'An iterative discriminant analysis method to search for the Higgs particle at LEP2', submitted to Nucl. Instr. Meth.

[24] Proceedings of the ECFA workshop on LEP200, ECFA report 97/108, Vol. 2, p.320.

[25] R.A. Fisher, The use of multiple measurements in taxonomic problems, Annals of Eugenics, Vol.7 (1936);
     M.G. Kendall and A. Stuart, The advanced theory of statistics, Vol.3, 1966, Griffin ed., London.

[26] R.K. Ellis, D.A. Ross and A.E. Terrano Nuc. Phys. **B178** (1981) 421.

[27] G.C. Fox and S. Wolfram, Phys. Lett. **B82** (1979) 134.

[28] S. Bethke et al., Phys. Lett. **B213** (1988)235.

[29] L. Lönnblad, Comp. Phys. Comm. **71** (1992) 15.

[30] DELPHI Collaboration, P. Abreu et al., Zeit. Phys. **C73** (1996) 1.

[31] V.F. Obraztsov, Nucl. Instr. Meth. **A316** (1992) 388.

[32] A.L. Read, 'Optimal Search Method based on the Likelihood Ratio and its Application to the Search for the MSM Higgs Boson at $\sqrt{s} = 161$ and 172 GeV', DELPHI note in preparation.

[33] E. Accomando and A. Ballestrero, in CERN Report 96-01, Vol. 2, p.312.

[34] CERN Report 96-01, Physics at LEP2, Vol. 1, page 399.